



**IJOER**  
RESEARCH JOURNAL

ISSN  
2395-6992

# International Journal of Engineering Research & Science



[www.ijoer.com](http://www.ijoer.com)  
[www.adpublications.org](http://www.adpublications.org)

Volume-6! Issue-2! February, 2020

[www.ijoer.com](http://www.ijoer.com) ! [info@ijoer.com](mailto:info@ijoer.com)

## Preface

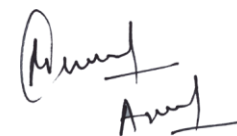
We would like to present, with great pleasure, the inaugural volume-6, Issue-2, February 2020, of a scholarly journal, *International Journal of Engineering Research & Science*. This journal is part of the AD Publications series *in the field of Engineering, Mathematics, Physics, Chemistry and science Research Development*, and is devoted to the gamut of Engineering and Science issues, from theoretical aspects to application-dependent studies and the validation of emerging technologies.

This journal was envisioned and founded to represent the growing needs of Engineering and Science as an emerging and increasingly vital field, now widely recognized as an integral part of scientific and technical investigations. Its mission is to become a voice of the Engineering and Science community, addressing researchers and practitioners in below areas

Chemical Engineering	
Biomolecular Engineering	Materials Engineering
Molecular Engineering	Process Engineering
Corrosion Engineering	
Civil Engineering	
Environmental Engineering	Geotechnical Engineering
Structural Engineering	Mining Engineering
Transport Engineering	Water resources Engineering
Electrical Engineering	
Power System Engineering	Optical Engineering
Mechanical Engineering	
Acoustical Engineering	Manufacturing Engineering
Optomechanical Engineering	Thermal Engineering
Power plant Engineering	Energy Engineering
Sports Engineering	Vehicle Engineering
Software Engineering	
Computer-aided Engineering	Cryptographic Engineering
Teletraffic Engineering	Web Engineering
System Engineering	
Mathematics	
Arithmetic	Algebra
Number theory	Field theory and polynomials
Analysis	Combinatorics
Geometry and topology	Topology
Probability and Statistics	Computational Science
Physical Science	Operational Research
Physics	
Nuclear and particle physics	Atomic, molecular, and optical physics
Condensed matter physics	Astrophysics
Applied Physics	Modern physics
Philosophy	Core theories

Chemistry	
Analytical chemistry	Biochemistry
Inorganic chemistry	Materials chemistry
Neurochemistry	Nuclear chemistry
Organic chemistry	Physical chemistry
Other Engineering Areas	
Aerospace Engineering	Agricultural Engineering
Applied Engineering	Biomedical Engineering
Biological Engineering	Building services Engineering
Energy Engineering	Railway Engineering
Industrial Engineering	Mechatronics Engineering
Management Engineering	Military Engineering
Petroleum Engineering	Nuclear Engineering
Textile Engineering	Nano Engineering
Algorithm and Computational Complexity	Artificial Intelligence
Electronics & Communication Engineering	Image Processing
Information Retrieval	Low Power VLSI Design
Neural Networks	Plastic Engineering

Each article in this issue provides an example of a concrete industrial application or a case study of the presented methodology to amplify the impact of the contribution. We are very thankful to everybody within that community who supported the idea of creating a new Research with IJOER. We are certain that this issue will be followed by many others, reporting new developments in the Engineering and Science field. This issue would not have been possible without the great support of the Reviewer, Editorial Board members and also with our Advisory Board Members, and we would like to express our sincere thanks to all of them. We would also like to express our gratitude to the editorial staff of AD Publications, who supported us at every stage of the project. It is our hope that this fine collection of articles will be a valuable resource for *IJOER* readers and will stimulate further research into the vibrant area of Engineering and Science Research.



Mukesh Arora  
(Chief Editor)

## **Board Members**

### **Mukesh Arora (Editor-in-Chief)**

BE(Electronics & Communication), M.Tech(Digital Communication), currently serving as Assistant Professor in the Department of ECE.

### **Prof. Dr. Fabricio Moraes de Almeida**

Professor of Doctoral and Master of Regional Development and Environment - Federal University of Rondonia.

### **Dr. Parveen Sharma**

Dr Parveen Sharma is working as an Assistant Professor in the School of Mechanical Engineering at Lovely Professional University, Phagwara, Punjab.

### **Prof.S.Balamurugan**

Department of Information Technology, Kalaignar Karunanidhi Institute of Technology, Coimbatore, Tamilnadu, India.

### **Dr. Omar Abed Elkareem Abu Arqub**

Department of Mathematics, Faculty of Science, Al Balqa Applied University, Salt Campus, Salt, Jordan, He received PhD and Msc. in Applied Mathematics, The University of Jordan, Jordan.

### **Dr. AKPOJARO Jackson**

Associate Professor/HOD, Department of Mathematical and Physical Sciences, Samuel Adegboyega University, Ogwa, Edo State.

### **Dr. Ajoy Chakraborty**

Ph.D.(IIT Kharagpur) working as Professor in the department of Electronics & Electrical Communication Engineering in IIT Kharagpur since 1977.

### **Dr. Ukar W.Soelistijo**

Ph D , Mineral and Energy Resource Economics, West Virginia State University, USA, 1984, Retired from the post of Senior Researcher, Mineral and Coal Technology R&D Center, Agency for Energy and Mineral Research, Ministry of Energy and Mineral Resources, Indonesia.

### **Dr. Samy Khalaf Allah Ibrahim**

PhD of Irrigation &Hydraulics Engineering, 01/2012 under the title of: "Groundwater Management Under Different Development Plans In Farafra Oasis, Western Desert, Egypt".

### **Dr. Ahmet ÇİFCİ**

Ph.D. in Electrical Engineering, Currently Serving as Head of Department, Burdur Mehmet Akif Ersoy University, Faculty of Engineering and Architecture, Department of Electrical Engineering (2015-...)

### **Dr. Mohamed Abdel Fatah Ashabrawy Moustafa**

Ph.D. in Computer Science - Faculty of Science - Suez Canal University University, 2010, Egypt.

Assistant Professor Computer Science, Prince Sattam bin AbdulAziz University ALkharj, KSA.

### **Dr. Heba Mahmoud Mohamed Afify**

Ph.D degree of philosophy in Biomedical Engineering, Cairo University, Egypt worked as Assistant Professor at MTI University.

### **Dr. Aurora Angela Pisano**

Ph.D. in Civil Engineering, Currently Serving as Associate Professor of Solid and Structural Mechanics (scientific discipline area nationally denoted as ICAR/08—"Scienza delle Costruzioni"), University Mediterranea of Reggio Calabria, Italy.

### **Dr. Faizullah Mahar**

Associate Professor in Department of Electrical Engineering, Balochistan University Engineering & Technology Khuzdar. He is PhD (Electronic Engineering) from IQRA University, Defense View, Karachi, Pakistan.

### **Dr. S. Kannadhasan**

Ph.D (Smart Antennas), M.E (Communication Systems), M.B.A (Human Resources).

### **Dr. Christo Ananth**

Ph.D. Co-operative Networks, M.E. Applied Electronics, B.E Electronics & Communication Engineering Working as Associate Professor, Lecturer and Faculty Advisor/ Department of Electronics & Communication Engineering in Francis Xavier Engineering College, Tirunelveli.

### **Dr. S.R.Boselin Prabhu**

Ph.D, Wireless Sensor Networks, M.E. Network Engineering, Excellent Professional Achievement Award Winner from Society of Professional Engineers Biography Included in Marquis Who's Who in the World (Academic Year 2015 and 2016). Currently Serving as Assistant Professor in the department of ECE in SVS College of Engineering, Coimbatore.

### **Dr. Maheshwar Shrestha**

Postdoctoral Research Fellow in DEPT. OF ELE ENGG & COMP SCI, SDSU, Brookings, SD  
Ph.D, M.Sc. in Electrical Engineering from SOUTH DAKOTA STATE UNIVERSITY, Brookings, SD.

### **Zairi Ismael Rizman**

Senior Lecturer, Faculty of Electrical Engineering, Universiti Teknologi MARA (UiTM) (Terengganu) Malaysia  
Master (Science) in Microelectronics (2005), Universiti Kebangsaan Malaysia (UKM), Malaysia. Bachelor (Hons.) and Diploma in Electrical Engineering (Communication) (2002), UiTM Shah Alam, Malaysia

### **Dr. D. Amaranatha Reddy**

Ph.D.(Postdoctoral Fellow,Pusan National University, South Korea), M.Sc., B.Sc. : Physics.

## **Dr. Dibya Prakash Rai**

Post Doctoral Fellow (PDF), M.Sc.,B.Sc., Working as Assistant Professor in Department of Physics in Pachhunga University College, Mizoram, India.

## **Dr. Pankaj Kumar Pal**

Ph.D R/S, ECE Deptt., IIT-Roorkee.

## **Dr. P. Thangam**

BE(Computer Hardware & Software), ME(CSE), PhD in Information & Communication Engineering, currently serving as Associate Professor in the Department of Computer Science and Engineering of Coimbatore Institute of Engineering and Technology.

## **Dr. Pradeep K. Sharma**

PhD., M.Phil, M.Sc, B.Sc, in Physics, MBA in System Management, Presently working as Provost and Associate Professor & Head of Department for Physics in University of Engineering & Management, Jaipur.

## **Dr. R. Devi Priya**

Ph.D (CSE),Anna University Chennai in 2013, M.E, B.E (CSE) from Kongu Engineering College, currently working in the Department of Computer Science and Engineering in Kongu Engineering College, Tamil Nadu, India.

## **Dr. Sandeep**

Post-doctoral fellow, Principal Investigator, Young Scientist Scheme Project (DST-SERB), Department of Physics, Mizoram University, Aizawl Mizoram, India- 796001.

## **Mr. Abilash**

MTech in VLSI, BTech in Electronics & Telecommunication engineering through A.M.I.E.T.E from Central Electronics Engineering Research Institute (C.E.E.R.I) Pilani, Industrial Electronics from ATI-EPI Hyderabad, IEEE course in Mechatronics, CSHAM from Birla Institute Of Professional Studies.

## **Mr. Varun Shukla**

M.Tech in ECE from RGPV (Awarded with silver Medal By President of India), Assistant Professor, Dept. of ECE, PSIT, Kanpur.

## **Mr. Shrikant Harle**

Presently working as a Assistant Professor in Civil Engineering field of Prof. Ram Meghe College of Engineering and Management, Amravati. He was Senior Design Engineer (Larsen & Toubro Limited, India).

## Table of Contents

S.No	Title	Page No.
1	<p><b>Study of Crystal Structure Profile Fitting of CuO for different Intensities of Gamma Radiation using Rietveld Refinement Method</b></p> <p><b>Authors:</b> Md. Mostafizur Rahman, Umme Kulsum Alo</p> <p> DOI: <a href="https://dx.doi.org/10.5281/zenodo.3692352">https://dx.doi.org/10.5281/zenodo.3692352</a></p> <p> <b>DIN Digital Identification Number:</b> IJOER-FEB-2020-1</p>	01-07
2	<p><b>Characterization of fine precipitates evolution in post ageing treatment after friction stir processed 7075 Al Alloy</b></p> <p><b>Authors:</b> P. K. Mandal, Jithin Devasia, Mebin T Kuruvila</p> <p> DOI: <a href="https://dx.doi.org/10.5281/zenodo.3692360">https://dx.doi.org/10.5281/zenodo.3692360</a></p> <p> <b>DIN Digital Identification Number:</b> IJOER-FEB-2020-2</p>	08-18
3	<p><b>Naphtol Oligomers and their Electroconductive Compositions</b></p> <p><b>Authors:</b> R.R. Guliyev, D.N. Aliyeva, R.A. Akhmedova, S.S. Mashayeva, Ch.O. Ismailova, B.A. Mamedov</p> <p> DOI: <a href="https://dx.doi.org/10.5281/zenodo.3692362">https://dx.doi.org/10.5281/zenodo.3692362</a></p> <p> <b>DIN Digital Identification Number:</b> IJOER-FEB-2020-4</p>	19-25
4	<p><b>Alzheimer's Detection By Using Neural Networks</b></p> <p><b>Authors:</b> Kavita Patil, Geetanjali Kale</p> <p> DOI: <a href="https://dx.doi.org/10.5281/zenodo.3692368">https://dx.doi.org/10.5281/zenodo.3692368</a></p> <p> <b>DIN Digital Identification Number:</b> IJOER-FEB-2020-5</p>	26-31
5	<p><b>ZnO Modified Bismuth Silicate Glasses Structural and Physical Properties</b></p> <p><b>Authors:</b> Md khademul Basher</p> <p> DOI: <a href="https://dx.doi.org/10.5281/zenodo.3692376">https://dx.doi.org/10.5281/zenodo.3692376</a></p> <p> <b>DIN Digital Identification Number:</b> IJOER-FEB-2020-6</p>	32-37

6	<p><b>Optimization of IBOM Power Plant (PG9171) using Fault Prediction on Gas Path Analysis</b> <b>Authors:</b> Nwaorgu.G.O, Pullah.A</p> <p> <b>DOI:</b> <a href="https://dx.doi.org/10.5281/zenodo.3692382">https://dx.doi.org/10.5281/zenodo.3692382</a></p> <p> <b>DIN Digital Identification Number:</b> IJOER-FEB-2020-7</p>	38-45
7	<p><b>A Study to Evaluate the Effectiveness of Self Instructional Module on Knowledge and Practice regarding Integrated Management of Neonatal and Childhood Illnesses among Staff Nurses working in Paediatric Wards of Selected Hospitals in Patna, Bihar</b> <b>Authors:</b> Rohit Tongariya</p> <p> <b>DOI:</b> <a href="https://dx.doi.org/10.5281/zenodo.3692386">https://dx.doi.org/10.5281/zenodo.3692386</a></p> <p> <b>DIN Digital Identification Number:</b> IJOER-FEB-2020-8</p>	46-52

# Study of Crystal Structure Profile Fitting of CuO for different Intensities of Gamma Radiation using Rietveld Refinement Method

Md. Mostafizur Rahman<sup>1</sup>, Umme Kulsum Alo<sup>2</sup>

Department of EEE, Islamic University Kushtia-7003, Bangladesh

**Abstract**— The study of crystal structure profile fitting described by Hugo Rietveld named Rietveld Refinement became popular for profile fitting and microstructural analysis. The Rietveld method refines user-selected parameters to minimize the difference between an experimental parameter (observed data) and a model based on the hypothesized crystal structure and instrumental parameters (calculated data). In this paper, profile fitting of CuO has been discussed for different intensities of XRD data. Here Goodness of fitting is kept 1-2. For different dose the goodness of fitting changes.

**Keywords**— CuO, Powder diffraction, gamma radiation.

## I. INTRODUCTION

### 1.1 Cupric Oxide (CuO)

During the past few years, the nano-semiconductors have proved itself beside the bulk semiconductors and have attracted extensive attention from scientists not only for the dramatic changing of their properties as a function of size, which is so significant for fundamental research, but also for their applications in different topics of technology as nano-electronics, photonics, optoelectronics, nano- medicine and nano-devices of renewable energy. It is well recognized that metal oxides have reached an important place in several areas of chemistry, physics and materials science. Currently, copper oxides, especially found a wide application domain in catalytic, field emissions, gas sensing, lithium batteries, and solar cells [2–6].

Metal oxide semiconductor thin films have been studied for their use in optoelectronic and photonics technology. Among the metal oxides, copper oxide (CuO) is a p-type semiconducting oxide material. CuO exhibits superior properties, including a direct band gap (~ 1.2 eV-2.1 eV), non-toxic nature, excellent chemical stability, cost effective synthesis, abundance in nature and reasonably good electrical properties [7-9]. CuO has received considerable attention for various applications, including gas sensors, biosensors, solar cells, batteries, magnetic storage materials, catalysts, diodes and transistors [8-12].

Interaction of radiant energy with matter, especially  $\gamma$ -radiation, is an enormously important from the view point of theory and practice. Gamma irradiation, the high energetic form of electromagnetic wave, causes two effects when interacting with materials: first, ionization which creates secondary reactions with ejected electrons and second, the atomic displacement which defects into atomic lattice. Irradiation of solids with high energy radiation, like  $\gamma$ - rays, electrons or neutrons expected to affect their optical, electrical and physical properties. The various researches illustrate that when solid state materials are exposed to ionizing radiation, their microstructural properties are altered. Numerous efforts have recently been made to investigate the influence of gamma radiation on different metal oxides and polymers. Copper Oxide is a group II-VI semiconductor with optical properties. It exhibits a wide variety of morphologies in the nano regime that can be grown by tuning the growth habit of the CuO crystal. There are two stable crystalline phases of the Copper oxide such as Cupric oxide (CuO) or tenorite and Cuprous oxide (Cu<sub>2</sub>O) or cuprite.

### 1.2 Crystal Structure Analysis

A crystal with its strictly periodic atomic structure represents a natural, very symmetrical three- dimensional diffraction grating for wavelengths of the order of the interatomic distances. Crystal structure analysis is thus based on the theories of symmetry (space groups) on the one hand and of interaction of radiation with solids (diffraction) on the other. The diffraction techniques, with the help of extensive computer calculations, lead to the atomic arrangements of crystalline materials. Depending on the problem, X-rays, electrons, or neutrons are used, which provide the electron-density, electrostatic potential density and nuclear density (also magnetic spin density) distribution, respectively, in a crystal[13].

All possible arrangements of atoms in crystals are governed by the 230 types of space groups, derived in 1890 by the crystallographer E.S. Fedorov and the mathematician A. Schoenflies. X-ray diffraction of crystals was discovered by the physicists M. Von Laue, W. Friedrich, and P. Knipping in 1912. In 1913- 1914, W.H. Bragg and W.L. Bragg first applied X-

ray diffraction to the experimental confirmation of the structures of single crystals of NaCl, Cu, diamond, etc. previously predicted by W. Barlow. The application of X-ray diffraction was extended to polycrystalline materials in 1916 by P. Debye and P. Sherrer. Details of the history of crystallography can be found in a recent Historical Atlas by I. Lima-de-Faria.

The power of a structure analysis of a synthetic crystal or a mineral and the reliability and accuracy of the results depend on many factors: sample quality, radiation source, apparatus and techniques available, especially for the measurement of the diffracted intensities. The first problem of a structural study is the determination of the symmetry and the lattice parameters of the crystal. The next step is the derivation of an atomic model. The structure is then refined from the diffraction data, taking into account the finer effects of the interaction between sample and radiation. The final stage is the crystallochemical analysis which comprises interpretation of the geometrical model, calculation of interatomic distances, valency angles, sizes, and orientations of thermal-motion ellipsoids and, finally, generation of visible structure models on a display or a plotter.

Further advances of the theory and the methods of structure analysis provide information not only on the geometry but also on more subtle features of the mineral structure, such as isomorphous replacement, disorder, variable atomic occupation of crystallographic sites, sizes and misorientation of mosaic blocks in single crystals, as well as thermal motion of the atoms including its anisotropy[13].

### 1.3 X-ray Powder Diffraction

Powder diffraction is a scientific technique using X-ray, neutron, or electron diffraction on powder or microcrystalline samples for structural characterization of materials. An instrument dedicated to performing such powder measurements is called a powder diffractometer. X-ray powder diffraction (XRD) is a rapid analytical technique primarily used for phase identification of a crystalline material and can provide information on unit cell dimensions.

Max von Laue, in 1912, discovered that crystalline substances act as three-dimensional diffraction gratings for X-ray wavelengths similar to the spacing of planes in a crystal lattice. X-ray diffraction is now a common technique for the study of crystal structures and atomic spacing.

X-ray diffraction is based on constructive interference of monochromatic X-rays and a crystalline sample. These X-rays are generated by a cathode ray tube, filtered to produce monochromatic radiation, collimated to concentrate, and directed toward the sample. The interaction of the incident rays with the sample produces constructive interference (and a diffracted ray) when conditions satisfy Bragg's Law ( $n\lambda=2d \sin \theta$ ). This law relates the wavelength of electromagnetic radiation to the diffraction angle and the lattice spacing in a crystalline sample. These diffracted X-rays are then detected, processed and counted. By scanning the sample through a range of  $2\theta$  angles, all possible diffraction directions of the lattice should be attained due to the random orientation of the powdered material. Conversion of the diffraction peaks to d-spacing allows identification of the mineral because each mineral has a set of unique d-spacing. Typically, this is achieved by comparison of d-spacing with standard reference patterns.

### 1.4 Rietveld Refinement

Rietveld refinement is a technique described by Hugo Rietveld for use in the characterization of crystalline materials. The neutron and x-ray diffraction of powder samples results in a pattern characterized by reflections (peaks in intensity) at certain positions. The height, width and position of these reflections can be used to determine many aspects of the material's structure.

The Rietveld method uses a least-squares approach to refine a theoretical line profile until it matches the measured profile. The introduction of this technique was a significant step forward in the diffraction analysis of powder samples as, unlike other techniques at that time; it was able to deal reliably with strongly overlapping reflections.

The method was first implemented in 1967 and reported in 1969 for the diffraction of monochromatic neutrons where the reflection-position is reported in terms of the Bragg angle  $2\theta$ . This terminology will be used here although the technique is equally applicable to alternative scales such as x-ray energy or neutron time-of-flight. [16]

The Rietveld method refines user-selected parameters to minimize the difference between an experimental pattern (observed data) and a model based on the hypothesized crystal structure and instrumental parameters (calculated pattern) [17].

The Rietveld method use the most physically-accurate model available for the intensities (the structure factor equation including iso or anisotropic thermal parameters, multiplicity, Lorentz and polarization factors, preferred orientation, absorption, extinction, anomalous scattering, etc.) but uses a phenomenological description of peak shapes (including both

instrumental or micro-structural factors affecting peak-shapes), and a physically sense-less background representation. Some of the corrections of the intensities (e.g. absorption) are not exact, though, they come from approximate models, but perform well when the effect of this factor is not very significant (and sometimes they are the only available model). Related methods used for determining intensities use the non- intensity-related parameters used in the Rietveld formula, to extract intensities from the fit.

The Rietveld Method, using an accurate representation of the intensities, performs well for structural analysis (refinement of structural model) and also quantitative phase analysis since relative intensities are correctly accounted for even in the presence of preferred orientation, micro-absorption, etc. that can be reasonably corrected with some physically-sensible models. Rietveld method as crystal structure refinement method is a method to check, how close to reality your guess is and to refine it so that the residual functions mentioned above will become as low as possible [18].

### 1.5 Full Prof Suite

The FullProf Suite (for Windows, Linux and macOS) is formed by a set of crystallographic programs (FullProf, WinPLOTR, EdPCR, GFourier, etc...) mainly developed for Rietveld analysis (structure profile refinement) of neutron (constant wavelength, time of flight, nuclear and magnetic scattering) or X-ray powder diffraction data collected at constant or variable step in scattering angle  $2\theta$ . The different programs can be run either in standalone form (from a console window or clicking directly in a shortcut) or from the interfaces WinPLOTR and/or EdPCR.

The programs within the FullProf Suite are distributed in the hope that they will be useful, but without any Warranty of being free of internal errors. In no event will the authors (or their institutions) be liable to you for damages, including any general, special, incidental or consequential damages arising out of the use or inability to use the programs (including but not limited to loss of data or data being rendered inaccurate or losses sustained by you or third parties or a failure of the program to operate with any other programs). The authors are not responsible for erroneous results obtained with the programs.

The first versions of the program FullProf were based on the code of the DBWS program which was also a major modification of the original Rietveld-Hewat program. The program FullProf has been re-written using the full capabilities of the new Fortran 95 standard during

1997-1998. It is progressively being transformed in a program based in the Crystallographic Fortran 95 Modules Library [3]. The program works with some allocatable arrays so the user can directly control the dimensions of important arrays at run time. In this paper we shall describe some elementary points concerning the methods implemented in the program and how to use it. For further details the user should consult the manual and tutorials. The Windows version of the program and all the suite of programs related to FullProf are now distributed within the FullProf suite installer (setup\_FullProf\_Suite.exe). This installer, additional documents and tutorials, can be found in the FullProf Web site [19-20]

## II. EXPERIMENTAL PART

### 2.1 Preparation of XRD data file

Here CuO powder is taken. Cu at wavelength  $1.540560 \text{ \AA}$  is taken. The data taken here is  $2\theta$ . Initial theta value 25.00 final  $2\theta$  value 80.00 and step used here the default step, i.e. 0.02.

### 2.2 Creating PCR file

XRD data file is taken in Microsoft .xlsx file. From that data file a .dat file is created to perform the operation. To develop the pcr file crystallographic information file is taken from crystallography open database for CuO. 12- Coefficient Fourier Cosine series is taken for background type. Phase of CuO is monoclinic and space group is C 2/c.

Rietveld refinement, profile matching and integrated intensity refinement of X- ray data was performed by using FullProf Suite Program. The pseudo-voigt function was used to refine CuO x-ray data applying C 2/c space group and monoclinic symmetry with Lau class 2 /m. The parameters thus obtained for the atomic positions of Cu and O element are presented in Table 1. Other parameters for example, full width at half maximum (FWHM), shape parameters, linear interpolations etc. were refined iteratively. All the diffraction peaks could be suitably indexed to the CuO teronite phase [13–15]. Refinement results reveal a monoclinic lattice structure (JCPDS 141–0254), having lattice constants  $a = 4.67910 \text{ \AA}$ ,  $b = 3.48050 \text{ \AA}$  and  $c = 5.11830 \text{ \AA}$  along with  $\alpha = \gamma = 90^\circ$ , and  $\beta = 98.5981^\circ$ .

**TABLE 1**  
**RIETVELD REFINEMENT PARAMETERS USED FOR ATOMIC POSITIONS IN FULLPROF SUITE PROGRAM**

Elements		x	y	z	Occ.	B
Atom#1	Cu	Cu	0.25000	0.25000	1.000	1.00
Atom#2	O	O	0.00000	0.41840	1.000	1.00

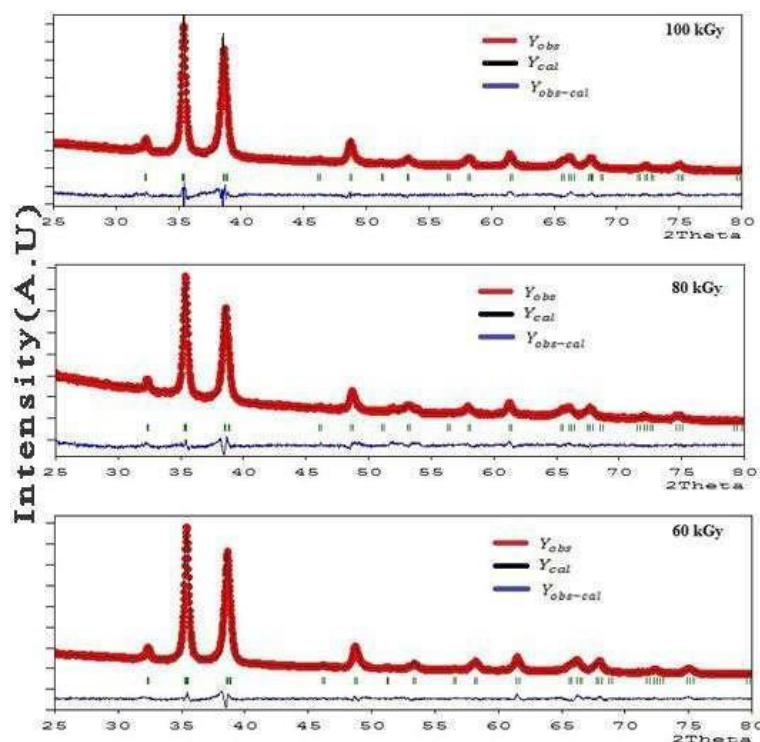


**FIGURE 1: Refined output graph for different intensities (60 KGy, 80 KGy, 100 KGy)**

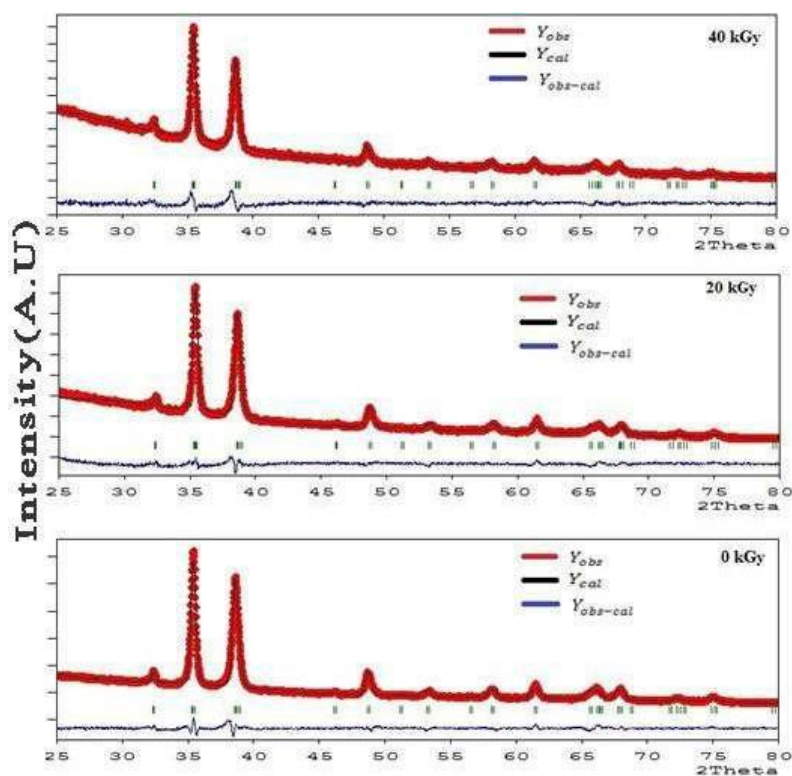


**FIGURE 2: Refined output graph for different intensities (0 KGy, 20 KGy, 40 KGy)**

### 2.3 Profile fitting

Here background points are refined first. Then instrumental components were refined. Profile and atomic positions were refined for the final step. In FWHM section U, V, W was refined first. And IG parameter is refined at the last step to get good fitting. All parameters were refined one by one first. Then Several Parameters were refined for various combinations of sequences to get good profile fitting.

The refined parameters are given in table-2:

**TABLE 2**  
**REFINED PARAMETERS**

Dose (kGy)	Lattice Parameter	R <sub>p</sub>	R <sub>wp</sub>	R <sub>esp</sub>	GOF	X <sup>2</sup>	R <sub>Brag</sub>	R <sub>F</sub>	Cell Volume
0	a = 4.67865 b = 3.42799 c = 5.12931 β = 99.3642	18.8	13.3	8.53	1.56	2.45	4.12	3.70	81.166
20	a = 4.67950 b = 3.43057 c = 5.12791 β = 99.3910	23.9	16.1	11.14	1.45	2.09	7.88	6.21	81.217
40	a = 4.68230 b = 3.42301 c = 5.12750 β = 99.4527	36.2	21.5	17.25	1.25	1.55	7.56	4.37	81.065
60	a = 4.68080 b = 3.42870 c = 5.12930 β = 99.3620	15.2	11.4	7.18	1.59	2.53	3.17	3.50	81.224
80	a = 4.70150 b = 3.44830 c = 5.15670 β = 99.3620	27.1	16.4	12.29	1.33	1.78	7.29	5.59	82.489
100	a = 4.67990 b = 3.42751 c = 5.12401 β = 99.3811	21	14.8	9.76	1.52	2.31	4.47	3.54	81.092

## III. RESULT AND DISCUSSION

### 3.1 Lattice constant

Lattice constant, or lattice parameter, refers to the physical dimension of unit cells in a crystal lattice. Lattices in three dimensions generally have three lattice constants, referred to as a, b, and c. However, in the special case of cubic crystal structures, all of the constants are equal and we only refer to a. Similarly, in hexagonal crystal structure, then a and b constants are equal, and we only refer to the and c constants. For monoclinic a, b, c are different. α, γ are 90° and β is different. A group of lattice constants could be referred to as lattice parameters. However, the full set of lattice parameters consist of the three lattice constants and the three angles between them [21].

### 3.2 Cell volume

The volume of the unit cell can be calculated from the lattice constant lengths and angles. If the unit cell sides are represented as vectors, then the volume is the dot product of one vector with the cross product of the other two vectors. The volume is represented by the letter V[21]. For the general unit cell.

$$V = abc\sqrt{(1 + 2\cos\alpha\cos\beta\cos\gamma - \cos^2\alpha - \cos^2\beta - \cos^2\gamma)}$$

For monoclinic lattices with α = 90°, γ = 90°, this simplifies to

$$V = abcsin\beta$$

For orthorhombic, tetragonal and cubic lattices with β = 90° as well, then V = abc.

For intensity 40 kGy unit cell volume is lowest, 81.065 Å<sup>3</sup>. For 80kGy cell volume is highest, 82.489.

### 3.3 R factors

Weighted sum of squares  $WSS = \sum_{i=1}^N [w_i (I_i^{exp} - I_i^{cal})]^2$

Where

$$w_i = \frac{1}{\sqrt{I_i^{exp}}}$$

R structure factor:  $R_f = \frac{\sum |(I_k^{obs})^{\frac{1}{2}} - (I_k^{ca})^{\frac{1}{2}}|}{\sum (I_k^{obs})^{\frac{1}{2}}}$  where  $I_k$  is the intensity of  $K^{th}$  reflection at the end of refinement cycle.

R Bragg factor:  $R_{Bragg} = \frac{\sum |I_k^{obs} - I_k^{cal}|}{\sum I_k^{obs}}$

R weighted pattern:  $R_{wp} = \left[ \frac{\sum [w_i (y_i^{obs} - y_i^{cal})^2]}{\sum w_i (y_i^{obs})^2} \right]^{1/2}$  where  $y_i$  = gross intensity at  $I^{th}$  step

Goodness of fit:  $\frac{R_{wp}}{R_{exp}}$

$$X^2 = \left( \frac{R_{wp}}{R_{exp}} \right)^2$$

$R_{exp} = [N - P] / \sum w_i (y_i^{obs})^2 ]^{1/2}$  where  $N$  = Number of points,  $P$  = number of parameters [22]

## IV. CONCLUSION

Materials are essential to our technological society: Semiconductors in the electronic industry, zeolites as catalysts in the petrochemical industry, ceramics in medicine and engineering and possibly in the future, high –temperature superconductors in electrical engineering.

In order to understand the properties of these materials and to improve them, the

Atomic structure has to be known. An effective way to do this is by means of diffraction techniques using neutrons from nuclear reactors and particle accelerators or X-rays from X-ray tubes and synchrotrons. The Single crystal diffraction technique using relatively large crystal of the material, gives a set of separate data from which the structure can be obtained.

However, most materials of technical interest cannot grow large crystals, so one has to resort to the powder diffraction technique using material in the form of very small crystallites. The drawback of this conventional powder method is that the diffraction peaks grossly overlap, thereby preventing proper determination of the structure. The "Rietveld Method" creates a virtual separation of these overlapping peaks, thereby allowing an accurate determination of the structure. The method has been so successful that nowadays the structure of materials, in the form of powders, is routinely being determined, nearly as accurately as the results obtained by single crystal diffraction techniques. An even more widely used application of the method is in determining the components of chemical mixtures. This quantitative phase analysis is now routinely used in industries ranging from cement factories to the oil industry.

## V. FUTURE WORK

Our aim is to lesson to the difference the calculated value of R factor and the expected value of R factor. If the difference is less, the structure of new compound will be more accurate. Then we easily characterize the new compound. The difference can be lessening using linear background. Crystallite size, strain and microstructure analysis of CuO may be done in future.

**REFERENCES**

- [1] S.Govindasamy,T.marimuthu,M.S.Vaiyazhipalayam,Optical,Catalytic and antibacterial properties of phytofabricated CuO nanoparticles using tocoma castanifolia leaf extract,Optik 127(2016) 7822-7828.
- [2] zhu yW,Yu T,Cheong FC,Xu XJ,Lim CT ,TanVBC ,et al.large-scale synthesis and field emission properties of vertically oriented CuO nanowire films,Nanotechnology 16 (2005) 88-92.
- [3] Jiatao Zunfeng Liu, Qing Peng, Xun Wang, and Yadong Li, Nearly monodisperse Cu<sub>2</sub>O nanospheres: preparation and applications for sensitive gas sensors ,Chem, Mater, 18 (2006) 867-871.
- [4] Shuyan Gao,Shuxia Yang,Jie Shu, Shuxia zhang ,Zhengdao Li and kai Jiang ,Green fabrication of hierarchical CuO hollow micro/nanostructures and enhanced performance as electrode materials for lithium-ion batteries J.Phys.Chem.C.112(2008)19324-19328.
- [5] Sajad Hussain ,Chuanbao Cao, Ghulam Nabi,Waheed S.Khan, Muhammad Tahir, Muhammad Tanveer,Optical and electrical.
- [6] K.Mageshwari, R.Sathyamoorthy ,Physical properties of nanocrystalline CuO thin films prepared by the SILAR method .Mater . Sci .Semicond. Proc. 16(2013) 337-343.
- [7] F.Bayansal,B.Sahin, M.Yuksel, N. Biyikli, H.A. cetinkara, H.S. Guder, Influence of coumarin as an additive on CuO nanostructures prepared by successive ionic layer adsorption and reaction ( SILAR) method .J.Alloys Compd. 566 ( 2013) 78-82.
- [8] N.Mukherjee, B .Show , S.K. MAji,U .Madhu,S.k. Bhar ,B.C.Mitra,G.G.Khan,A.Mondal,CuO nano-whiskers: Electrodeposition, Raman analysis, Photoluminescence study and photocatalytic activity ,Mater.. Letters 65 (2011) 3248-3250.
- [9] H.T.Hsueh,S.J Chang,F.Y.Hung,T.Y.Tsai,W.Y.weng,C.L.Hsu, B.T.dai,CuO nano-wire based humidity sensors prepared on glass substrate .Sens Actuators B.156 (2011) 906-911.
- [10] X.Wang,C.Hu,H.Liu,G.Du.X.He,Y.Xi,Synthesis of CuO nanostructures and their applications for nonenzymatic glucose sensing sens.Actuators B. 144(2010) 220-225.
- [11] [https://www.malvernpanalytical.com/en/products/category/x-ray-diffractometers?creative=335131773810&keyword=%2Bpowder%20%2Bdiffraction&matchtype=b&network=g&device=c&gclid=CjwKCAiAy9jyBRA6EiwAeclQhOAvPEhoD5IHYYTlqL38gpn\\_FDxC2WRpuYr28dbLBQnb5kUTUfPII8hoCFrIQAvD\\_BwE](https://www.malvernpanalytical.com/en/products/category/x-ray-diffractometers?creative=335131773810&keyword=%2Bpowder%20%2Bdiffraction&matchtype=b&network=g&device=c&gclid=CjwKCAiAy9jyBRA6EiwAeclQhOAvPEhoD5IHYYTlqL38gpn_FDxC2WRpuYr28dbLBQnb5kUTUfPII8hoCFrIQAvD_BwE).
- [12] [https://en.wikipedia.org/wiki/Powder\\_diffraction](https://en.wikipedia.org/wiki/Powder_diffraction).
- [13] [https://en.wikipedia.org/wiki/Lattice\\_constant](https://en.wikipedia.org/wiki/Lattice_constant).
- [14] <https://www.sciencedirect.com/topics/biochemistry-genetics-and-molecular-biology/rieveld-refinement>.
- [15] T.Jarlborg, Effects of spin-phonon interaction within the CuO plane of high -TC Superconductors .Physica C.454(2007) 5-14.

# Characterization of fine precipitates evolution in post ageing treatment after friction stir processed 7075Al Alloy

P. K. Mandal<sup>1</sup>, Jithin Devasia<sup>2</sup>, Mebin T Kuruvila<sup>3</sup>

Department of Metallurgical and Materials Engineering, Amal Jyothi College of Engineering, Kanjirappally-686518, Kerala, India

**Abstract**—The effect of post ageing treatment (140°C for 2h) on the microstructure and mechanical behaviour of FSPed 7075 Al alloy has been studied by Optical microscopy (OM), Field emission scanning electron microscopy (FESEM), Differential scanning calorimetry (DSC), Scanning electron microscopy (SEM), Transmission electron microscopy (TEM), and mechanical properties. Friction stir processing (FSP) is a solid-state surface modification technique to apply for cast aluminium alloys. FSP has a similar metal working principle like FSW (friction stir welding). The alloy has strong age-hardening response with scandium (Sc) inoculated Al-Zn-Mg alloy, on the other hand novelty of FSP only few studies have been carried out to the effect of post ageing treatment on the microstructure, size, morphology and fine dispersion of coherent Al<sub>3</sub>Sc(L1<sub>2</sub>) type precipitates or η-phases and its mechanical properties of friction stir processed 7075 Al alloy. The FSPed enhances grain boundary (GB) formation and increases suitable sites for the precipitation of nucleation in post aged 7075 Al alloy. The mechanical properties have been evaluated such as proof strength ( $\sigma_{0.2}$ ) of 122.9 MPa, ultimate tensile strength ( $\sigma_u$ ) of 256.4 MPa, ductility ( $\delta$ ) of 8.6%, Vicker's hardness in stir zone of 101 HV, strain hardening exponent (n) of 1.82, and heat input during FSPed of 2.15 kJ/mm, respectively.

**Keywords**—Al<sub>3</sub>Sc and η precipitates, FSP, mechanical properties, post aged 7075 Al alloy, TEM.

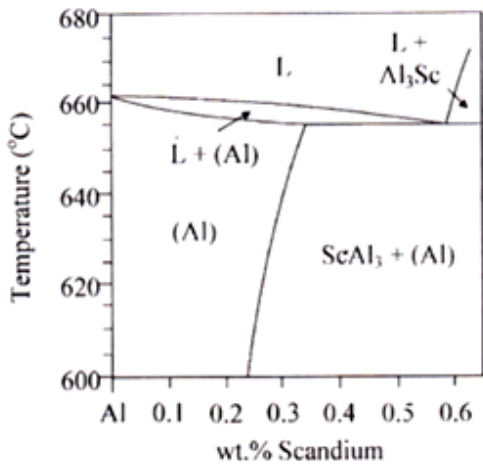
## I. INTRODUCTION

The high strength Al-Zn-Mg alloy (7075 series) was widely used due to their spontaneous age-hardening ability, good corrosion resistance and excellent mechanical properties obtained through fine precipitation of a homogeneous distribution of dispersoid particles [1-3]. Further, friction stir processing (FSP) has been adapted for surface modification technology, especially for fabrication process, processing and synthesis of materials. It has great advantages including surface modification for microstructural evaluation, adjusting mechanical properties by optimizing tool design and process parameters [4, 5]. FSP can be exploited not only by controlling process parameters but also by using an Al-Zn-Mg-Sc alloy contains thermally stable precipitates or dispersoids, also can precipitate out such particles during processing thereby retarding the uncontrolled grain growth. Hence, fine-grained microstructure may be obtained by controlling the grain growth or fine distribution of Al<sub>3</sub>Sc precipitates during FSPed plus post ageing treatment [6-8]. Ma and Mishra et al. [2005] demonstrated the possibility of achieving grains larger than 1 μm under any other processing conditions. As well, Nascimento et al. [2009], Kwon et al. [2003], and Colligan et al. [1999] insight studied on FSP technique successfully to produce fine-grained structure and surface composite of aluminium alloys. More emphasis has been given on the mechanism of dynamic recrystallization in Al-Zn-Mg-Sc alloy and the role of coherent precipitates in the formation of high temperature (450-550°C) FSPed microstructure. In addition, heat input (2.15 kJ/mm) is the main criterion for the energy transformation during FSPed [9-11]. The characteristics of fine-grained microstructure obtained through FSP are entirely different from any other conventional severe plastic deformation (SPD) techniques. Thus, the major processing parameters are the tool rotation and traverse speed, the axial force, tilt angle and the proper tool design have been well documented by several authors. The possible strengthening mechanism can be attributed to formation of fine grain and subgrain structure and dislocation distribution of the modified surface [12-14]. The objective of the present work is to characterize the precipitates in friction stir processed Al-Zn-Mg-Sc alloy then post ageing treatment at 140°C for 2h using OM, FESEM, SEM, DSC, and TEM analysis. To investigate the effects of scandium on mechanical properties of FSPed aluminium alloy after post ageing treatment (140°C for 2h).

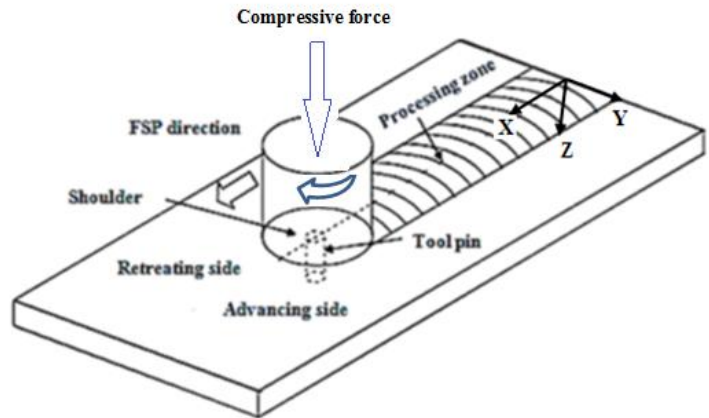
## II. EXPERIMENTAL PROCEDURE

The muffle furnace was used to melt the 7075 Al alloy, and subsequently Sc added an inoculation effect in-form of Al-2wt % Sc master alloy through foundry route. The melt was carried out in a mild steel mould (200×90×24mm<sup>3</sup>) and melting temperature fixed at 780°C. The pieces of aluminium around 3.5 kgs, kept into a graphite crucible, and its put into a muffle

furnace and heated upon 2. 5h until fully melt it. Then, pieces of Al-2wt. %Sc master alloy added in proportion of Sc (generally 50% recovery) into liquid bath and kept for another 30 mins for grain refinement with the carefully adjusting the fading. Then the red hot crucible was taken out from the furnace, soon Mg and Zn were added in liquid bath gradually with carefully. Slag removed from the top of the liquid bath and it was poured into metallic mould quickly. The hot mould immediately put into the water bath for faster cooling. The size of cast plate was obtained of  $150 \times 90 \times 8 \text{ mm}^3$  from main coupon. The cast metal had been analyzed by ICP-AES (inductively coupled plasma atomic emission spectroscopy) and AAS (atomic absorption spectroscopy) methods and the following composition is given in weight percentage of 7075 Al alloy: Zn(5. 95%), Mg(2. 90%), Sc(0. 45%), Si(0. 10%), Fe(0. 10%), and balance of Al. While, total Zn and Mg content is 8. 85% and Zn to Mg ratio of 2:1 and Sc content 0. 45% (hypoeutectic) as shown Figure 1(a). The cast plate was preferred for solution treatment at  $465^\circ\text{C}$  for 1h then followed by immediately quenching in water to room temperature is called  $T_4$  heat treatment. After completing the  $T_4$  heat treatment, the same specimens were preferred for artificial ageing at  $120^\circ\text{C}$ ,  $140^\circ\text{C}$ , and  $180^\circ\text{C}$  for 14h each slot, respectively. This ageing kinetics has been evaluated through Vicker's hardness (FIE VM50 PC) measurements with 10 kgs. load and 15s dwell time. Each time six indentations were taken quickly on specific sample which carried out from the heating furnace and obtained average value for plotting ageing time vs. Vicker's hardness as shown in Figure 8(a-b). The  $T_4$  plate was preferred for double-pass FSP with fixed parameters are 1000 rpm, 70 mm/min traverse speed and specified tool design, then its post aged at  $140^\circ\text{C}$  for 2h. It is clear that post ageing treatment conducted after completion of double-pass FSPed plate. Then, the samples were picked up from SZ (stir zone) and preferred for characterizations such as OM, FESEM, SEM, DSC, TEM, and mechanical testing. Samples for optical metallography were cut into small pieces for cold mounting then polished by emery papers from course to finer grades and followed by velvet cloth polishing with alumina powder slurry to obtain mirror finish. The FESEM with EDS analysis (QUANTA 200F, 30kV) was determined for GB segregations of experimental samples. The DSC (EXSTAR TG/DTA 6300) run was carried out of experimental samples for revealing semi-solid state precipitation and dissolution reactions by using a nitrogen atmosphere and a constant heating rate of  $10^\circ\text{C}/\text{min}$  till  $650^\circ\text{C}$ . The polished samples were cleaned by water then dried and etched in Keller's reagent (1ml HF + 1. 5ml HCl + 2. 5ml HNO<sub>3</sub> + 95ml H<sub>2</sub>O) for optical microscopy. An optical microscope (LEICA DMI 5000M) was used to obtain microstructure images. TEM with SAD studies were performed using a Techai G<sup>2</sup> 20 S-TWIN at 200kV. The TEM thin foil (80 to 100  $\mu\text{m}$ ) specimens were prepared through polishing by fine emery papers and subsequently through conventional twin-jet electropolishing technique using a 30% HNO<sub>3</sub> + 70% CH<sub>3</sub>OH solution at  $-20^\circ\text{C}$  and 20V. After electropolishing samples (3 mm diameter and contain center hole) have preserved in vacuum desiccator for TEM analysis. A vertical milling machine was used for surface modification of cast aluminium plate by FSP. The FSP machine consists of 3 H. P. motor mounted on top with option for 8 variable spindle speeds. The spindle speed selection was done by shifting the rubber belt to the desire groove of the four-step cone-pulleys. A hydraulic power pack controlled the movement of a semi-automatic adjustable working table. A constant axial compressive force of 15 kN was fixed before start the FSP machine and all process parameters are shown in Table 1. The processing plate ( $150 \times 90 \times 8 \text{ mm}^3$ ) had fixed on the working table with the proper fixer as shown in Figure 1(b) and subsequently a tool configuration as shown in Figure 1(c), a macrostructure of double-pass FSPed plate (Figure 1. d), a macrostructure of double-pass FSPed as showing of stir zone (Figure 1. e), and a bunch of tensile test samples as shown in Figure 1(f), respectively. The tensile samples were picked up from SZ of double-pass FSPed as shown in Figure 1(d) and Figure 1(f). It has to mention that the tool design is the most important parameter of the FSP. The tool made of heat treated martensitic stainless steel (211 HV) with cylindrical shape of shoulder and oval shape of pin tip. The tool has three main functions likely to (i) transform the applied load to the work piece, (ii) heat is generated by friction between the tool shoulder and work piece, and by the plastic deformation of the work piece, and (iii) stirring and mixing the material around it. The tool was rotated clockwise direction at the speed of 1000 rotations per min with the rotating pin inserted into the work plate. The rotating tool was then traversed in the X-axis direction perpendicular to the Y-axis direction of the work plate at a constant speed of 70 mm/min. The tool rotation Z-axis was held perpendicularly to the work plate. All FSP experiments were carried out through the double-pass and only 35% deviation in between two passes with the same direction during processing. The nugget zone or stir zone created during processing in middle place of working plate with adjacent right side and left side is called advancing side and retreating side, respectively. After FSPed, all plates were preferred for post ageing treatment at  $140^\circ\text{C}$  for 2h in muffle furnace with controlled temperature. Then, the processed plate preferred for machining along the SZ to preparation for tensile samples (ASTM: E8/E8M-11) [15]. The tensile testing was carried out at a cross head speed of 1 mm/min in a Universal Testing Machine (UTM) (25 kN, H25, K-S, UK) in room temperature. The averages of five samples were tested for each case for evaluating of tensile properties and the results are shown in Table 2.



(a)



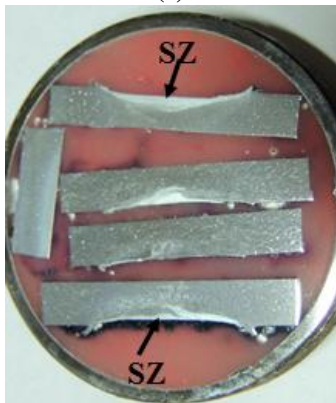
(b)



(c)



(d)



(e)



(f)

**FIGURE 1: (a) The Al-Sc equilibrium phase diagram, (b) Schematic diagram of double-pass FSPed set-up (plate size:150×90×8mm<sup>3</sup>), (c) Tool configuration, (d) Double-pass FSPed plate (each impression contain double-passFSP), (e) A bunch of macrostructures of double-pass FSPed as showing of stir zone (SZ), (f) A bunch of tensile test samples were collected from stir zone (SZ).**

**TABLE 1  
PROCESSING PARAMETERS OF DOUBLE-PASS FSP<sub>ED</sub>.**

FSP parameters and the tool design						
Tool rotation speed(rpm)	Work piece travel speed (mm/min)	Friction pressure (up-setting force) (kN)	Pin angle( °)	Pin root dia. and ht. (mm)	No. of passes	Plate dimensions
1000	70	15	2.5	5.0, 3.5	two	150×90×8 mm <sup>3</sup>

### III. RESULTS AND DISCUSSION

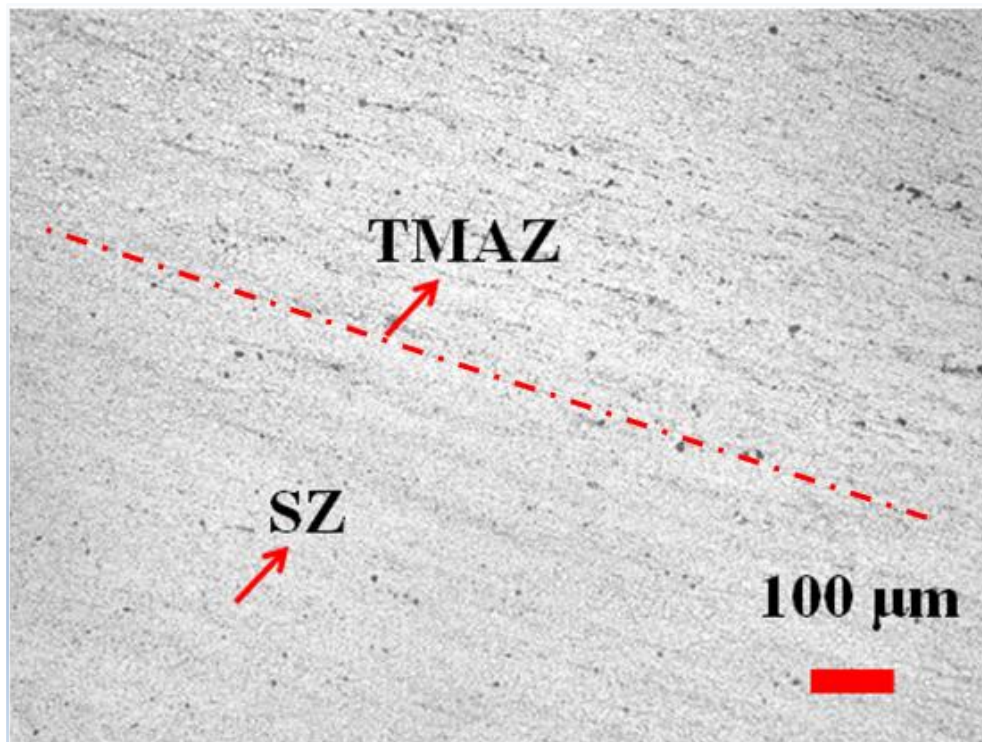


**FIGURE 2: Optical micrograph of 7075 Al alloy at  $T_4$ +FSPed+Post-aged at 140°C for 2h condition. (1000 rpm and 70 mm/min)**

The strength of the fine-grain aluminium alloy after FSPed from SZ can be calculated from the Hall-Patch relationship:  $\sigma_y = \sigma_0 + \frac{k}{\sqrt{d}}$ , where  $\sigma_y$  is the yield strength (0.2% proof strength) as 143.6 MPa,  $\sigma_0$  is the friction strength,  $d$  is the grain size as  $5.31 \pm 1.0 \mu\text{m}$ , and  $k$  ( $0.22 \text{ MPa}\sqrt{\text{m}}$ ) is a constant for a particular material. The grain size measured by Image J software, and 0.2% proof strength as experimental value is 143.6 MPa (Table 2), then from the above equation  $\sigma_0$  is calculated as 143.5 MPa, it seems both of the strengths are almost same values [16, 17]. It has to mention that the increasing strength as a result of finer grains have to more number of grain boundaries in SZ after FSPed plus post aged 140°C for 2h. There are significant improvements of mechanical properties have realized through only a double-pass of FSPed. The deformed alloy in the SZ experiences adequately high temperatures (450-500°C) leading to dynamic recrystallization occurs by nucleation of very fine grains at the boundaries of the severely deformed grains in SZ. According to Jata et al. [2000] suggested that the low angle boundaries at the initial stage of parent metal are replaced by the high angle boundaries in SZ by continuous rotation of the original low angle boundaries during FSPed [18-20]. Many other researchers have been reported that the fraction of high angle grain boundaries (85-90%) is also responsible for formation of the fine and equiaxed grains produced by FSPed aluminium alloys. This high-volume fraction of high angle grain boundaries can encourage grain boundary sliding, which is estimated as the leading deformation mechanism for higher ductility and superplasticity [21, 22]. It is generally believed that achieving fine-grained sizes using FSPed is easier in this alloy that contain large number of second phase particles as  $\eta$ - $\text{MgZn}_2$  and numerous dispersoids as  $\text{Al}_3\text{Sc}$  in matrix. These precipitates have different interface energy that can improve the tensile properties by orientation and the post ageing treatment. Also, these particles can restrict grain growth due to their pinning effect can play the major role in grain size evolution in FSPed alloy. It is also able to calculate the heat input of 2.15 kJ/mm during FSPed at fixed parameters as shown Table 1. Figure 2 shows optical microstructure of FSPed aluminium alloy exhibited clearly two different regions such a TMAZ which average grain size of  $6.96 \pm 2.1 \mu\text{m}$  corresponding created several black spots average size of  $10.09 \pm 2.1 \mu\text{m}$ , similarly SZ average grain size of  $5.31 \pm 1.0 \mu\text{m}$  corresponding created several black spots average size of  $3.42 \pm 1.62 \mu\text{m}$ , respectively. It has to conclude that these black spots generated due to Zn vaporization effect during FSPed and its deleterious effects decrease mechanical properties mainly for large size of black spots and several hair line cracks generated due to torsional effects of rotating tool in TMAZ in matrix [23, 24]. Figure 3 shows the FESEM with EDX analysis exhibited several white spots mainly for  $\text{Al}_3\text{Sc}$  agglomeration and  $\text{Al}_2\text{Zn}_3\text{Mg}_3$  phases with ample impurities (Fe+Si=6.89 wt. %) content as well as Sc content of 2.89 wt. % in the matrix. Figure 4 shows the DSC curve of alloy. There are five peaks in the curve, which are marked by letters A, B, C, D, and E, respectively.

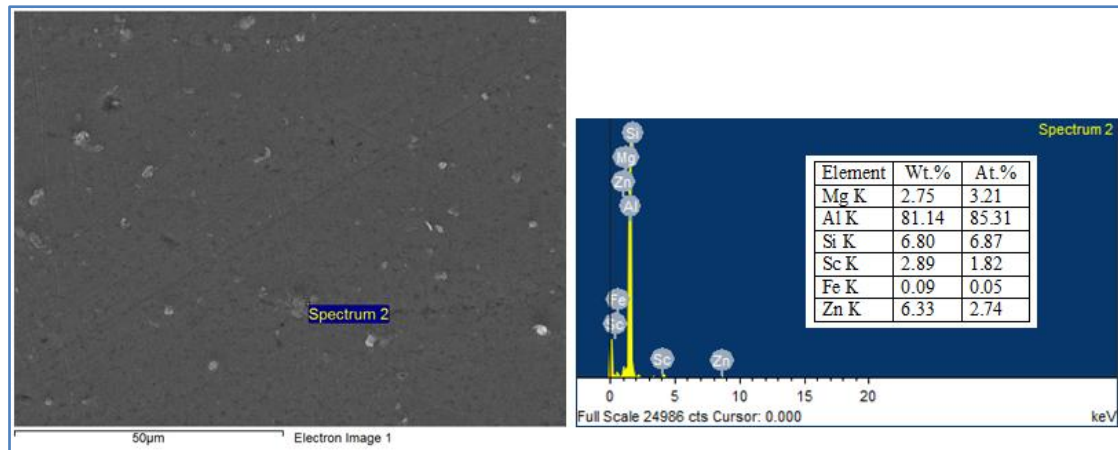


**FIGURE 3: FESEM micrograph with EDX analysis of 7075 Al alloy at  $T_4$ +FSPed+ Post-aged at  $140^\circ\text{C}$  for 2h. (1000 rpm and 70 mm/min)**

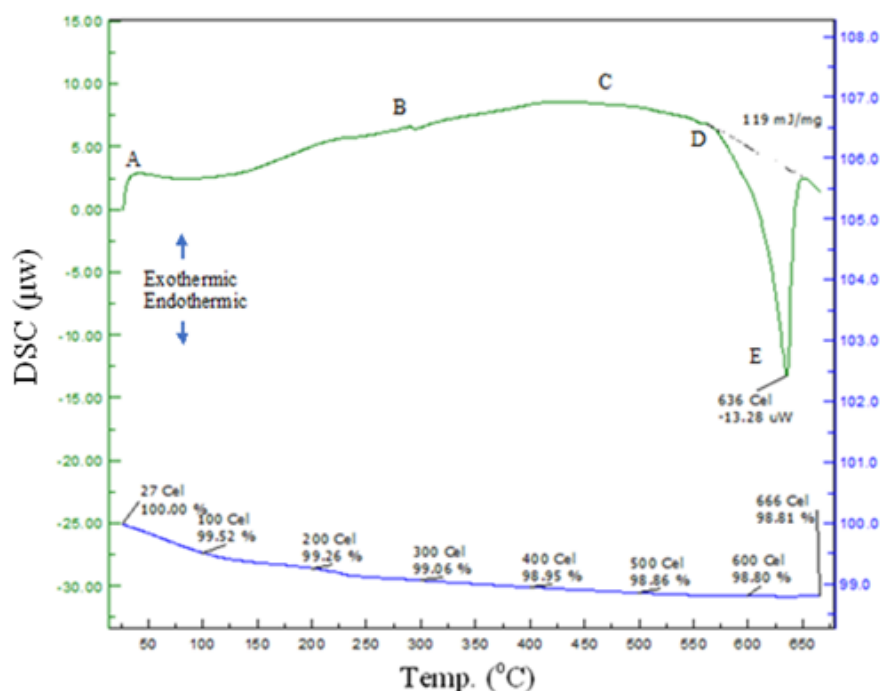


**FIGURE 4: DSC analysis (heating rate  $10^\circ\text{C}/\text{min}$ ) of 7075 Al alloy at  $T_4$ +FSP+Post-aged at  $140^\circ\text{C}$  for 2h. (1000 rpm and 70 mm/min)**

The first peak indicates at the A point of exothermic reaction occur at around  $25\text{-}30^\circ\text{C}$ , which may refer for GP zones formation in matrix of alloy. The second peak indicates at the B point little deflection of endothermic reaction occur at around  $285\text{-}295^\circ\text{C}$ , which may refer initial phases are (GP zones,  $\eta$ -metastable phases) dissolve in matrix during DSC run at  $10^\circ\text{C}/\text{min}$ . The third peak indicates at the C point of exothermic reaction occur at around  $560\text{-}570^\circ\text{C}$ , which may refer for reprecipitation of metastable phases of  $\eta$ ,  $\eta$  and  $\text{Al}_3\text{Sc}$  particles and formation of high volume fraction of the precipitates, but it has offered hardening effect till D point (endothermic reaction) in the DSC curve. The alloy is prone of endothermic reaction occur at  $636^\circ\text{C}$ , which may refer for completely dissolved of all hardening phases and coarsening effect of  $\text{Al}_3\text{Sc}$  particles in matrix [25, 26]. Figure 5(a) shows TEM micrograph with the SAD analysis of  $T_6$  aluminium alloy revealed a large number of coherent secondary  $\text{Al}_3\text{Sc}$  particles (marked by red arrows and size  $43.38 \pm 10.23$  nm) of fine precipitates are distributed homogeneously in matrix. It is clearly visible at the grain boundary regions for high magnification (100 nm) of  $T_6$  aluminium alloy (Figure 5. b). Besides the spots of  $\text{Al}_3\text{Sc}$  particles there are some fine precipitates for  $\eta$  phases in the matrix. These coherent  $\text{Al}_3\text{Sc}$  particles ( $33.81 \pm 6.58$  nm) have a good thermal stability and drastic anticrystallization effect. It can be seen that ageing strengthening effect of alloy is very strong. Initial stage of ageing, the strength of alloy increases rapidly then the peak can be achieved at  $140^\circ\text{C}$  for 6h ageing time. Therefore,  $\text{Al}_3\text{Sc}$  particles and  $\eta$  phases are the main strengthening precipitates in peak-aged aluminium alloy.

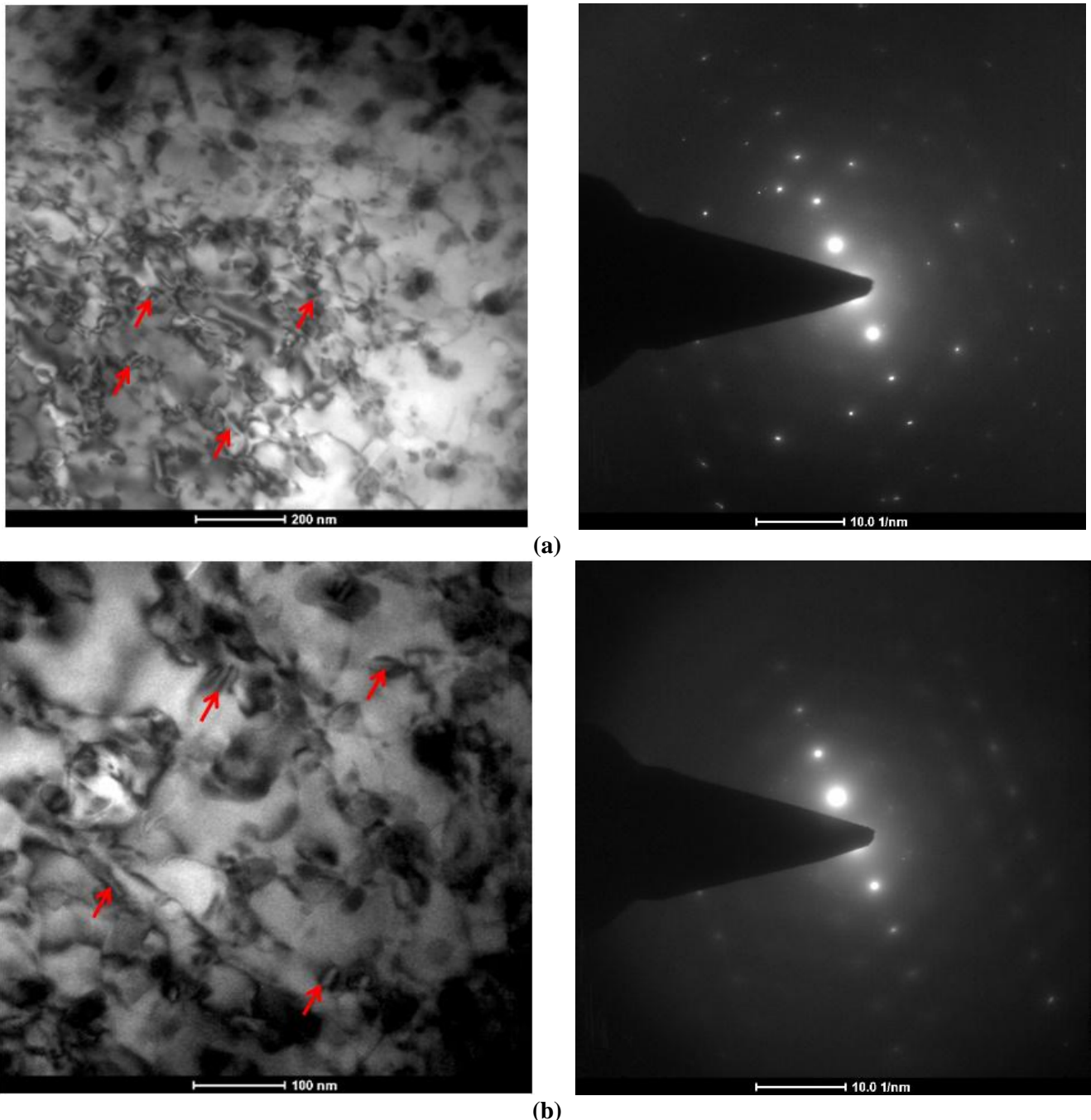
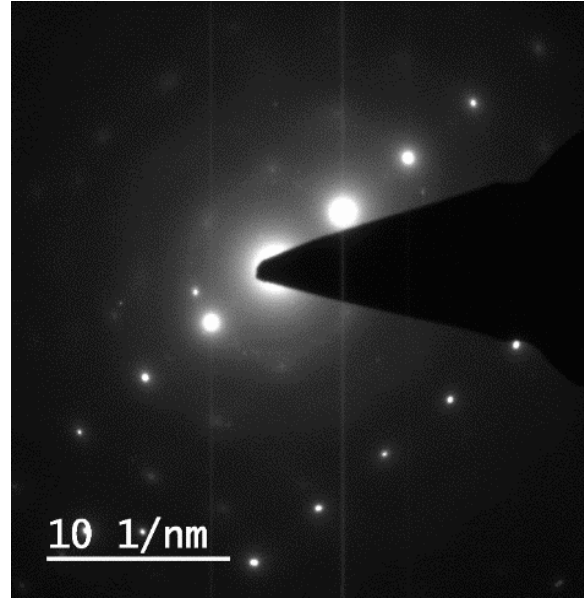
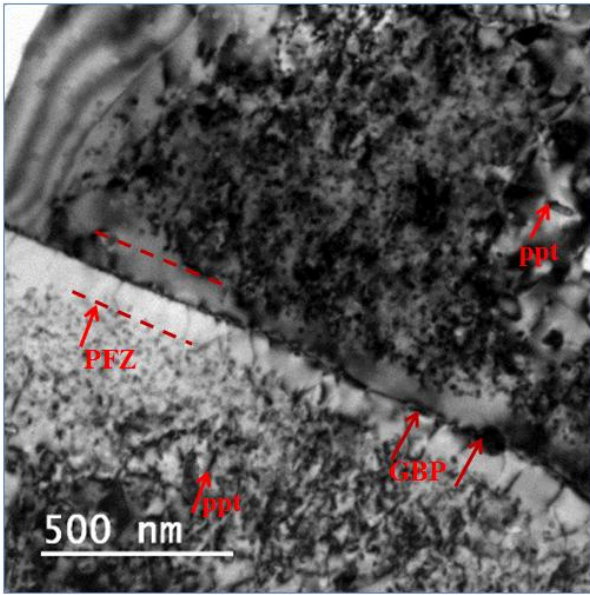
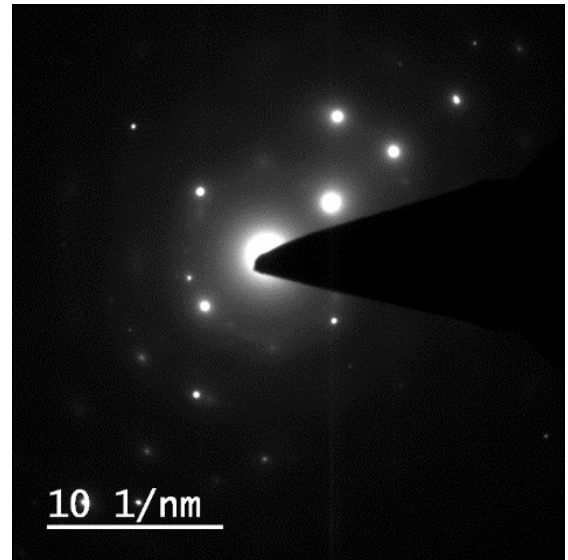
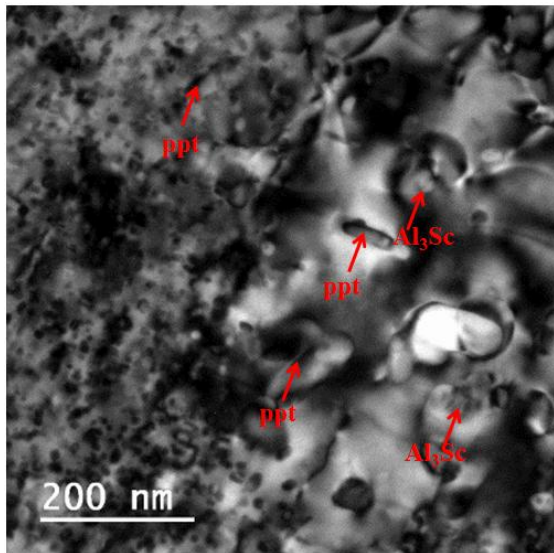


**FIGURE 5: TEM micrographs with SAD patterns of 7075 Al alloy aged at 140°C for 6h ( $T_6$ ): (a) at low magnification (200 nm), (b) at high magnification (100 nm).**

Figure 6(a-b) shows TEM micrographs with the SAD analysis of aluminium alloy exhibited fine homogeneous precipitates with narrow zone of PFZ (precipitation free zone) and fine precipitates embedded on the grain boundary (GB) in the matrix. Mostly two types of precipitated particles are dominated likely to GBP (grain boundary precipitates) of  $Al_3Sc$  type on the grain boundary and needle shape ppt (precipitates) of  $\eta$ -type in the matrix. According to the micrographs of TEM analysis, the mixture of GP zones and  $\eta$ -type ( $71.68 \pm 9.44$  nm) and  $Al_3Sc$  type are dominant precipitates of the alloy in this post-ageing state. So, the small spherical precipitates are mainly GP (I, II) zones ( $15.04 \pm 3.30$  nm) and elongated or needle shape ppt (precipitates) are the  $\eta$ -type ( $52.32 \pm 16.52$  nm) and cauliflower shape is  $Al_3Sc$  type ( $33.43 \pm 11.02$  nm) in the matrix (Figure 6. b). The GBP of the studied alloy is form about  $24.93 \pm 5.1$  nm thick with  $54.32 \pm 16.28$  nm in length and exist in the PFZ ( $173.15 \pm 7.36$  nm) at the grain boundary discontinuously (Figure 6. a). The TEM micrographs observation clearly indicated that the during FSPed plus post ageing can precipitate the nanometer-sized precipitates (GP zones,  $\eta$ ,  $MgZn_2$  and  $Al_3Sc$ ) have the strong precipitation strengthening for the alloy [27-29].

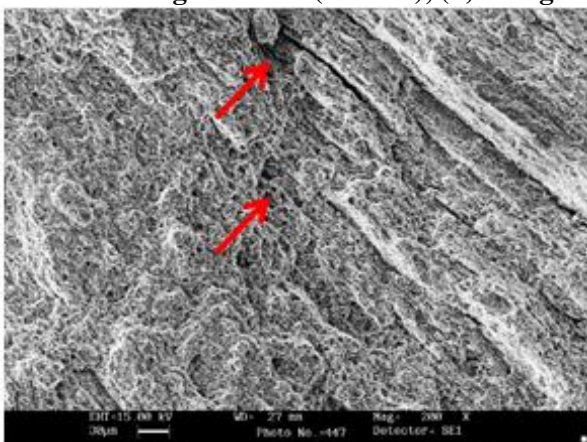


(a)

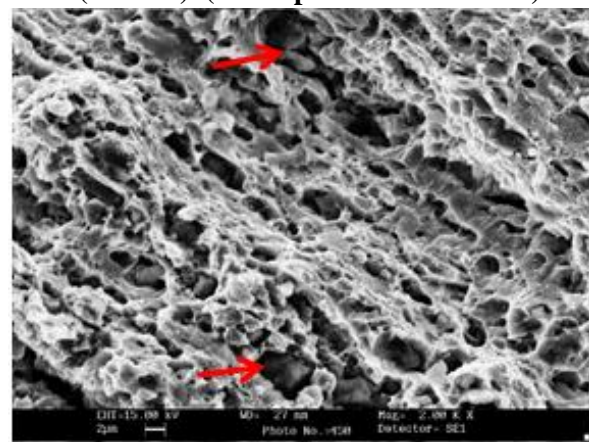


(b)

**FIGURE 6: TEM micrographs with SAD patterns of 7075 Al alloy (T<sub>4</sub>+FSP+Post-aged at 140°C for 2h): (a) at low magnification (500 nm), (b) at high magnification (200 nm). (1000 rpm and 70 mm/min).**



(a)



(b)

**FIGURE 7: SEM tensile fractographs of 7075 Al alloy (T<sub>4</sub>+FSP+Post-aged at 140°C for 2h): (a) at low magnification (200X), (b) at high magnification (2000X). (1000 rpm and 70 mm/min)**

Figure 7 shows SEM fractograph at different magnifications exhibited mainly ductile mode of fractures propagation taking place upon transgranular manner in matrix. In the low magnification (200X) fractograph shows crack is originated from dip notch like hole (indicated by red arrows) propagating further with branches throughout the matrix. In Figure 6(b) shows the TEM analysis indicated agglomeration of coarse precipitates, defects like Zn vaporization are main causes of failure. In the high magnification (2000X) fractograph shows clear indication of many crack propagation points due to coarse precipitates (indicated by red arrows) like  $\text{Al}_3\text{Sc}$  or  $\text{Al}_2\text{Mg}_3\text{Zn}_3(\text{T})$  agglomeration lead to crack extension to forward in transgranular manner and results to formation of ridge like segments in the matrix [30-32].

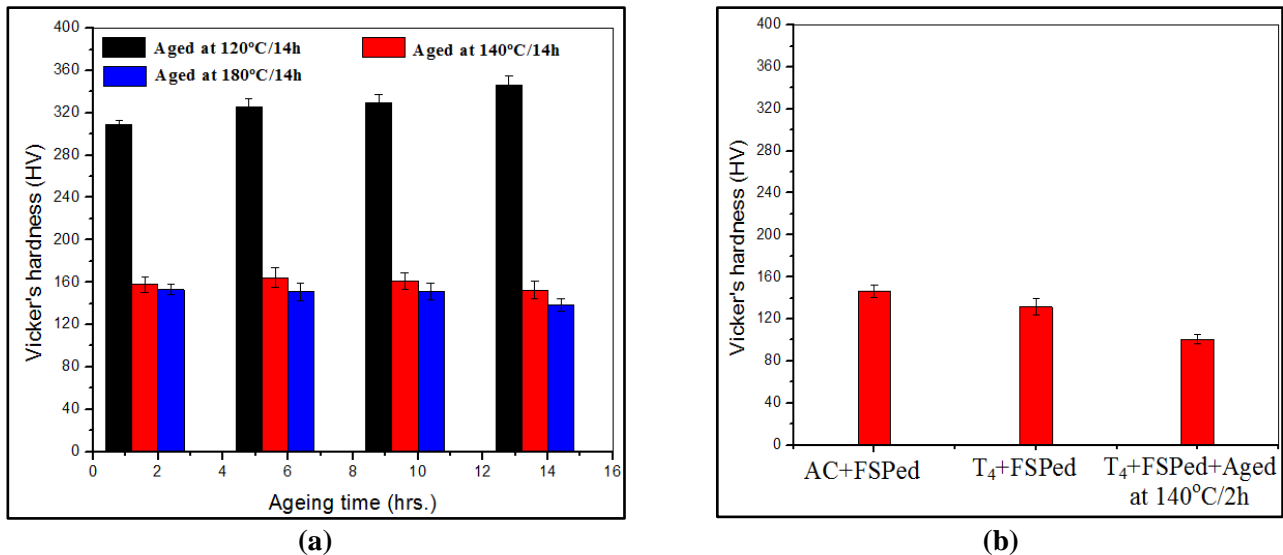


**FIGURE 8: The Vicker's hardness bar diagrams are exhibited hardening effect at different conditions: (a) after different ageing treatments, and (b) after different FSPed conditions. (1000 rpm and 70 mm/min)**

Figure 8(a) shows illustration of Vicker's hardness bar diagrams revealed hardening effect after ageing treatments at 120 to 180°C for 14h of solution treated ( $T_4$ ) aluminium alloy. When aged at 120°C for 14h, the alloy exhibits maximum age-hardening effect nearly two times more than any other ageing treatment conditions throughout the process. Mainly two reasons have to dominate for formation of high volume fraction of GP zones and acceleration of age-hardening effects due to minor Sc addition and their responsibility for early formation of  $\eta$ -phase of 7075 Al alloy. The increase of ageing time beyond the peak ageing time causes the conversion of semi coherent precipitates ( $\eta$ ) to incoherent equilibrium precipitates ( $\eta$ ) and also dissolution of GP zones and coarsening of  $\text{Al}_3\text{Sc}$  type particles. Mostly precipitates are losing the coherency, become coarsen and lightly distributed and they are easily by-passed by dislocation. When aged at 140°C for 14h, the alloy exhibits low age-hardening effect perhaps due to less density of hardening precipitates ( $\eta$ ) and coarsening of  $\text{Al}_3\text{Sc}$  particles. When aged at 180°C for 14h, the alloy exhibits minimum age-hardening effect perhaps due to overaged precipitates ( $\eta$ ) which are incoherent in the matrix, larger interparticle spacing and coarsening of  $\text{Al}_3\text{Sc}$  particles in the grain result in more reduction of strength [33, 34]. The effect of processing parameters on the surface macrohardness (10 kg. load) of Sc added aluminium alloy with FSPed plus different pre-heat treatment and post heat treatment conditions as shown in Figure 8(b). As a result, the hardness was enhanced with uniform distribution of hardening particles of  $\eta$  and  $\text{Al}_3\text{Sc}$  after FSPed in matrix. In some of cases, hardness profile showed a general softening and reduction of hardness due to high heat input for high rotational speed in spite of smaller grain size. The result means that the hardness distribution has not combined with the Hall-Patch relationship. According to the characteristics of the microstructure, the major contributions to hardness of the modified layer exposed by FSPed are fine grains and the Orowan strengthening and dislocation density due to the dispersoid particles. This significant hardness improvement can be attributed by controlling the grain size and heat input through optimum tool rotation and travelling speed. Generally, the enhanced strength found in FSPed aluminium alloy is most likely caused by recrystallized grains, residual stress due to the shoulder compression, precipitation hardening and  $\eta$ ,  $\text{Al}_3\text{Sc}$  additions into the soft matrix, where thermal mismatch occurs between hard particles and soft matrix. Specially, in the case of 3 segment of Figure 8(b) curve's hardness drop sharply perhaps for dissolution of precipitates or coherency loss due to high angle grain boundaries and high heat input (2.15 kJ/mm) after post ageing treatment. Table 2 shows the results of mechanical properties of aluminium alloy after FSPed plus low temperature post ageing treatment led to the increases the proof strength (143.6 MPa) and ultimate tensile strength (256.4 MPa) due to precipitation strengthening, while the simultaneous increase in

ductility (8.6%) and strain hardening exponent (n) of 1.82 obtained from logarithmic true stress-true strain curve indicate high value for good toughness ( $K_{IC} = 32.8 \text{ MPa}\sqrt{\text{m}}$ ) after post ageing treatment is a rare phenomenon [35-37]. These together increases of ductility and strength can be attributed to concurrent incidence of precipitation with internal stress relaxation. In other words, when hardening by ageing dominates over the softening by relaxation of internal stress, an enhancement in both the strength and ductility of the FSPed alloy is possible. Furthermore, as observed from the TEM analysis (Figure 6) shows the new location of secondary phases and dispersoids at the interior grain lead to the less strain and stress localization contributing to an enhancement of ductility. This location of the precipitate due to post ageing treatment at  $140^\circ\text{C}$  for 2h can be explained through two possible theories such as during heat treatment some dislocation walls can disappear, thus leaving many precipitates in the cell interiors. Another, the motion of dislocations existence due to the high gradient of dislocation density from walls to interior of grains and it's displacing the precipitates to interior of grains. As well, heat ratio is 14.29 for given FSP parameters and actual heat input calculated as 2.15 kJ/mm indicates better strength and ductility after low temperature post ageing treatment of aluminum alloy [38-40].

**TABLE 2**  
**RESULTS OF MECHANICAL PROPERTIES HAVE BEEN TABULATED AFTER  $T_4$ +FSPed+AGED AT  $140^\circ\text{C}$  FOR 2h of Al ALLOY.**

7075 Al alloy	Mechanical properties				
	0.2% Proof strength ( $\sigma_{0.2}$ ) in MPa	Ultimate tensile strength ( $\sigma_u$ ) in MPa	%El ( $\delta$ )	Strain hardening exponent (n)	Heat ratio (tool rotation speed/traverse speed)
	143.6	256.4	8.6	1.82	14.29

#### IV. CONCLUSION

In this study, the following conclusions have been summarized below:

- 1) With minor Sc addition peak of ageing effect achieved earlier for high strength Al-Zn-Mg alloy.
- 2) After aged at  $120^\circ\text{C}$  for 14h, the alloy exhibits maximum age-hardening effect due to formation of high volume fraction of GP zones as well as minor Sc addition and their responsibility for early formation of  $\eta$ -phase of 7075 Al alloy.
- 3) FSP is a novel surface modification technique and resulted in substantial grain refinement with numerous commercial applications of 7075 Al alloy. During FSP of aluminium alloy the dispersoids and strengthening particles in the matrix are distributed uniformly throughout the SZ region due to the stirring action of the tool.
- 4) The optical micrograph revealed very fine grains ( $5.31 \pm 1.0 \mu\text{m}$ ) in SZ as well as TMAZ ( $6.96 \pm 2.1 \mu\text{m}$ ) region, but several black spots due to the Zn vaporization and creation of hair line cracks for torsional effects in the TMAZ. Therefore, the SZ comprises very fine grains primarily due to severe plastic deformation (SPD) and dynamic recrystallization mechanism.
- 5) The FESEM micrograph indicated as several white spots which have Sc content of 2.89 wt. % and Si+Fe of 6.89 wt. % in major portion of impurities intend to diminish the strength and ductility of FSPed Al alloy.
- 6) DSC thermogram indicated some distinct exothermic peaks at around  $60^\circ\text{C}$  for formation of GP zones and go on exhibiting anti-recrystallization effects or high thermal stability means thermal strength upto  $600^\circ\text{C}$  then softening tendency come for endothermic reaction due to dissolution of hardening phases and coarsening effects of  $\text{Al}_3\text{Sc}$  particles at around  $636^\circ\text{C}$ .
- 7) The TEM micrographs have been represented as low magnification and for high magnification of studied alloy. The micrograph revealed (500 nm) very fine precipitates (e. g.  $\text{Al}_3\text{Sc}$  and  $\text{MgZn}_2$ ) with dislocation tangles and seems high angle grain boundaries are dominated in matrix. Also, distinct grain boundary has around  $54.32 \pm 16.28 \text{ nm}$  width and PFZ size around  $173.15 \pm 7.36 \text{ nm}$  in the matrix. Other micrograph (200 nm) revealed fine precipitates as well as some coarse particles (agglomeration  $\text{Al}_3\text{Sc}$  particles or T phases) in the matrix.
- 8) The overall strengthening is associated with the fine grain strengthening, sub-grain and precipitation strengthening by  $\text{Al}_3\text{Sc}$  particles and  $\text{MgZn}_2$  precipitates. Moreover, mixture of fine and coarse type coherent spherical  $\text{Al}_3\text{Sc}$  particles appears after  $T_4$ +FSP+Aged at  $140^\circ\text{C}$  for 2h.

### ACKNOWLEDGEMENTS

The authors are express their sincere gratitude for given opportunity of research works at the Department of Metallurgical and Materials Engineering in Indian Institute of Technology Roorkee (IITR), Uttarakhand, India.

### REFERENCES

- [1] Y. Deng, Z. Yin, K. Zhao, J. Duan, Z. He, "Effects of Sc and Zr microalloying additions on the microstructure and mechanical properties of new Al-Zn-Mg alloys", *Journal of Alloys and Compounds*, 530 (2012) 71-80.
- [2] L-M. Wu, M. Seyring, M. Rettenmayr, W-H. Wang, "Characterization of precipitate evolution in an artificially aged Al-Zn-Mg-Sc-Zr alloy", *Materials Science and Engineering A*, 527 (2010) 1068-1073.
- [3] H. Löffler, I. Kovacs, J. Lendvai, "Review Decomposition processes in Al-Zn-Mg alloys", *Journal of Materials Science*, 18 (1983) 2215-2240.
- [4] M-H. Ku, F-Y. Hung, T-S. Lui, L-H. Chen, W-T. Chiang, "Microstructural Effects of Zn/Mg Ratio and Post Heat Treatment on Tensile Properties of Friction Stirred Process (FSP) Al-xZn-yMg Alloys", *Materials Transactions*, Vol. 53, 5(2012) 995-1001.
- [5] Z. Y. Ma, "Friction Stir Processing Technology: A Review", *Metallurgical and Materials Transactions A*, Vol. 39A (March 2008) 642-658.
- [6] K. Li, X. Liu, Y. Zhao, "Research Status and prospect of Friction Stir Processing Technology", *Coatings*, 9, 129 (2019) 1-14.
- [7] A. Goloborodko, T. Ito, X. Yun, Y. Motohashi, G. Itoh, "Friction Stir Welding of a Commercial 7075-T<sub>6</sub> Aluminium Alloy: Grain Refinement, Thermal Stability and Tensile Properties", *Materials Transactions*, Vol. 45, 8(2004) 2503-2508.
- [8] A. Kurt, I. Uygur, E. Cete, "Surface Modification of aluminium by friction stir processing", *Journal of Materials Processing Technology*, 211(2011) 313-317.
- [9] M. M. El Rayes, E. A. El Danaf, M. S. Soliman, "High-temperature deformation and enhanced ductility of friction stir processed-7010 Aluminium Alloy", *Materials and Design*, 32 (2011) 1916-1922.
- [10] R. Kumar, K. Singh, S. Pandey, "Process forces and heat input as function of process parameters in AA5083 friction stir welds", *Transactions of Nonferrous Metals Society of China*, 22(2012) 288-298.
- [11] H. Chen, B. Yang, "Effect of Precipitations on Microstructures and Mechanical Properties of Nanostructured Al-Zn-Mg-Cu Alloy", *Materials Transactions*, Vol. 49, 12(2008) 2912-2915.
- [12] A. D. Isadare, B. Aremo, M. O. Adeoye, O. J. Olawale, M. D. Shittu, "Effect of Heat Treatment on Some Mechanical Properties of 7075 Aluminium Alloy", *Materials Transactions*, 16(1), (2013) 190-194.
- [13] K. Wang, F. C. Liu, Z. Y. Ma, F. C. Zhang, "Realization of exceptionally high elongation at high strain rate in a friction stir processed Al-Zn-Mg-Cu alloy with presence of liquid phase", *Scripta Materialia*, 64(2011) 572-575.
- [14] J. Chen, L. Zhen, S. Yang, W. Shao, S. Dai, "Investigation of precipitation behavior and related hardening in AA 7055 aluminium alloy", *Materials Science and Engineering A*, 500(2009) 34-42.
- [15] G. R. Cui, Z. Y. Ma, S. X. Li, "The origin of non-uniform microstructure and its effects on the mechanical properties of a friction stir processed Al-Mg alloy", *Acta Materialia*, 57(2009) 5718-5729.
- [16] X. Feng, H. Lu, S. S. Babu, "Effect of grain size refinement and precipitation reactions on strengthening in friction stir processed Al-Cu alloys", *Scripta Materialia*, 65(2011) 1057-1060.
- [17] Z. Ahmad, "The Properties and Application of Scandium-Reinforced Aluminium", *Journal of The Minerals, Metals and Materials Society*, Vol. 55, Issue 2, 530(Feb. 2003) 35-39.
- [18] J-Q. Su, T. W. Nelson, C. J. Sterling, "Microstructure evolution during FSW/FSP of high strength aluminium alloys", *Materials Science and Engineering A*, 405(2005) 277-286.
- [19] Y. Deng, R. Ye, G. Xu, J. Yang, Q. Pan, B. Peng, X. Cao, Y. Duan, Y. Wang, L. Lu, Z. Yin, "Corrosion behaviour and mechanism of new aerospace Al-Zn-Mg alloy friction stir welded joints and the effects of secondary Al<sub>3</sub>Sc<sub>x</sub>Zr<sub>1-x</sub> nanoparticles", *Corrosion Science*, 90(2015) 359-374.
- [20] V. J. Arulmoni, R. S. Mishra, "Friction Stir Processing of Aluminium alloys for Defense Applications", *International Journal of Advance Research and Innovation*, Vol. 2, Issue 2 (2014) 337-341.
- [21] M. Shamanian, H. Mostaan, M. Safari, "Friction stir modification of GTA 7075-T<sub>6</sub> Al alloy weld joints: EBSD study and microstructural evolutions", *Archives of Civil and Mechanical Engineering*, 17(2017) 574-585.
- [22] A. Kumar, A. K. Mukhopadhyay, K. S. Prasad, "Superplastic behaviour of Al-Zn-Mg-Cu-Zr alloy AA7010 containing Sc", *Materials Science and Engineering A*, 527(2010) 854-857.
- [23] L-M. Wu, W-H. Wang, Y-F. Hsu, S. Trong, "Effects of homogenization treatment on recrystallization behaviour and dispersoid distribution in an Al-Zn-Mg-Sc-Zr alloy", *Journal of Alloys and Compounds*, 456(2008) 163-169.
- [24] T. Hu, K. Ma, T. D. Topping, J. M. Schoenung, E. J. Lavernia, "Precipitation phenomena in an ultrafine-grained Al alloy", *Acta Materialia*, 61(2013) 2163-2178.
- [25] N. Afify, A-F. Gaber, G. Abbady, "Fine Scale Precipitates in Al-Zn-Mg Alloys after Various Aging Temperatures", *Materials Sciences and Applications*, 2(2011) 427-434.
- [26] O. N. Senkov, S. V. Senkova, M. R. Shagiev, "Effect of Sc on Aging Kinetics in a Direct Chill Cast Al-Zn-Mg-Cu Alloy", *Metallurgical and Materials Transactions A*, Vol. 39A (May 2008) 1034-1053.
- [27] S. Gholami, E. Emadoddin, M. Tajally, E. Borhani, "Friction stir processing of 7075 Al alloy and subsequent aging treatment", *Transactions of Nonferrous Metals Society of China*, 25(2015) 2847-2855.

- [28] N. Kumar, R. S. Mishra, Ultrafine-Grained Al-Mg-Sc Alloy via Friction-Stir Processing, *Metallurgical and Materials Transactions A*, Vol. 44A, (Feb. 2013)934-945.
- [29] P. K. Mandal, J. Felix Kumar, "Investigation of precipitation Behaviour and Related Microstructural and Mechanical properties after FSP of Aluminium Alloy", *International Advanced Journal of Engineering Research*, Vol. 2, Issue 11 (November 2019) 15-19.
- [30] Z. Chen, Y. Mo, Z. Nie, "Effect of Zn Content on the Microstructure and Properties of Super-High Strength Al-Zn-Mg-Cu Alloys", *Metallurgical and Materials Transactions A*, Vol. 44A, (Aug. 2013) 3910-3920.
- [31] J. Ma, D. Yan, L. Rong, Y. Li, "Effect of Sc addition on microstructure and mechanical properties of 1460 alloy", *Progress in Natural Science: Materials International*, 24(2014) 13-18.
- [32] X. Ju, F. Zhang, Z. Chen, G. Ji, M. Wang, Y. Wu, S. Zhong, H. Wang, "Microstructure of Multi-Pass Friction-Stir-Processed Al-Zn-Mg-Cu Alloys Reinforced by Nano-Sized TiB<sub>2</sub> Particles and the Effect of T<sub>6</sub> Heat Treatment", *Metals*, 7, 530(2017) 1-15.
- [33] S. Hirose, T. Hamaoka, Z. Horita, S. Lee, K. Matsuda, D. Terada, "Methods for Designing Concurrently Strengthened Severely Deformed Age-Hardenable Aluminium Alloys by Ultrafine-Grained and Precipitation Hardenings", *Metallurgical and Materials Transactions A*, Vol. 44A, (Aug. 2013) 3921-3933.
- [34] M. R. Clinch, S. J. Harris, W. Hepples, N. J. H. Holroyd, M. J. Lawday, B. Noble, "Influence of Zinc to Magnesium Ratio and Total Solute Content on the Strength and Toughness of 7xxx series Alloys", *Materials Science Forum*, Vols. 519-521(2006) 339-344.
- [35] H. Zhenbo, Y. Zhimin, L. Sen, D. Ying, S. Baochuan, Z. Xiang, "Preparation, microstructure and properties of Al-Zn-Mg-Sc alloy tubes", *Journal of Rare Earths*, Vol. 28, No. 4, (August 2010) 641-646.
- [36] M. Vratnica, Z. Cvijovic, N. Radovic, "THE EFFECT OF COMPOSITIONAL VARIATIONS ON THE FRACTURE TOUGHNESS OF 7000 Al-ALLOYS", *Materials and Technology*, 42, 5(2008) 191-196.
- [37] A. C. Reddy, S. S. Rajan, "Influence of ageing, inclusions and voids on ductility fracture mechanism in commercial Al-alloys", *Bulletin of Material Science*, Vol. 28, No. 1, (February 2005) 75-79.
- [38] S. Dadbakhsh, A. K. Taheri, C. W. Smith, "Strengthening study on 6082 Al alloy combination of aging treatment and ECAP process", *Materials Science and Engineering A*, 527(2010) 4758-4766.
- [39] P. K. Mandal, "Study on hardening mechanisms in aluminium alloys", *International Journal of Engineering Research and Applications*, Vol. 4, Issue 1, Part-6 (January 2016)91-97.
- [40] G. M. Ludtka, D. E. Laughlin, "The Influence of Microstructure and Strength on the Fracture Mode and Toughness of 7XXX Series Aluminium Alloys", *Metallurgical Transactions A*, Vol. 13A (March 1982) 411-425.

# Naphthol Oligomers and their Electroconductive Compositions

R.R. Guliyev<sup>1</sup>, D.N. Aliyeva<sup>2</sup>, R.A. Akhmedova<sup>3</sup>, S.S. Mashayeva<sup>4</sup>, Ch.O. Ismailova<sup>5</sup>,  
B.A. Mamedov<sup>6</sup>

Institute of Polymer Materials of Azerbaijan National Academy of Sciences, Sumgait

**Abstract**— By oxidative polycondensation reaction of 1- and 2-naphthols, the polyfunctional polyconjugated soluble and melttable oligomers showing the thermostable, semiconductive and paramagnetic properties, as well as high reactivity in the reactions characteristic for aromatic hydroxyl groups have been obtained.

They have been used as active fillers in preparation of electroconductive compositions on the basis of thermoplasts and rubbers. The antistatic polymer-oligomer compositions of LDPE, PP and PS with naphthol oligomers have been obtained. It has been shown that in partial substitution of carbon black by naphthol oligomers in the composition of vulcanizate from BR, the obtained rubbers exhibit high heat-physical, physical-mechanical and electrical properties.

**Keywords**— electroactive polymers, electroconductive compositions, naphthol, oligonaphthol, oxidation, polycondensation.

## I. INTRODUCTION

It was known that the various types of electroactive thermoplastic polymer materials and rubbers are successfully used in the various fields of technique and industry, where it is necessary to remove electrostatic charges arising from friction and deformation of products [1]. Usually these materials are obtained by introduction of electroconductive fillers into the corresponding polymers, since thermoplastics, thermoplastics and rubbers are good electrical isolators. As such fillers, the metal powders, various brands of carbon black and powdered graphite are often used [2, 3]. Under certain conditions, the particles of such fillers form continuous electroconductive structures – in most cases, three-dimensional nets. However, the polymer composition materials developed with use of metal powders do not have the necessary elastic properties and the initial polymers are incompatible with metal particles, which, of course, lead to rapid destruction of current-conductive structures as a result of deformation of products during exploitation. An application of electroconductive additives of the organic nature (for ex., various types of structuring carbon blacks) allow to obtain the electroconductive composition materials with good physical-mechanical properties due to good compatibility of components [4-7].

It should be also noted that the polyfunctional aromatic polyconjugated oligomers possess thermo- and radiation stability, paramagnetism, semiconductivity, stabilizing and antistatic activity. In addition, they show solubility, meltability and high reactivity in various chemical conversions [5-10].

Taking this into account, we have synthesized the oligo(1-naphthol) and oligo(2-naphthol), including reactive hydroxyl groups, oxidative polycondensation of naphthols in the presence of hydrogen peroxide, and by oxidation of these oligomers with molecular oxygen in an alkaline medium there have been obtained the macroradicals of naphthoxyl type with various concentration of paramagnetic centers (PMC).

## II. EXPERIMENTAL

The synthesis of naphthol oligomers (NO) was carried out in a 500 ml three-necked flask equipped with thermometer, a mechanical stirrer and reflux condenser. 28.8 g (0.1 mol) of naphthol, 170 g of 30% solution of hydrogen peroxide (0.6 mol H<sub>2</sub>O<sub>2</sub>) and 140 ml of distilled water were placed in the flask. The oxidative polycondensation reaction was carried out at 363 K for 4 h in intensive mixing of the reaction. The synthesized samples of NO were purified from residue of monomer with washing of hot distilled water and dried at 373 K in vacuum box (13.3 Pa) to constant mass.

The oxidation of the synthesized naphthol oligomers was carried out in a glass reactor equipped with magnetic stirrer, a thermometer and a bubbler. 21.3 g (0.15 mol) of NO, 110 ml of C<sub>2</sub>H<sub>5</sub>OH were loaded into a reactor and after achievement of the preset temperature the dry and purified oxygen was passed through the system with rate 5.6 l/h. After reaction completion the reaction system was subjected to the filtration, the obtained precipitate was washed with ethanol and dried in vacuum (13.3 Pa) at 313-323 K to constant mass. The kinetics of the oxidative polycondensation and NO oxidation was studied by volumetric method by measurement of volume, absorbed by reaction mixture of the oxygen at its constant pressure equal to 98.066 kPa according to the method described in [9-10].

The IR spectra of NO were taken for thin films of naphthol oligomers applied on NaCl monocrystals (for those NO samples,

which did not form the high-quality films, tablets were obtained from fine-grained mixture of an oligomer and KBr by pressing under pressure) on spectrometer "Agilent Cary 630 FTIR", of firm "Agilent Technologies". The UV spectra of NO samples were taken in ethanol by means of spectrometer "Agilent Cary 60 spectrophotometer" of firm "Agilent Technologies". EPR spectra of NO samples were taken on spectrometer PE-1806. DPhPH and 2,2,6,6-tetramethyl-4-oxypiperidine-1-oxyl were used as standards [9].

The molecular weights (MW) and molecular-weight distribution (MWD) of oligomers were determined on gel-chromatograph "Waters" (refractometric detector) [10]. Three styrogel columns with porosity of 200, 500 and 1000 Å were used. Eluent – tetrahydrofuran. Eluent feeding rate – 1.0-1.1 ml/min. The sample was introduced for one min. as 0.2% NO solution in tetrahydrofuran. For calculation, it was used a calibration dependence, which is described by the equation  $V_R = 30.8 - 4.0 \cdot \lg M$ , where  $V_R$  is the retention volume, ml;  $M$  is the molecular weight. The average molecular weights were calculated on formulas

$$\bar{M}_w = \sum W_i M_i \quad \text{and} \quad \bar{M}_n = \frac{1}{\sum W_i / M_i},$$

where:  $W_i$  – mass fraction with molecular weight  $M_i$  (it was defined as a ratio of the area of  $i$ -th part of chromatogram to all area).

The electrical measurements have been carried out according to the standard method on direct current by means of an amplifier B 3-16, and on alternating current by means of a bridge R-571 – in low frequencies and Q-meter – in the field of high frequency ( $5 \cdot 10^4 - 3 \cdot 10^7$  Hz).

A rubber mixture on the basis on butyl rubber (BR) and the synthesized oligomer compound were made by means of laboratory rollers. On the rollers, the rubber was firstly plasticized, and then the necessary components were added in a certain sequence, including an oligomer compound and mixed. Depending on peculiarities of the mixture components, the temperature of the rolls was adjusted in the front shaft in the range of 303-313 K, in the ending shaft in the range of 343-348 K.

Following the sequence of introduction of components, the preparation of the rubber mixture was carried out as follows: 1) BR – 0; techn.stearin. – 3 min; captax – 5 min, thiuram – 7 min, zinc oxide + oligomer – 10 min; sulphur – 15 min, total time of mixing – 20 min, vulcanization temperature – 313-323 K, 2) Further, by means of PG-63 hydraulic press, the obtained mixtures were pressed in special press-molds in the form of plates with thickness of 1.5-2.0 mm. With use of standard knives, the samples of various shapes and sizes were cut from obtained plates for determination of the physical-mechanical (tensile strength, specific elongation, residual deformation), electrical and other properties.

The strength and deformation properties of the samples were determined by means of breaking machine PM-250.

The electrical resistance of the sample area (R) in OM was calculated on formula:

$$R = \frac{V}{I}$$

Where:  $V$  – tension value in the sample area between tension electrodes, measured by electrometer (B),  $I$  – Current, passing through sample (A).

From all R measurements on one sample the average arithmetic value of the sample resistance was calculated ( $R_{av}$ ).

The specific volumetric electrical resistance –  $\rho_v$  (Om·cm) was calculated on formula:

$$\rho_v = \frac{R_{cp} \cdot h \cdot b}{l}$$

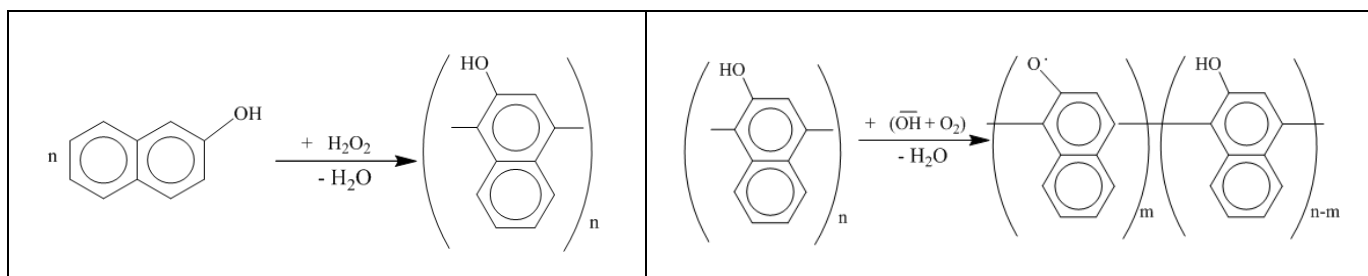
Where:  $R_{av}$  – average arithmetic value of electrical resistance of the sample (Om),  $h$  – sample thickness (cm),  $b$  – sample width (cm) and  $l$  – distance between tension electrodes (cm).

The specific volumetric electroconductivity ( $\sigma_v$ ),  $\text{Om}^{-1} \cdot \text{cm}^{-1}$ , was calculated on formula:

$$\sigma_v = \frac{1}{\rho_v}$$

### III. RESULTS AND DISCUSSION

The synthesis of naphthol oligomers (NO) was carried out by oxidative polycondensation reaction of naphthols in the presence of hydrogen peroxide and the macronaphthoxyl radicals with various concentration of paramagnetic centers (PMC) by NO oxidation with oxygen in alcohol-alkaline medium:



The synthesized NO samples are the powders of dark brown or black color, well soluble in polar organic solvents and melting under load at 380-405 K, depending on synthesis conditions. Their composition and structure has been established by methods of elemental, chemical and IR spectral analyses, and the molecular-weight indices – by a method of gel-permeating chromatography (Table 1).

**TABLE 1**  
**SYNTHESIS CONDITIONS AND SOME INDICES OF OLIGOHYDROXYNAPHTHYLENES (T = 4 H)**

Naphthol, mol/l	$\text{H}_2\text{O}_2$ , mol/l	T, K	Yield, %	Elemental composition, %		OH groups, %	MW indices		
				C	H		$\overline{M}_w$	$\overline{M}_n$	$\overline{M}_w/\overline{M}_n$
1.2	1.2	343	29.1	84.16	4.85	10.1	850	730	1.16
1.2	1.2	353	34.5	84.23	4.83	10.3	890	750	1.19
1.2	1.2	363	45.6	83.72	4.72	11.1	960	790	1.22
1.2	1.2	368	51.7	83.84	4.51	11.5	1230	870	1.41
1.6	1.6	368	52.4	84.22	4.59	11.8	1270	960	1.32
1.2	2.4	368	73.5	83.78	4.43	10.6	1370	1030	1.33
1.2	3.6	368	86.9	84.37	4.69	11.9	1560	1180	1.32

The results of elemental analysis and determination of content of hydroxyl groups evidence that they are practically identical for synthesized oligomers and 1-naphthol. This indicates that at naphthol oligomerization the dehydration reaction does not occur and the simple ether bonds are not formed. Indeed, in the IR spectra of oligomers the absorption band of C–O–C groups at  $1230\text{ cm}^{-1}$  are not observed. At the same time, in the spectra at  $3400\text{--}3580\text{ cm}^{-1}$  the wide intensive absorption band characteristic for associated hydroxyl groups is fixed. In addition, in the IR spectra the absorption bands of naphthalene ring ( $1455$ ,  $1520$  and  $1600\text{ cm}^{-1}$ ) and nonplanar deformation vibrations of aromatic –CH groups at  $770\text{ cm}^{-1}$  (for four neighboring CH-groups) and  $875\text{--}880\text{ cm}^{-1}$  (for isolated –CH groups) are appeared.

In the UV spectra of the synthesized NO samples, a wide intense peak with maximum at 220 nm, and also less intense absorption bands with maxima at 285 and 330 nm have been fixed. The first of these is E-band ( $\pi \rightarrow \pi^*$  excitation, and the second characterizes  $n \rightarrow \pi^*$  transitions of the non-divided electrons of the oxygen atom. The last peak indicates the availability of a system of polyconjugated bonds).

The obtained NO samples possess electron-exchange activity, their aqueous and alcohol solutions absorb intensively molecular oxygen (Fig.1). NO oxidation rate constant values are sufficiently high ( $k = 3.8 \cdot 10^{-2} - 24.1 \cdot 10^{-2}\text{ min}^{-1}$  at 313-333 K, solvent – methanol), and activation energy value is equal to 84.6 kJ/mol. By NO oxidation one can obtain the stable macroradicals of naphthoxyl type, i.e. the obtained and oxidized NO samples show the paramagnetic (PMC concentration  $\sim 1.3 \cdot 10^{17} - 2.75 \cdot 10^{19}\text{ spin/g}$ ) and semiconducting ( $\sigma_0 \sim 10^{-14} - 10^{-9}\text{ Ohm}^{-1} \cdot \text{cm}^{-1}$  at 298 K,  $E = 1.3 - 1.67\text{ eV}$ ) properties. Moreover, an increase of PMC concentration in the composition of NO samples by 1-2 orders of magnitude leads to a noticeable increase of their electroconductivity (Table 2 and 3). Consequently, these oligomers can fulfill the function of an antioxidant in the composition and thus increase the heat- and thermal stability, as well as a period of their effective exploitation.

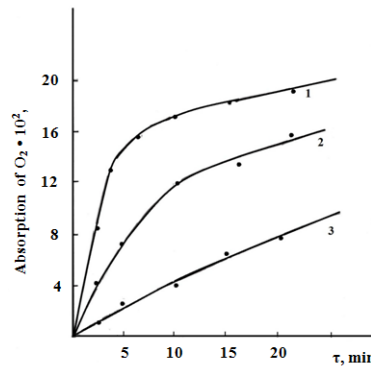


FIGURE 1: Kinetic curves of oxygen absorption by alkaline solution of NO in methanol.  $[\text{NO}]_0 = 0.34 \text{ mol/l}$ ,  $[\text{NaOH}]_0 = 0.45 \text{ mol/l}$ . T, K: 333 (1), 323 (2) and 313 (3).

TABLE 2  
PREPARATION OF NO SAMPLES WITH VARIOUS PMC CONCENTRATION

N <sub>2</sub>	$[\text{OH}^-]_0, \text{ mol/l}$	$[\text{NO}]_0^*, \text{ mol/l}$	T, K	$\tau, \text{ min.}$	$[\text{PMC}] \cdot 10^{-19}, \text{ spin/g}$
1	1.5	2.0	308	20	1.30
2	1.5	1.5	308	20	1.47
3	1.5	0.75	308	20	0.75
4	0.35	0.75	308	20	0.87
5	0.72	0.75	308	20	0.95
6	0.72	0.75	308	20	0.79
7	0.72	0.75	303	20	1.18
8	0.72	0.75	313	20	1.72
9	1.5	1.5	308	40	2.25
10	1.5	1.5	308	45	2.75

\*PMC concentration for initial NO sample was  $-0.54 \cdot 10^{18} \text{ spin/g}$ .

TABLE 3  
SOME ELECTRICAL INDICES OF NO SAMPLES CONTAINING VARIOUS PMC CONCENTRATION

$[\text{PMC}] \cdot 10^{-18}, \text{ cm}^{-3}$	$\sigma(0), \text{ Om}^{-1} \cdot \text{cm}^{-1}$	$\sigma(\omega) \text{ at } 10^6 \text{ Hz}, \text{ Om}^{-1} \cdot \text{cm}^{-1}$	$N(E_F) \cdot 10^{20}, \text{ cm}^{-3} \cdot \text{eV}^{-1}$	$N_0(E_F) \cdot 10^{-18}, \text{ cm}^{-3}$
1.3	$1.25 \cdot 10^{-14}$	$1.1 \cdot 10^{-9}$	0.48	1.20
7.5	$1.72 \cdot 10^{-10}$	$2.3 \cdot 10^{-8}$	2.90	7.25
11.8	$5.9 \cdot 10^{-10}$	$6.3 \cdot 10^{-8}$	4.72	11.9
22.5	$1.2 \cdot 10^{-9}$	$2.5 \cdot 10^{-7}$	7.62	19.1

The possibility of increase of the electroconductivity of NO with growth of PMC concentration in its composition has been used for creation of antistatic polymer compositions on the basis of thermoplastics by introduction of 5÷15% of NO into their composition, followed by treatment of the material surface with an aqueous or alcohol solution of alkali. It can be seen from Table 4 that  $\rho_v$  after introduction of NO into composition of thermoplasts is essentially decreased.

TABLE 4  
 $\rho_v$  VALUES OF COMPOSITION MATERIALS ON THE BASIS OF THERMOPLASTS AND NO

NO, %	Thermoplast, %	$\rho_v (\text{Om} \cdot \text{cm}), \text{ on the basis}$		
		LDPE	PP	PS
5	95	$0.81 \cdot 10^8$ ( $7.3 \cdot 10^8$ )	$2.5 \cdot 10^8$ ( $9.1 \cdot 10^8$ )	$4.8 \cdot 10^8$ ( $9.8 \cdot 10^8$ )
10	90	$3.5 \cdot 10^8$ ( $6.4 \cdot 10^8$ )	$8.1 \cdot 10^8$ ( $1.2 \cdot 10^7$ )	$9.5 \cdot 10^8$ ( $2.7 \cdot 10^7$ )
15	85	$8.6 \cdot 10^8$ ( $3.7 \cdot 10^7$ )	$9.8 \cdot 10^8$ ( $6.0 \cdot 10^7$ )	$2.8 \cdot 10^8$ ( $8.5 \cdot 10^7$ )

The synthesized NO samples have been used as active additive for preparation of the rubber mixtures on the basis of rubbers, for ex., butyl rubber (BR). In this case, the rubber mixtures on the basis of BR have been made according to the standard recipe of ingredients with only difference that NO samples have been (partially) used instead of carbon black (from 20.0 to 45 w.p. per 100 w.p. of rubber) (Table 5).

**TABLE 5**  
**COMPOSITIONS OF THE RUBBER MIXTURES AND PHYSICAL-MECHANICAL AND ELECTRICAL INDICES OF THE OBTAINED VULCANIZATES ON THE BASIS OF BUTYL RUBBER**

№	Ingredients			Mixtures (mass, g)			
				1	2	3	4
1	Butyl rubber			100	100	100	100
2	Technical stearin			3.0	3.0	3.0	3.0
3	Captax			0.65	0.65	0.65	0.65
4	DPHG			1.3	1.3	1.3	1.3
5	Zinc oxide			5.0	5.0	5.0	5.0
6	Black carbon			50	30	15	5
7	NO			0	20	35	45
8	Sulphur			2.0	2.0	2.0	2.0
Properties							
Mixtures	Vulcanization time, min.	Tensile strength, MPa	Specific elongation, %	Residual deformation, %	Modulus of elongation, MPa		$\sigma \cdot 10^7, \text{Om}^{-1} \cdot \text{cm}^{-1}$
					200%	300%	
1	2	3	4	5	6	7	8
Before aging							
1	40	19.5	710.0	4.2	9.4	14.1	
	60	18.3	700.0	4.5	9.0	13.2	
	80	19.1	663.3	4.3	9.8	14.3	
2	40	21.5	690.0	8.0	8.4	12.1	0.07
	60	23.6	681.5	7.3	8.1	12.5	0.25
	80	24.1	611.4	6.9	8.8	13.0	0.22
3	40	20.9	704.2	10.3	6.5	10.6	3.4
	60	21.6	672.0	12.1	7.0	11.1	5.6
	80	22.6	602.0	13.4	7.3	12.0	4.4
4	40	24.1	695.4	12.0	6.3	9.0	18
	60	26.0	674.0	13.5	6.5	10.1	24
	80	28.5	600.0	15.1	7.1	10.7	32
1	2	3	4	5	6	7	8
After exposure at 373 K for 24 h							
1	40	15.1	382	2.8	7.0	17.6	
	60	15.8	417	1.8	5.2	14.9	
	80	16.3	424	1.3	4.8	17.2	
2	40	20.8	580.7	4.1	7.0	12.8	0.05
	60	22.1	520.2	3.4	6.6	12.2	0.15
	80	22.5	508.4	3.1	7.0	12.9	0.26
3	40	20.3	583.1	4.8	5.1	9.5	4.1
	60	21.2	524.2	6.0	5.5	9.8	5.8
	80	23.5	485.2	7.1	6.4	10.2	6.7
4	40	23.2	575.5	5.7	4.8	8.4	64
	60	24.7	532.4	6.7	5.5	8.9	67
	80	25.8	491.3	7.9	5.9	8.7	73

It has been established that an introduction of NO instead of carbon black into composition of the rubber mixtures leads to an increase of tensile strength, specific elongation and decrease of modulus of elasticity of the obtained rubbers.

For example, a tensile strength for rubbers obtained with mixture vulcanization on the basis of BR including 20 mass p. of NO instead of carbon black is increased to 21.5÷24.1 MPa, a specific elongation reaches 611÷690%, and a modulus in elongation is decreased by 200% from 9.4÷9.8 to 8.1÷8.8 MPa. Along with this, the thermal stability and service life of the obtained rubbers are increased, which is obviously has been connected with structural peculiarity of NO; condensed aromatic structural fragments in the chain of aromatic polyconjugation stipulate high thermal stability, and an availability of hydroxyl groups in naphthalene rings – antioxidant activity. Since NO samples with different contents of PMC exhibit the high electrical conductivity, their joint use with electroconductive carbon black allows to obtain a rubber with a specific volume conductivity  $10^{-8} \div 10^{-6} \text{Om}^{-1} \cdot \text{cm}^{-1}$ . Moreover, a growth of NO content from 20 to 45.0 w.p. (from rubber mass) instead of carbon black and also an increase of PMC concentration in NO composition leads to an increase of specific electroconductivity of the obtained rubbers. An effect of percolation is reached at content ~22.8 mass p. of NO for rubbers obtained from BR (Fig. 2).

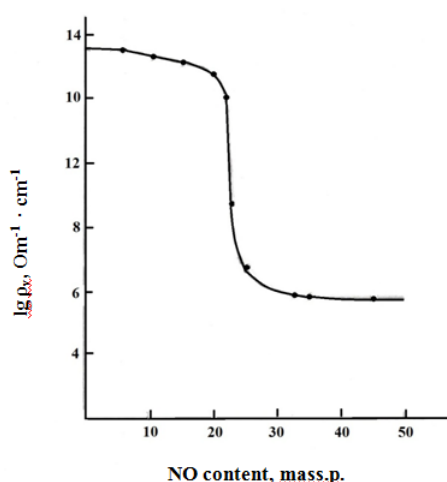


**FIGURE 2. Change of specific volume resistance of vulcanizates from content of NO : BR.**

The reinforcing properties of NO in the rubber composition have been probably stipulated by optimal combination of such indices as small particle size, low density, good compatibility of components and the participation of hydroxyl groups in the formation of the spatial net. Indeed, the specific volume resistance of the obtained rubbers depends on mixing time at various NO contents. The main reasons of change of specific resistance value of the made rubbers are the structurization or destruction of macromolecules. As a result of vulcanization, it is formed a net and a higher internal tension arises in the rubber. With increase of the rolling duration a probability of mechanical destruction of spatially cross-linked macromolecules is increased, a consequence of which is the formation of defective zones in the vulcanizate matrix (Table 6).

**TABLE 6.**  
**P<sub>V</sub> VALUES OF VULCANIZATES OBTAINED AT VARIOUS MIXING TIME AND NO CONTENT**  
**(VULCANIZATIUN TIME – 40 MIN.)**

N	NO content per 100 w.p. BR, w.p.	Mixing time, min.		$\sigma \cdot 10^7$ , $\text{Om}^{-1} \cdot \text{cm}^{-1}$
		Total	with NO	
1	20.5	41	2	0.28
2	20.5	44	5	1.12
3	20.5	46.5	7.5	3.8
4	35.0	41	2	4.9
5	35.0	44	5	8.3
6	35.0	46.5	7.5	9.8
7	45.0	41	2	65
8	45.0	44	5	82
9	45.0	46.5	7.5	96

Thus, the accumulation of static electric charges on the surface of rubber-technical products during their exploitation with

use of the developed rubbers is minimized.

#### IV. CONCLUSIONS

1. By oxidative polycondensation reaction of 1- and 2-naphthols, the polyfunctional polyconjugated soluble and meltable oligomers, including the corresponding hydroxynaphthylene links with high reactivity in the reactions characteristic for aromatic hydroxyl groups have been obtained.
2. By oxidation of naphthol oligomers one can obtain the stable macroradicals of naphthoxyl type. The obtained and oxidized NO samples show the paramagnetic (PMC concentration  $\sim 1.3 \cdot 10^{17} \div 2.75 \cdot 10^{19}$  spin/g) and semiconducting ( $\sigma_0 \sim 10^{-14} \div 10^{-9} \text{ Om}^{-1} \cdot \text{cm}^{-1}$  at 298 K,  $E = 1.3 \div 1.67 \text{ eV}$ ) properties.
3. The naphthol oligomers have been used as active fillers in preparation of electroconductive compositions on the basis of thermoplasts and rubbers. The antistatic polymer-oligomer compositions of LDPE, PP and PS with naphthol oligomers have been obtained.
4. It has been shown that in partial substitution of carbon black by naphthol oligomers on the composition of vulcanizates from BR, the obtained rubbers show the high heat-physical, physical-mechanical and electrical properties.

#### REFERENCES

- [1]. Herbert Naarmann, Polymers, Electrically Conducting, Ullmann's Encyclopedia of Industrial Chemistry 2002, 429 p.
- [2]. V. S. Kaverinskiy, and F. M. Smekhov, Electrical properties of paint and varnish materials and coatings. Moscow: Khimiya, 1990, 158 p.
- [3]. A. Ya. Valipour, P. N. Moghaddam, and B. A. Mamedov, "Some Aspects of Chemical Procedures & Application Trends of Polyaniline as An Intrinsically Conductive Polymer," Life Sci. J., 2012, v. 9, N 4, pp. 409-421.
- [4]. A. Ya. Valipour, P. N. Moghaddam, and B. A. Mamedov, "Synthesis of Hydrophilic Template As A Matrix Polymer For Preparation of Soluble Conductive Polyaniline Composites," Archives de Science Journal. Switzerland, Geneva, 2012, v. 65, N 7, pp. 14-20.
- [5]. A. Pud, N. Ogurtsov, A. Korzhenko, and Q. Shapoval, "Some Aspects of Preparation Methods and Properties of Polyaniline Blends and Composites with Organic Polymers," Prog. Polym. Sci., 2003, v. 28, pp. 1701-1753.
- [6]. A. V. Ragimov, B. A. Mamedov, and S. G. Gasanova, "New Efficient Dielectric and Antistatic Materials Based on Oligoaminophenols," Polymer International, 1997, v. 43, N 4, p. 343-348.
- [7]. B. A. Mammadov, R. A. Ahmadova, Mashayeva S.S. et al. "Preparation of Oligo-4-Aminophenol And Electroconductive Composition Materials On Its Basis," European Applied Sciences, 2014, N 1, pp. 147-153.
- [8]. M. Tefera, A. Geto, M. Tessema, S. Admassie, et al., "Simultaneous Determination of Caffeine and Paracetamol by Square Wave Voltammetry at Poly(4-Amino-3-Hydroxynaphthalene Sulfonic Acid)-Modified Glassy Carbon Electrode," Food Chemistry, 2016, v. 210, pp. 156-162.
- [9]. H. Bhandari, R. Srivastav, V. Choudhary, and S. K. Dhawan, "Enhancement of Corrosion Protection Efficiency of Iron by Poly(Aniline-Co-Amino-Naphthol-Sulphonic Acid) Nanowires Coating In Highly Acidic Medium," Thin Solid Films, 2010, v. 519(3), pp.1031-1039.
- [10]. F. Doğan, K. Şirin, F. Kolcu, and İ. Kaya, "Conducting Polymer Composites Based On LDPE Doped With Poly(Aminonaphthol Sulfonic Acid)," Journal of Electrostatics, 2018, v. 94, pp. 85-93.

# Alzheimer's Detection By Using Neural Networks

Kavita Patil<sup>1</sup>, Geetanjali Kale<sup>2</sup>

<sup>1</sup>Department of EXTC, MUMBAI University

<sup>2</sup>Department of ETRX, MUMBAI University

**Abstract**— It is very important to get the diagnosis tools in early stage of Alzheimer as it will increase patient's chances of recovering and it enables the people attending the patient to take better care of him/her. Alzheimer's disease (shortly AD) is an acute disease with many number of the human deaths mostly people over 60 years. There are number of techniques like blood test, psychological analysis and neuroimaging, are available for the detection of Alzheimer's disease. Here we present details of work done in detection and classification of the Alzheimer's disease using neuroimaging techniques. MRI (magnetic resonance imaging) scans of brains are used for detection and classification purpose. First stage is to preprocess the MRI images and then we segment it. Next we do feature extraction from segmented image. These features are stored for the last stage which is classification and detection. Classification and detection is done using artificial neural network (ANN) which is very reliable and accurate technique. Neural network is trained using number of sample data and extracted feature. This leads to more accurate results which will aid in early diagnosis of Alzheimer's disease.

**Keywords**— Alzheimer's disease, artificial neural network, classification, magnetic resonance imaging, neuroimaging, positron emission tomography.

## I. INTRODUCTION

Alzheimer's disease is disorder in which person slowly starts to lose his/her memory, thinking ability and finally he/she is unable to do the simplistic day to day task. It is irreversible damage to the brain. It affects mostly the older people but can rarely be seen in people between 30 to 60 years. It was discovered by Dr. Alois Alzheimer in 1906. While examining he started noticing abnormalities in brain tissues of a dead woman. These abnormalities are now known as main features of the disease. The other significant finding was damage to interconnect between nerve cells. By studying these abnormalities we can detect the onset of the disease. The people affected by the disease can look normal in day to day life but steadily start having difficulties in day to day activities like reading, recognizing object, reasoning, driving and others. Eventually the brain damage is so much that its tissue shrunk. The disease is fatal and causes number of deaths every year. It is really necessary to diagnose the disease in early stages to take better care of the patient. Mild cognitive impairment (MCI) can be considered as the early stage of the Alzheimer. But not every person with MCI develops Alzheimer. Thus proper classification of the brain scans is necessary to segregate the affected person from non-affected one. There is pattern in brain damage as disease progresses. Hippocampus is one of the regions in the brain which first gets affected. This region is responsible for episodic and spatial memory and also provides interconnects between brain and body. Present day medicines only help to keep the symptoms in check. But they are not able to stop the progression of the disease. The disease is not curable and there is no treatment in current time to reverse the damage done to the brain. Computer based system for Alzheimer's disease focused on taking number of data samples and splitting them in training and testing samples. It uses morphological operations to separate normal brain scans from disease affected brain scans. Morphometry analysis is also used to study brain MRI images to classify them in normal or abnormal categories. It helps in computation of the structural differences throughout the brain tissues. Another form of Morphometry is voxel based Morphometry which allows to compare differences in local concentration of brain tissues using voxel wise comparison of multiple brain images. Study has been conducted to measure volumetric atrophy of the gray matter in the areas of the neocortex of the Alzheimer's patients and non-affected patients. In this method subject images are spatially normalized and then tissue classes are segmented using priori probability maps. Next step is to use denoising and remove distortions. The data is then tested using general linear model for residual variability and experimental results. This results in statistical parametric map which are thresholded for required result. There are also experiments using machine learning techniques for classifying brain images into normal or specific neurodegenerative disease. In these experiments various forms of artificial neural network are used for classification. Some studies also show use of support vector machine with linear as well as non-linear kernels. Feature extraction can be done in different ways like using morphological operation, based on region of interest, or using grey level co-occurrence matrix on segmented image. Computer techniques are widely used in medical diagnosis mostly in cancer related cases. The research is done in detecting brain, liver and breast cancer detection using various image processing techniques using human organ photos or images. MRI scans are commonly used in neuroscience to study the brain tissues and any damage to them. These MRI images can be

processed to highlight the damages done to the brain tissues which can be used to detect the disease. A combination of the image processing techniques like denoising, segmentation, feature extraction and classification technique are applied to obtain affected region in the MRI image of the brain.

## II. METHODOLOGY

### 2.1 Reading MRI Images

First step is to read dataset of MRI images. We are also using positron emission topography (PET) images.

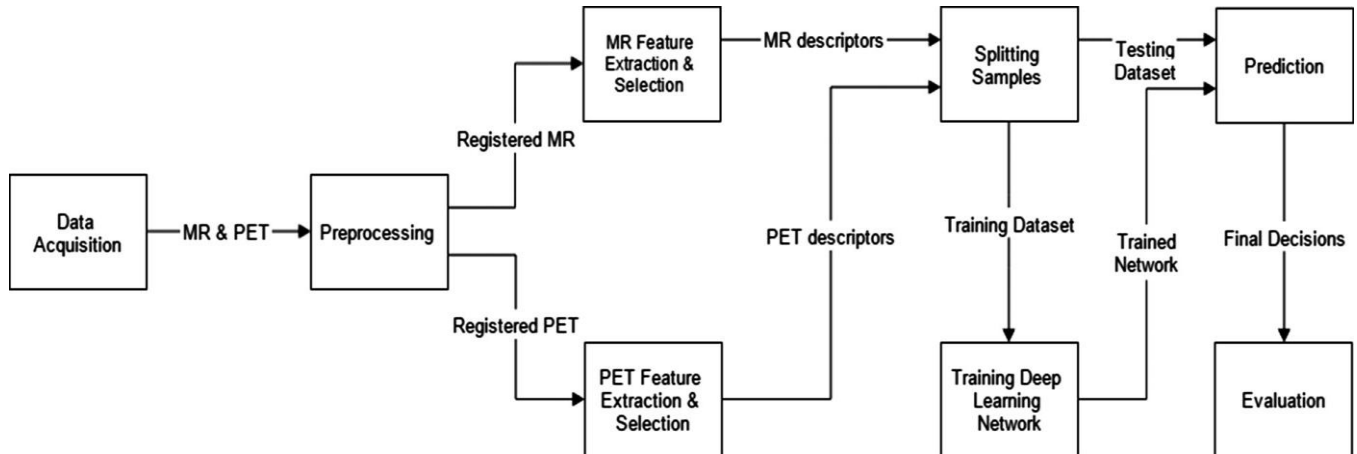


FIGURE 1: Block Diagram for Proposed System

### 2.2 Pre-processing & Enhancement

The collected MRI images first pre-processed and then segmented into some working parts. In pre-processing first we perform RGB to GRAY conversion in this conversion image is resize that is we actually convert 3D image into 2D image. Because 2D image take less time for detection. And then resize the image to reduce processing time. After pre-processing we enhance the image to find hide area. Because of enhancement hide area is visible and easily detects the node.

### 2.3 Segmentation of Pre-processed Image

After pre-processing and enhancement MRI image is segmented into no of working parts. Each working part has a feature which should be extracting. This dataset is first divided into training, testing and valuable purpose.

### 2.4 Feature Extraction

After segmentation we extract each working part feature. Feature extraction is a method of capturing visual content of an image. The feature extraction is the process to represent raw image in its reduced form to facilitate decision making such as pattern classification. Each feature is extracted in descriptor and statistically. Here mostly I used fourier descriptor and for statistical feature extraction I shall use standard deviation and variance. Each working part extracts the features like intensity, texture, shape etc.

### 2.5 Classification

In this study we are going to use artificial neural networks for classification. Artificial neural networks are computational model inspired by an animal's nervous systems in particular the brain which is capable of machine learning as well as pattern recognition. In artificial neural network use feed forward back propagation and because of that we can get accurate result. Here I shall use Levenberg learning algorithm as a learning method.

## III. EXPERIMENT AND RESULT

We created the system based on the artificial and check the result with multiple images. We used different dataset for training and testing purposes. Feature was extracted from the MRI brain scans with Alzheimer in different stages and also with no Alzheimer. The neural network was trained using these features and then tested using test data samples. The image samples included scans from people of different age group and sex.

Following is the user interface created for the system and the steps to perform the classification of the Alzheimer's disease.

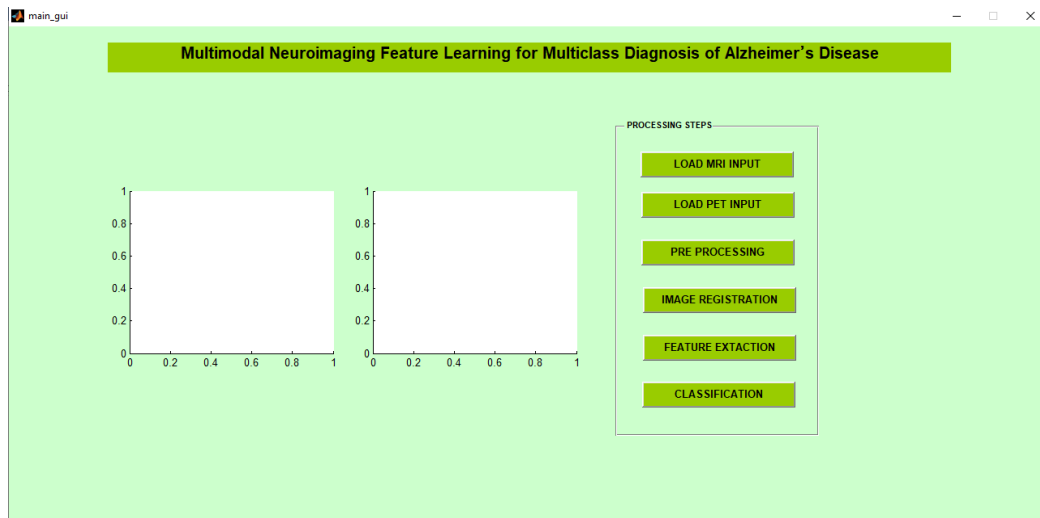


**FIGURE 2: Main Window**

When we click on first push button a window will appear containing number of test images. We then select one image from the set as an input image for the system. The input image is shown in the below figure.

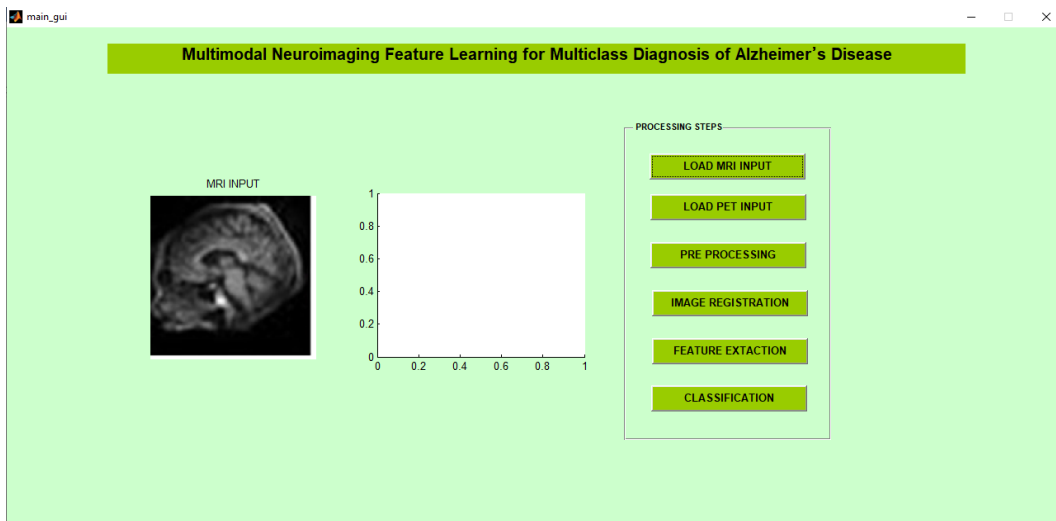


**FIGURE 3: Taking MRI image as input**

Next we will input the PET images from the sample set same as MRI images. This image will be shown in box next to the MRI image. The PET images were aligned with MRI image to give better biomarkers for the classification function.

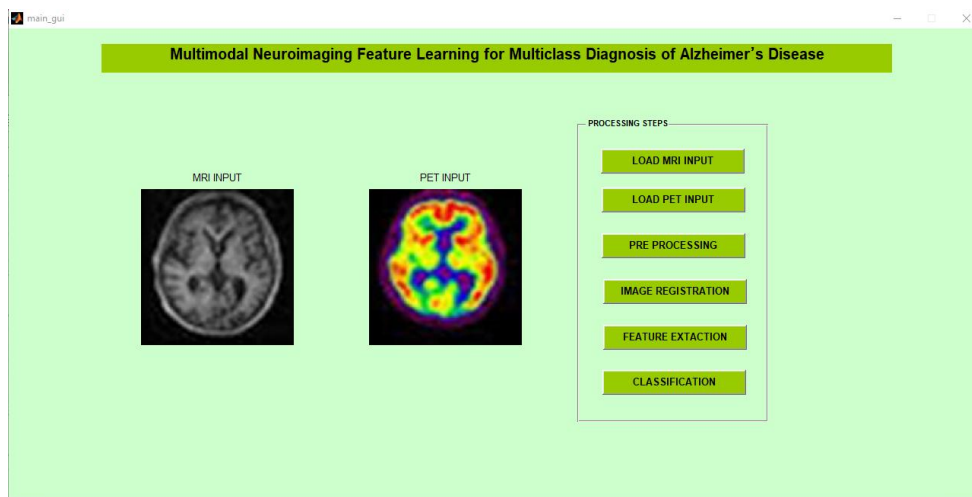


**FIGURE 4: Pre-processing of input images**

Next step is to pre-process the MRI and PET images. Pre-processing include denoising the images using filtering methods here we are using median filtering and convert the image in grey.

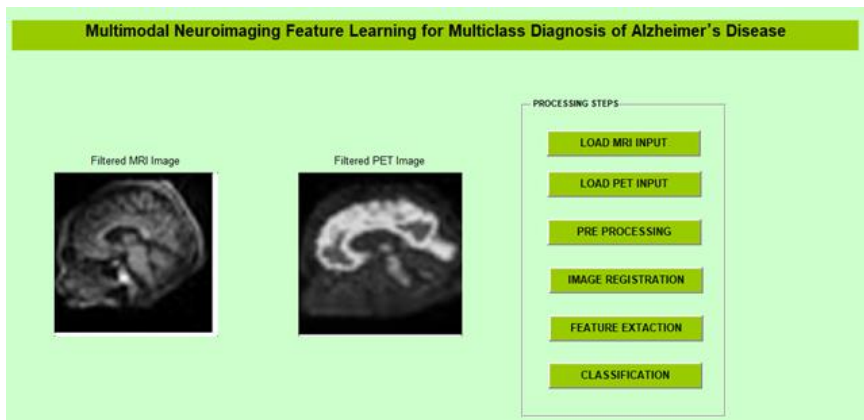


**FIGURE 5: Pre-processing of both the images**

Next process is image registration which includes image registration based on the intensities. This process will align the PET and MRI images using matched intensities of the two images. This will transform the various biomarkers from MRI and PET images into single coordinate system which will be easier to access when classifying the images in disease affected and non-affected set. Figure below shows registered images.



**FIGURE 6: Registration of the pet and MRI images**

Features are then extracted from the registered images. It is done using grey level co-occurrence matrix. This matrix will provide texture information based on number of times specific value pixels repeated in specific special location. These values will create a map showing abnormal growth in the scans using texture features of the images. Once the features are extracted it will show message box as in the figure below.

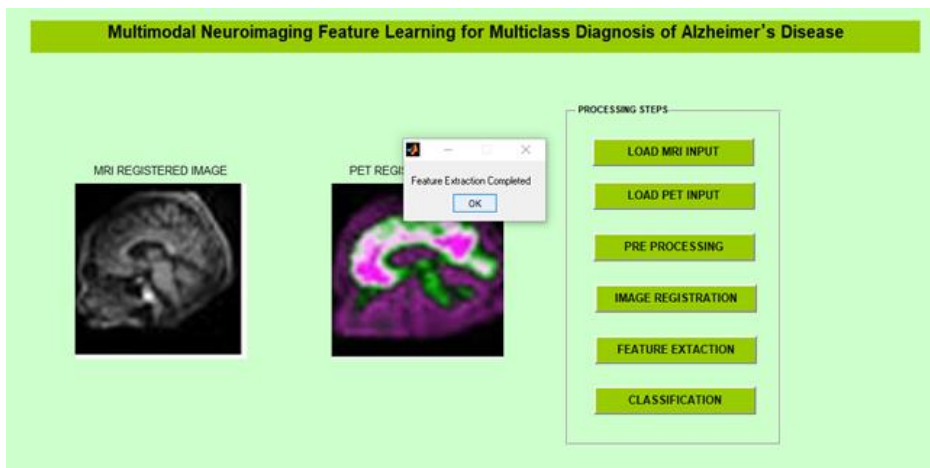


**FIGURE 7: Feature extraction from pet and MRI images**

Lastly we are doing classification using artificial neural network. The classifier matches extracted features from the dataset with features from test sample and provides result as Alzheimer's affected or Normal in the message box as shown in the below figures.

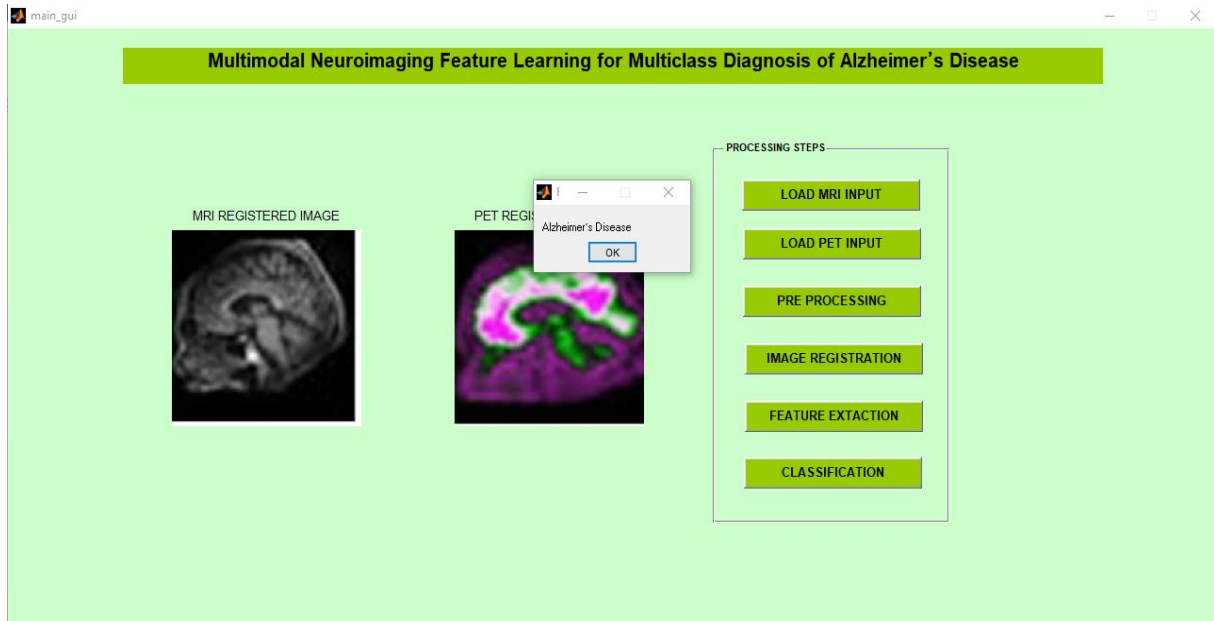


**FIGURE 8: Alzheimer's disease scans**

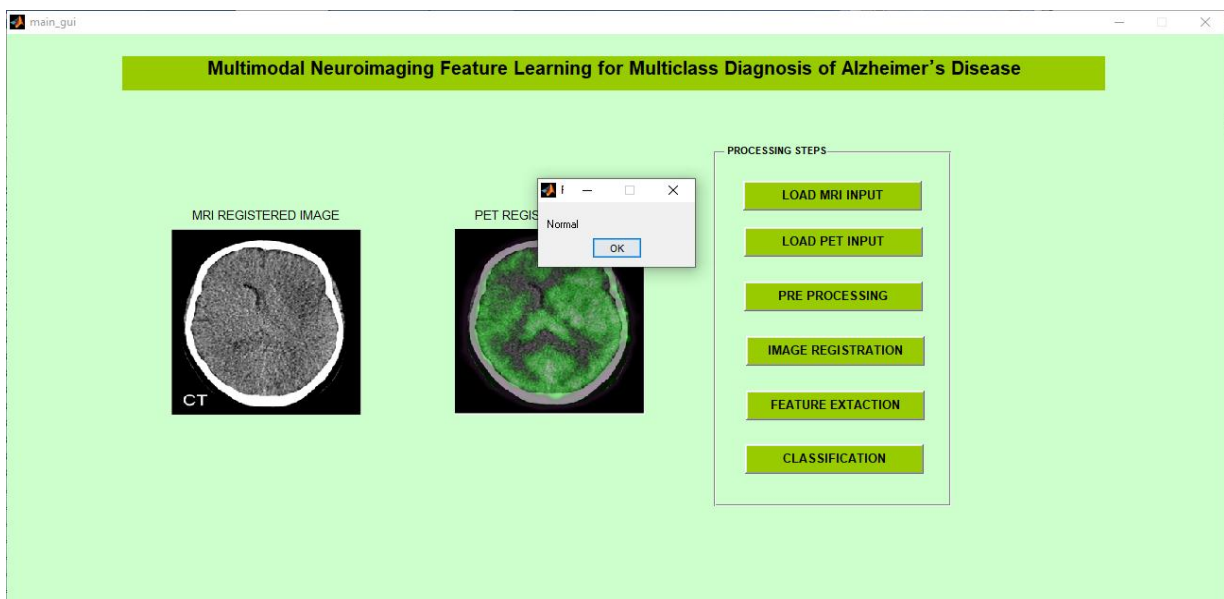


**FIGURE 9: Image classified as normal scan**

#### IV. CONCLUSION

We have experimented a system for Alzheimer's disease diagnosis and classification. The system can distinguish between normal and disease affected MRI scans with better accuracy. We can also extend this system to label more unlabeled data in the future. Grey level co-occurrence matrix used for feature extraction provides good feature bank for classification purpose. Neural network is best suited for these kinds of the classification and it gets better with more training samples comprising of different types of datasets. Proposed system is a powerful method to represent multimodal neuroimaging biomarkers.

#### REFERENCES

- [1] Siqi Liu., "Multimodal Neuroimaging Feature Learning for Multiclass Diagnosis of Alzheimer's disease," *IEEE transaction on biomedical engineering*, vol. 62, no. 4, April 2015.

- [2] G. McKhann *et al.*, "Clinical diagnosis of Alzheimer's disease report of the NINCDSADRDA Work Group under the auspices of Department of Health and Human Services Task Force on Alzheimer's disease," *Neurology*, vol. 34, no. 7, pp. 939-939, 1984.
- [3] R. Brookmeyer *et al.*, "Forecasting the global burden of Alzheimer's disease," *Alzheimer's Dementia*, vol. 3, no. 3, pp. 186-191, 2007.
- [4] B. Dubois *et al.*, "Research criteria for the diagnosis of Alzheimer's disease: Revising the NINCDSADRDA criteria," *Lancet Neurol.*, vol. 6, no. 8, pp. 734-746, 2007.
- [5] S. Gauthier *et al.*, "Mild cognitive impairment," *The Lancet*, vol. 367, no. 9518, pp. 1262-1270, 2006.
- [6] C. DeCarli, "Mild cognitive impairment: Prevalence, prognosis, aetiology, and treatment," *Lancet Neurol.*, vol. 2, no. 1, pp. 15-21, 2003.
- [7] C. Davatzikos *et al.*, "Prediction of MCI to AD conversion, via MRI, CSF biomarkers, and pattern classification," *Neurobiol. Aging*, vol. 32, no. 12, pp. 2322.e19-2322.e27, 2011.
- [8] R. Cuingnet *et al.*, "Automatic classification of patients with Alzheimer's disease from structural MRI: A comparison of ten methods using the ADNI database," *Neuroimage*, vol. 56, no. 2, pp. 766-781, 2011.
- [9] Y. Fan *et al.*, "Structural and functional biomarkers of prodromal Alzheimer's disease: A high-dimensional pattern classification study," *Neuroimage*, vol. 41, no. 2, pp. 277-285, 2008.
- [10] S. Liu *et al.*, "Multi-channel brain atrophy pattern analysis in neuroimaging retrieval," in *Proc. IEEE Int. Symp. Biomed. Imaging: From Nano to Macro*, 2013, pp. 206-209.
- [11] S. Liu *et al.*, "Neuroimaging biomarker based prediction of Alzheimer's disease severity with optimized graph construction," in *Proc. IEEE Int. Symp. Biomed. Imaging: From Nano to Macro*, 2013, pp. 1324-1327.
- [12] W. Cai *et al.*, "A 3D difference of Gaussian based lesion detector for brain PET," in *Proc. IEEE Int. Symp. Biomed. Imaging: From Nano to Macro*, 2014, pp. 677-680.
- [13] G. Chetelat *et al.*, "Mild cognitive impairment can FDG-PET predict who is to rapidly convert to Alzheimer's disease?" *Neurology*, vol. 60, no. 8, pp. 1374-1377, 2003.
- [14] R. Higdon *et al.*, "A comparison of classification methods for differentiating frontotemporal dementia from Alzheimer's disease using FDG-PET imaging," *Statist. Med.*, vol. 23, no. 2, pp. 315-326, 2004.

# ZnO Modified Bismuth Silicate Glasses Structural and Physical Properties

Md khademul Basher

Department of physics, University of Rajshahi

**Abstract**— Zinc bismuth silicate glasses with compositions

$40SiO_2 \cdot xZnO \cdot (60 - x)Bi_2O_3$  ( $x = 0,5,10,15,20,25,30,35,$  and  $40$ ) were prepared using standard melt-quench techniques and zinc solubility limits were estimated using X-ray diffraction techniques in the bismuth silicate glass scheme. Density was measured using the principle of Archimedes; the molar volume and density decreased with a rise in ZnO in the samples. The temperature of the glass transition ( $T_g$ ) was determined using differential calorimetry scanning (DSC) and is expected to raise with a rise in ZnO content. Raman and FTIR spectra were registered at room temperature and Raman and FTIR analysis demonstrates that in all glass compositions there are asymmetric and symmetric extended vibrations of Si-O bonds in  $SiO_4$  tetrahedral units and with reduction in  $Bi_2O_3$ , the input of symmetric vibrations starts to dominate resulting in enhanced compactness of the glass composition.

**Keywords**— ZnO, Bismuth silicate, DSC, Raman spectra, Infrared spectrum.

## I. INTRODUCTION

Heavy metal oxide-based glasses have drawn community attention for their outstanding IR transmission relative to standard glasses [1,2]. Bismuth oxide lenses are suitable for a broad spectrum of applications for optical and electronic instruments, mechanical sensors and window reflection [3,4].  $Bi_2O_3$  is not a classic glass former, but owing to elevated polarization and low field strength of  $Bi^{3+}$  ions, a glass network of  $BiO_3$  and  $BiO_6$  may be constructed in the presence of standard glass formers such as  $SiO_2$ ,  $PbO$  and  $Bi_2O_3$  [5]. The structural function  $Bi_2O_3$  plays in glasses, however, is complex.  $Bi_2O_3$  is appropriate for forming elevated refractive index, non-toxicity, broad range of transmission, and so on [6].  $SiO_2$  has an incredibly broad range of industrial apps in its multiple amorphous forms [7]. Several reports are available in literature on ZnO-  $Bi_2O_3$  with  $Bi_2O_3$  and  $TeO_2$ , CdO-ZnO- $V_2O_3$ ,  $V_2O_3$ -  $Bi_2O_3$ - $B_2O_3$  and  $V_2O_5$ -ZnO-  $Bi_2O_3$  systems [8–14], but  $SiO_2$ -ZnO-  $Bi_2O_3$  physical and structural trials are uncommon.

The objective of this document is to use XRD, DSC, FTIR, and Raman spectroscopy methods to explore the impact of ZnO on the physical and structural characteristics of bismuth silicate glass specimens.

## II. EXPERIMENTAL

The glass samples in scheme  $40SiO_2 \cdot xZnO \cdot (60 - x)Bi_2O_3$  with composition  $x=0,5,10,15,20,25,30,35,$  and  $40$  were prepared by standard melt-quenching technique using anal grade  $SiO_2$ ,  $Bi_2O_3$ , and ZnO chemicals. However, we also tried to synthesize the samples with  $x$ (ZnO content) higher than 40 but we couldn't achieve. The weighed amounts of  $SiO_2$ , ZnO and  $Bi_2O_3$  were well mixed with pestle mortar for the synthesis of samples and then the blend was drawn in silica crucible. The mixed crucible was then placed in an electrically heated muffle furnace and the temperature was slowly raised to  $1100^\circ C$  where the mixture was melted. For half an hour, the melt was kept at  $1100^\circ C$  and shaken for adequate mixing and homogeneity. The samples of coin-shaped glass were obtained by pouring and quenching the melt at room temperature between two plates of stainless steel. Glass sample density was evaluated using the Principle of Archimedes with water as a buoyant liquid. X-ray diffraction patterns were used to detect the amorphous character using the Rigaku Table Top X-ray Diffract meter (XRD). The glass transition temperature ( $T_g$ ) was determined using TA tools, Model No, from differential calorimetry scanning (DSC). Q600 SDT. Glass samples were heated to a temperature range of  $40^\circ C$  to  $1000^\circ C$  in the nitrogen atmosphere at a rate of  $20^\circ C / min$ . Infrared transmission spectra were registered over the range of 400 to  $2000\text{ cm}^{-1}$  at room temperature using Shimadzu FRIT-8001PC spectrometer. The powdered samples were carefully blended in a proportion of 1:20 by weight with dry KBrand then pallets were prepared under 8-9 tonnes stress. The Raman Spectra was registered using the back-scattering setup of the Renishaw Invia Reflex Micro Raman Spectrometer with Ar ion laser (514 nm).

### III. RESULTS AND DEBATE

$40SiO_2 \cdot xZnO \cdot (60 - x)Bi_2O_3$  prepared glass samples with  $x=0,5,10,15,20,25,30,35,$  and  $40$  were discovered to be colored light yellow. Figure 1 shows the XRD patterns of  $x=0,10,20,30$  and  $40$  glass samples. The existence of wide spectrum and lack of any sharp peak in X-ray diffractograms confirms the synthetic glass samples' amorphous nature. Table 1 shows the measured density values ( $\rho$ ) for all specimens. Perusal of the information described in Table 1 shows that sample density reduces as ZnO content increases. As heavier  $Bi_2O_3$  molecules are substituted with lighter ZnO molecules, this is the usual trend.

**TABLE 1**  
 **$40SiO_2 \cdot xZnO \cdot (60 - x)Bi_2O_3$  CRYSTAL TRANSITION TEMPERATURE ( $T_g$ ), MOLAR VOLUME ( $V_m$ ), AND DENSITY ( $\rho$ )[27]**

Compositions ( $x$ )	$\rho$ (g/cc)	$V_m$ (cc/mole)	$T_g$ ( $^{\circ}C$ )
0	6.73	45.11	451
5	6.60	43.08	471.85
10	6.4948	40.82	459.52
15	6.401	38.41	474
20	6.198	36.57	474
25	5.938	34.93	494
30	5.627	33.45	513
35	5.529	30.56	521
40	5.463	28.87	522

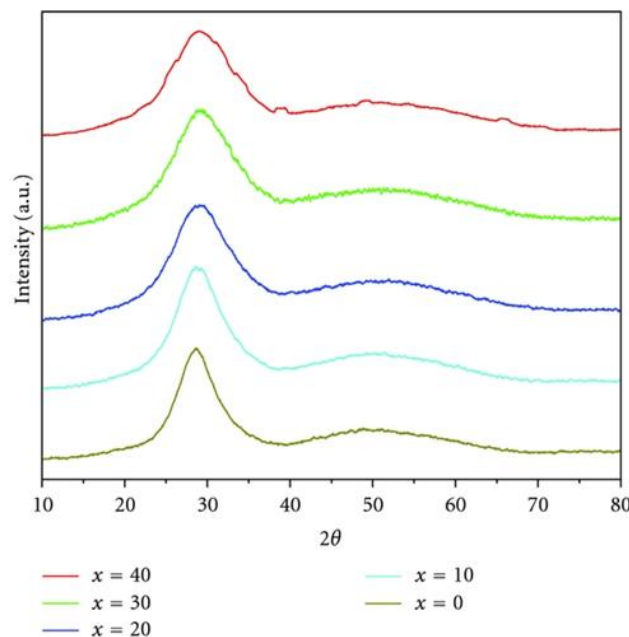


**FIGURE 1: XRD of various crystal compositions  $40SiO_2 \cdot xZnO \cdot (60 - x)Bi_2O_3$ . [27]**

Calculation of the molar quantity ( $V_m$ ) using the relationship

$$V_m = \frac{\sum x_i M_i}{\rho}$$

Wherever the density is  $\rho$ ,  $x_i$  and  $M_i$  respectively, represents the molar fraction and molecular weight of the component of  $i^{th}$  and density.  $V_m$  values are also shown in Table 1 and their composition variation is shown in Figure 2. Figure 2's perusal demonstrates that molar volume also reduces as ZnO content increases.

Similar results for  $V_2O_5-Bi_2O_3-ZnO$  [9] and  $Li_2O-Bi_2O_3-ZnO$  [15] glass structures were recorded in the literature. The results for  $40SiO_2 \cdot xZnO \cdot (60 - x)Bi_2O_3$  with  $x=0,5,10,15,20,25,30,35,40$  differential scanning calorimetry (DSC) are shown in Figure 3. The tendency to form glass and the thermal stability of glasses can be determined from  $T_g$  values.  $T_g$  is

noted to improve with a rise in the content of ZnO, suggesting an increase in the thermal stability of glass. A reduction in  $T_g$  connected with an rise in the content of heavy metal oxide in glass matrix may be linked to the opening of a network [16]. In the current glass scheme, therefore, the network compactness of the glass matrix improves with an increase in the content of ZnO.

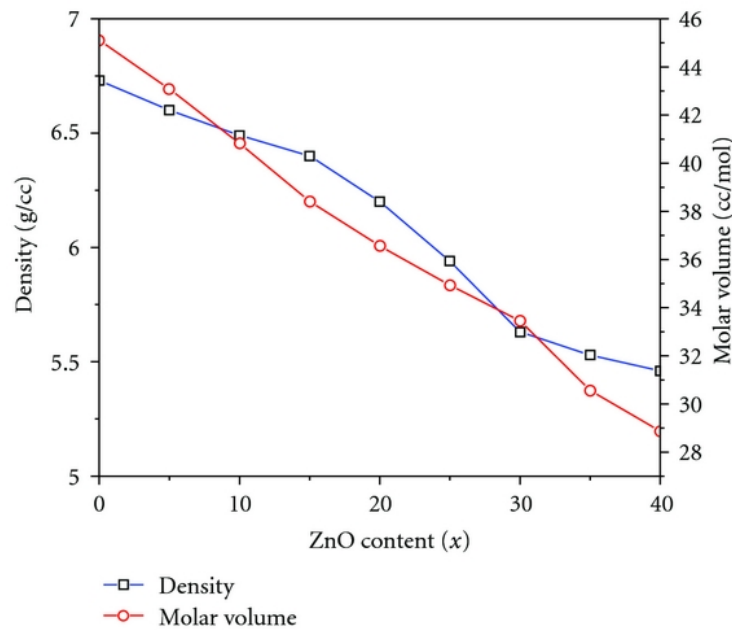


**FIGURE 2: Density ( $\pi$ ) and molar quantity ( $V_m$ ) compositional reliance for  $40SiO_2 \cdot xZnO \cdot (60 - x)Bi_2O_3$  lenses.[27]**

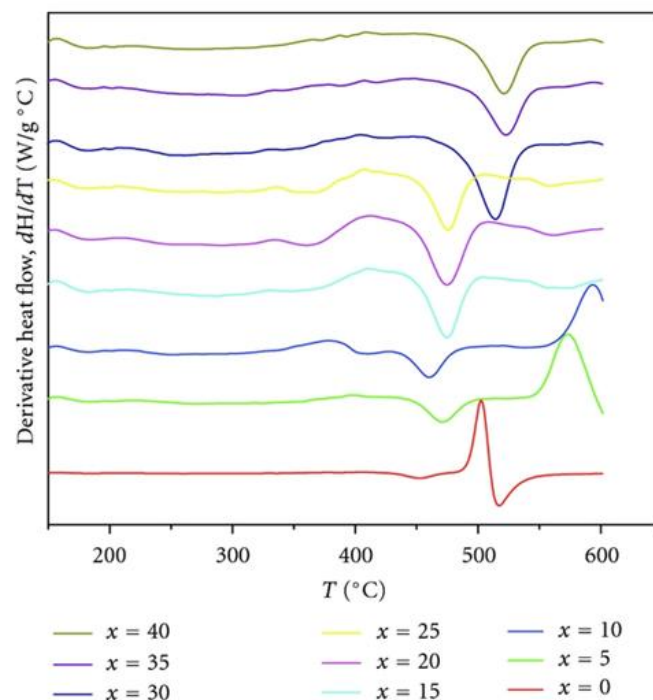


**FIGURE 3: Calorimetry differential scanning (DSC) curves for the  $40SiO_2 \cdot xZnO \cdot (60 - x)Bi_2O_3$  crystal scheme.[27]**

The tendency to form glass and the thermal stability of glasses can be determined from  $T_g$  values.  $T_g$  is noted to improve with a rise in the content of ZnO, suggesting an increase in the thermal stability of glass. A reduction in  $T_g$  connected with a rise in the content of heavy metal oxide in glass matrix may be linked to the opening of a network [16]. In the current glass scheme, the network compactness of the glass matrix rises as the content of ZnO rises.

For all  $40SiO_2 \cdot xZnO \cdot (60 - x)Bi_2O_3$  compositions, the Raman spectra are defined by three significant bands,  $\sim 120\text{ cm}^{-1}$ ,  $400\text{ cm}^{-1}$ , and a small wide band  $\sim 900\text{ cm}^{-1}$ . The FTIR spectrum is defined by two sharp absorption bands ranging from  $425$  to  $550\text{ cm}^{-1}$  (centered at about  $475\text{ cm}^{-1}$ ),  $800$  to  $1200\text{ cm}^{-1}$  (centered at approximately  $950\text{ cm}^{-1}$ ), a tiny band or flattening at  $720\text{ cm}^{-1}$  in all the glass specimens studied, and a tiny band occurs at around  $800\text{ cm}^{-1}$  in glass specimens for  $x=25,30,35$  and  $40$  as shown in Figure 5. In Raman spectra, the band between  $50$  and  $200\text{ cm}^{-1}$  (centered at about  $120\text{ cm}^{-1}$ ) is usually associated with vibrations involving  $Bi^{3+}$  cation movements in  $[BiO_6]$  and/or  $[BiO_3]$  units [17, 18]. Another  $400\text{ cm}^{-1}$  centered band can be attributed to the Bi–O–Bi and Bi–O stretching vibrations of  $BiO_6$  octahedral units [19, 20] and can be attributed to asymmetric Si–O–Si bending vibrations in  $SiO_4$  structural units [21, 22].

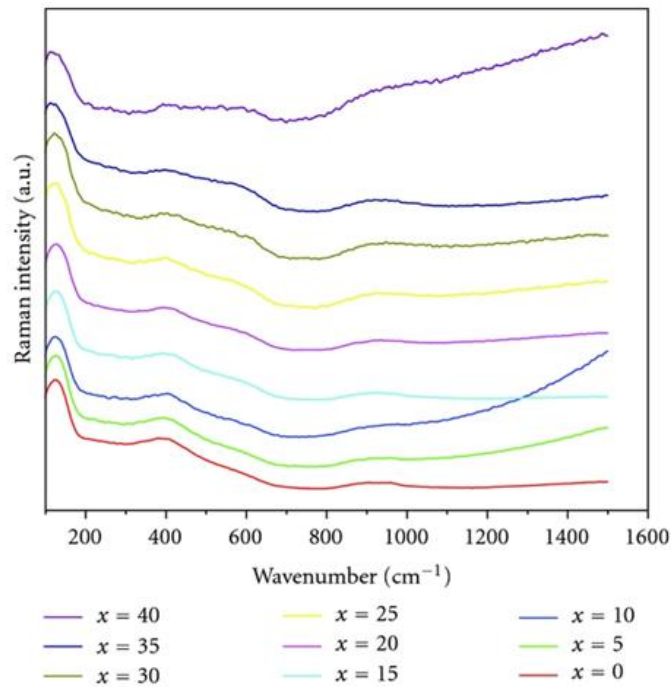


FIGURE 4: Raman spectra at room temperature for various  $40SiO_2 \cdot xZnO \cdot (60 - x)Bi_2O_3$  crystal compositions.[27]

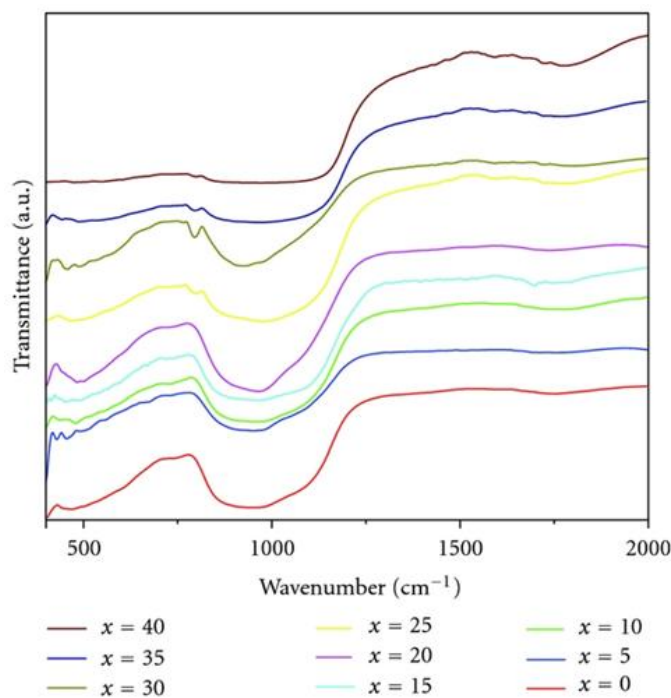


FIGURE 5: Infrared spectrum for various compositions of  $40SiO_2 \cdot xZnO \cdot (60 - x)Bi_2O_3$  at room temperature.[27]

The intensity of this band decreases with the decrease in  $Bi_2O_3$  content in present glass system, suggesting the presence of bismuth as network modifier in the form of  $BiO_6$  octahedral units. This is also supported by the FTIR data. In FTIR, bands ranging from  $425$  to  $550\text{ cm}^{-1}$  to  $800$  to  $1200\text{ cm}^{-1}$  are attributed to Bi–O–Bi and Bi–O  $BiO_6$  octahedra vibrations [17, 20, 23]. In  $BiO_3$  pyramidal units, Ardelean et al.[24] recorded a band at  $715\text{ cm}^{-1}$  owing to symmetric stretching vibrations of the Bi–O bond. Thus, the tiny kink found in all the glass compositions at  $720\text{ cm}^{-1}$  can be ascribed to symmetrical stretching vibrations of Bi–O bond in  $BiO_3$  pyramidal units. The Raman spectra of all compositions show a weak band around  $920\text{ cm}^{-1}$ , which may be attributed to the symmetric stretching vibrations of  $SiO_4$  with three non-bridging oxygens [21]. The position and intensity of this band remains same on wave number scale as per our expectations, as the  $SiO_2$  content remain same in all the compositions. It is also supported by the FTIR, where band is attributed to  $SiO_4$  tetrahedra's asymmetric stretching vibration mode between  $800$  and  $1200\text{ cm}^{-1}$ [17]. In glass samples with  $x=25,30,35$ , and  $40$ , there is a small but well-distinguished IR band at about  $800\text{ cm}^{-1}$ . For other glass compositions, this band is merged in the wide IR band from  $800\text{ cm}^{-1}$  to  $1200\text{ cm}^{-1}$ . The band is ascribed to Si–O symmetric stretched vibrations at around  $800\text{ cm}^{-1}$  in FTIR data [25]. The research of Raman and FTIR spectra demonstrates that there are asymmetric and symmetric extended  $SiO_4$  vibrations in all glass compositions and the input of symmetric vibrations starts to dominate with decreased  $Bi_2O_3$ . This may be due to the substitute of the bigger  $Bi_2O_3$  molecule with a lower ZnO molecule, leading to a reduction in the stretching of the silicate network. This may lead in an enhanced compactness of the glass framework, which is also demonstrated by a reduction in molar volume and an increase in  $T_g$ . Low frequency band present in FTIR data is assigned to vibrations of  $Zn^{2+}$  metal cations at around  $450\text{ cm}^{-1}$  in all glass samples [9]. A measure of the disturbance in the local framework is the length of Raman bands in disordered materials [26]. With a reduction in bismuth content, the Raman band length reduces indicating that the environment of bismuth in the current glass scheme is more distorted.

#### IV. CONCLUSION

Different studies such as X-ray diffraction, density and DSC conducted on  $40SiO_2 \cdot xZnO \cdot (60-x)Bi_2O_3$  for, ( $x=0,5,10,15,20,25,30,35$ , and  $40$ ) show that stable glasses are acquired for up to  $40$  glasses; the glass forming trend and thermal stability of these glasses increases with an rise in ZnO content. For higher concentration of ZnO that is, more than  $x=40$ , glass formation becomes difficult in the present physical conditions and this may be taken as the solubility limit of ZnO in present glass system. It is noted that the density of these glasses decreases with an rise in ZnO content. The input of symmetric vibrations of Si–O bonds in  $SiO_4$  tetrahedral units dominates asymmetric vibrations when ZnO is added to the bismuth silicate structure.  $Bi_2O_3$  plays both the former glass and the modifier role in the current study system.

#### ACKNOWLEDGEMENTS

I am thankful to my parent for support me lot. I also thankful to my friends Musabbir who support me a lot with share his knowledge about research with me and suggest me in many ways to doing this research.

#### REFERENCES

- [1] Y. Fujimoto and M. Nakatsuka, "Infrared luminescence from bismuth-doped silica glass," *Japanese Journal of Applied Physics*, vol. 40, pp. L279–L281, 2001. View at: [Publisher Site](#) | [Google Scholar](#).
- [2] X. G. Meng, J. R. Qiu, M. Y. Peng et al., "Near infrared broadband emission of bismuth-doped aluminophosphate glass," *Optics Express*, vol. 13, no. 5, pp. 1628–1634, 2005. View at: [Publisher Site](#) | [Google Scholar](#).
- [3] I. Oprea, H. Hesse, and K. Betzler, "Optical properties of bismuth borate glasses," *Optical Materials*, vol. 26, no. 3, pp. 235–237, 2004. View at: [Publisher Site](#) | [Google Scholar](#).
- [4] M. Łaczka, L. Stoch, and J. Górecki, "Bismuth-containing glasses as materials for optoelectronics," *Journal of Alloys and Compounds*, vol. 186, no. 2, pp. 279–291, 1992. View at: [Google Scholar](#).
- [5] Y. Zhang and T. Guo, "Study on the sealing glass of lower melting point in system  $Li_2O$ – $ZnO$ – $SiO_2$ ," *Vacuum Electronics*, vol. 2, pp. 43–45, 2006. View at: [Google Scholar](#).
- [6] Y. Zhang, Y. Yang, J. Zheng, W. Hua, and G. Chen, "Effects of oxidizing additives on optical properties of  $Bi_2O_3$ – $B_2O_3$ – $SiO_2$  glasses," *Journal of American Ceramic Society*, vol. 91, no. 10, pp. 3410–3412, 2008. View at: [Publisher Site](#) | [Google Scholar](#).
- [7] G. H. Beall, "Design and properties of glass-ceramics," *Annual Review of Materials Science*, vol. 22, no. 1, pp. 91–119, 1992. View at: [Google Scholar](#).
- [8] L. Baia, R. Stefan, W. Kiefer, and S. Simon, "Structural characteristics of  $B_2O_3$ – $Bi_2O_3$  glasses with high transition metal oxide content," *Journal of Raman Spectroscopy*, vol. 36, no. 3, pp. 262–266, 2005. View at: [Publisher Site](#) | [Google Scholar](#).

- [9] R. Punia, R. S. Kundu, J. Hooda, S. Dhankhar, S. Dahiya, and N. Kishore, "Effect of  $\text{Bi}_2\text{O}_3$  on structural, optical, and other physical properties of semiconducting zinc vanadate glasses," *Journal of Applied Physics*, vol. 110, no. 3, Article ID 033527, 6 pages, 2011. View at: [Google Scholar](#).
- [10] D. Saritha, Y. Markandeya, M. Salagram, M. Vithal, A. K. Singh, and G. Bhikshamaiah, "Effect of  $\text{Bi}_2\text{O}_3$  on physical, optical and structural studies of  $\text{ZnO-Bi}_2\text{O}_3\text{-B}_2\text{O}_3$  glasses," *Journal of Non-Crystalline Solids*, vol. 354, no. 52-54, pp. 5573-5579, 2008. View at: [Publisher Site](#) | [Google Scholar](#).
- [11] H. Doweidar and Y. B. Saddeek, "FTIR and ultrasonic investigations on modified bismuth borate glasses," *Journal of Non-Crystalline Solids*, vol. 355, no. 6, pp. 348-354, 2009. View at: [Publisher Site](#) | [Google Scholar](#).
- [12] J. Ozdanova, H. Ticha, and L. Ticky, "Remark on the optical gap in  $\text{ZnO-Bi}_2\text{O}_3\text{-TeO}_2$  glasses," *Journal of Non-Crystalline Solids*, vol. 353, no. 29, pp. 2799-2802, 2007. View at: [Publisher Site](#) | [Google Scholar](#).
- [13] G. López-Calzada, M. E. Zayas, M. Ceron-Rivera et al., "Optical characterization of novel matrix glasses based on a  $\text{CdO:ZnO:V}_2\text{O}_5$  ternary system," *Journal of Non-Crystalline Solids*, vol. 356, no. 6-8, pp. 374-377, 2010. View at: [Publisher Site](#) | [Google Scholar](#).
- [14] C. Tripon, D. Toloman, M. Aluas, C. Filip, and I. Ardelean, "Structural investigation of the  $x\text{V}_2\text{O}_5(1-x)[\text{Bi}_2\text{O}_3\text{-B}_2\text{O}_3]$  glasses by IR absorption, EPR and NMR," *Journal of Optoelectronics and Advanced Materials*, vol. 8, no. 3, pp. 1129-1131, 2006. View at: [Bi2O3-B2O3%20glasses%20by%20IR%20absorbtion,%20EPR%20and%20NMR&author=C.Tripon&author=D.Toloman&author=M.Aluas&author=C.Filip&author=I.Ardelean&publication\\_year=2006" target="blank">Google Scholar](#).
- [15] S. Bale and S. Rahman, "Glass structure and transport properties of  $\text{Li}_2\text{O}$  containing zinc bismuthate glasses," *Optical Materials*, vol. 31, no. 2, pp. 333-337, 2008. View at: [Publisher Site](#) | [Google Scholar](#).
- [16] V. C. S. Reynoso, L. C. Barbosa, O. L. Alves, N. Aranha, and C. L. Cesar, "Preparation and characterization of heavy-metal oxide glasses:  $\text{Bi}_2\text{O}_3\text{-PbO-GeO}_2\text{-B}_2\text{O}_3$  system," *Journal of Materials Chemistry*, vol. 4, no. 4, pp. 529-532, 1994. View at: [Google Scholar](#).
- [17] C. A. Geiger, "A powder infrared spectroscopic investigation of garnet binaries in the system  $\text{Mg}_3\text{Al}_2\text{Si}_3\text{O}_{12}\text{-Fe}_3\text{Al}_2\text{Si}_3\text{O}_{12}\text{-Mn}_3\text{Al}_2\text{Si}_3\text{O}_{12}\text{-Ca}_3\text{Al}_2\text{Si}_3\text{O}_{12}$ ," *European Journal of Minerals*, vol. 10, pp. 407-422, 1998. View at: [Google Scholar](#).
- [18] A. Ghosh, S. Bhattacharya, and A. Ghosh, "Optical and other physical properties of semiconducting cadmium vanadate glasses," *Journal of Applied Physics*, vol. 101, no. 8, Article ID 083511, 4 pages, 2007. View at: [Publisher Site](#) | [Google Scholar](#).
- [19] L. Baia, R. Stefan, J. Popp, S. Simon, and W. Kiefer, "Structural investigations of copper doped  $\text{B}_2\text{O}_3\text{-Bi}_2\text{O}_3$  glasses with high bismuth oxide content," *Journal of Non-Crystalline Solids*, vol. 303, no. 3, pp. 379-386, 2002. View at: [Publisher Site](#) | [Google Scholar](#).
- [20] L. Baia, R. Stefan, J. Popp, S. Simon, and W. Kiefer, "Vibrational spectroscopy of highly iron doped  $\text{B}_2\text{O}_3\text{-Bi}_2\text{O}_3$  glass systems," *Journal of Non-Crystalline Solids*, vol. 324, no. 1-2, pp. 109-117, 2003. View at: [Publisher Site](#) | [Google Scholar](#).
- [21] P. McMillan, "Structural studies of silicate glasses and melts-applications and limitations of Raman spectroscopy," *American Mineralogist*, vol. 69, no. 7-8, pp. 622-644, 1984. View at: [Google Scholar](#).
- [22] M. Todea and S. Simon, "Vibrational spectroscopic study on iron doped silicabismuthate glasses and glass ceramics," *Journal of Optoelectronics and Advanced Materials*, vol. 9, no. 3, pp. 621-624, 2007. View at: [Google Scholar](#).
- [23] A. A. Kharlamov, R. M. Almeida, and J. Heo, "Vibrational spectra and structure of heavy metal oxide glasses," *Journal of Non-Crystalline Solids*, vol. 202, no. 3, pp. 233-240, 1996. View at: [Publisher Site](#) | [Google Scholar](#).
- [24] I. Ardelean, S. Cora, and D. Rusu, "EPR and FT-IR spectroscopic studies of  $\text{Bi}_2\text{O}_3\text{-B}_2\text{O}_3\text{-CuO}$  glasses," *Physica B*, vol. 403, no. 19-20, pp. 3682-3685, 2008. View at: [Publisher Site](#) | [Google Scholar](#).
- [25] B. J. Saikia, G. Parthasarathy, and N. C. Sarmah, "Fourier transform infrared spectroscopic estimation of crystallinity in  $\text{SiO}_2$  based rocks," *Bulletin of Materials Science*, vol. 31, no. 5, pp. 775-779, 2008. View at: [Publisher Site](#) | [Google Scholar](#).
- [26] B. N. Meera and J. Ramakrishna, "Raman spectral studies of borate glasses," *Journal of Non-Crystalline Solids*, vol. 159, no. 1-2, pp. 1-21, 1993. View at: [Google Scholar](#).
- [27] J. Hooda, R. Punia, R. S. Kundu, Sunil Dhankhar and N. Kishore, "Structural and Physical Properties of  $\text{ZnO}$  Modified Bismuth Silicate Glasses".

# Optimization of IBOM Power Plant (PG9171) using Fault Prediction on Gas Path Analysis

Nwaorgu.G.O<sup>1</sup>, Pullah.A<sup>2</sup>

Department of Marine Engineering, Faculty of Engineering, Nigeria Maritime University, Delta State, Nigeria.

**Abstract**— Almost from the inception of the gas turbine engine (GT), users and engine manufacturers have sought an effective technique to determine the health of the gas-path components (fan, compressors, combustor, turbines) based on available gas-path measurements. The potential of such tools to save money by anticipating the need for overhaul and providing help in work scope definition is substantial, provided they produce reliable results. It furthermore therefore became desirable to monitor the engine performance and diagnose the fault even before the damage is done since the fault can cause permanent damage to the components. Preventive maintenance proves to be a better way considering the longer run. This project thus work describes how modern gas-path analysis can be used as a tool for gas turbine diagnosis. Gas path analysis is studied with the aid of fault predictions obtained from using fuzzy logic was found to be a more suitable method for gas turbine diagnosis because the set of fuzzy rules are described using common language. MATLAB Simulink environment is also used to predict the degree of fault in the gas turbine through its Gas path analysis. The linguistic variables used as inputs are temperature, pressure and speed while the linguistic variable used as output is failure. The universe of discourse for temperature is between [0, 55], pressure is [0, 1000], shaft speed is [0, 5000] and failure which is the fault is [0, 1]. A type 1 fuzzy logic model and the center of gravity method are used as the defuzzification module. From the results it is seen that the value for the highest possible fault is 0.909 and the lowest is 0.217 at 6.3 and 52.7 °C respectively. This research shows that the fault prediction probability increases at higher operating conditions of the gas turbine.

**Keywords**— Gas Turbine, Fault Prediction, Gas Path Analysis, MATLAB Simulink, Fuzzy Logic.

## I. INTRODUCTION

The gas turbine is the most versatile item of turbo machinery today [1]. It can be used in several different modes in critical industries such as power generation, aviation, marine propulsion etc. However, the need to develop accurate and reliable models of GT for different objectives and applications has been a strong motivation for researchers to continue to work in this fascinating area.

This lends credence to the fact that models and control methodologies, based on white-box approaches rely on thermodynamic and energy balance equations, which are coupled and have a high degree of nonlinearity [2]. Consequently, models and control systems that are built with such simplified and/or non linearized equations are not accurate enough to capture system dynamics precisely. These models cannot account for the individual nuances of operating equipment and are not able to accommodate changes as the equipment ages [1]. Therefore, considering assumptions and using linearization methods for simplification and solving these complex dynamics are unavoidable.

The basic operation of a GT is Brayton cycle with air as the working fluid. The machine has three main components. The compressor which draws air into the turbine and pressurizes it, the combustion system typically made up of fuel injectors that injects a steady stream of fuel into the combustion chamber where it mixes with the air and burned at a temperature of more than 1093°C producing a high temperature- high pressure gas stream and the turbine made up of an intricate array of alternate stationary and rotating aerofoil section blades where the high temperature-high pressure gas expands and spins the rotating blade of the turbine. The rotating blade of the turbine performs a dual function. They drive the compressor to draw more compressed air into the combustion chamber and they spin a generator to produce power. A fourth component is often used to increase efficiency (turbo prop, turbofan) to convert power into mechanical or electrical form (turbo shaft, electric generator) or to achieve greater power to mass/volume ratio (after burner).

There is a rich source of research activities in the area of modeling, simulation optimization and control of GT, particularly using thermodynamic analysis and very few on other methods. However, in spite of all the efforts already done in this all important field, there is need to redirect our attention and focus extensively to other tools, models and software in order to resolve problems encountered during the processes of design, manufacturing, operation, maintenance and optimization of GT.

The following problem can be highlighted in the existing models and control systems of GT: The models and control methodologies, based on thermodynamic and energy balance equations, which are coupled and have a high degree of nonlinearity are not accurate enough to capture system dynamics precisely [3]. These models cannot account for the individual nuances of operating equipment and are not able to accommodate changes as the equipment ages, deteriorate gradually losing their operability and efficiency.

Therefore, considering assumptions and using gas path analysis to develop accurate and reliable models of GT for different objectives, application, simplification and solving these complex dynamics are unavoidable. Fault prediction offers such potentials and shall be utilize to develop a model for the performance optimization of GT in this work. This research shows how the application of fault prediction on the gas path parameters can be used for engine performance monitoring and targets the detection of core engine deterioration. Gas path analysis (GPA) technique is used to access the condition of individual engine component based on the aero-thermodynamic relationship that exists between components and direct measurement of gas path parameter.

## II. RESEARCH GAP

This section shall present a comprehensive overview of some paramount research related to this work covering both the use of condition monitoring and gas path analysis. Odokwo et al applied graph networks approach to analyze and model a single-shaft open-cycle GT [4]. They used graph theory and algorithms to identify pressure and temperature drops, work transfer rates, rate of heat, and other system properties. Shalan et al investigated the comparative study on modeling of gas turbines in combined cycle power plants [5].

Simulink-VISUAL BASIC was used to investigate the stability of the turbine and its control system against overheat, as well as changes in frequency and load. The results showed that the existence of speed, frequency, and air control loops were necessary for the plant stability against disturbances. MarekDzida and Olszewski conducted a study on Comparing combined GT/steam turbine and marine low speed piston engine/steam turbine systems in naval applications [6].

The Monitoring and supervision of performance degradation is a widely studied topic in the gas turbine diagnosis research field where the performance parameters are estimated with different methods. If reliable performance estimations are available, it can be easier for the service engineers to efficiently plan service and maintenance of the gas turbine [7]. Saravanamuttoo *et al* investigated how compressor fouling affects the performance parameters using a linear fouling model [8].

Gas path analysis has a big influence on the gas turbine engine health and control. It has become one of the techniques in favour of condition maintenance strategy [9]. According to Jasmani *et al* the effectiveness of GPA using the measurement set selected with the introduced measurement selection method are then compared with the result of using standard measurement installed on existing GT [10]. Sajeev opined that GPA is very useful in terms of obtaining quantitative values of deterioration for multiple faults [11].

Urban stated that measurable engine parameters are treated as dependent variables, changes in which are mathematically interrelated to changes in component performance brought about by physical engine faults [12]. Provost stated that techniques are also presented for determining the gas path measurement in a GT that are needed to enable the required analysis of component changes and/or sensor biases to be performed [13].

## III. METHODOLOGY

The gas turbine under study is PG9171 manufactured by general electric. It operates at a speed of 5000rpm. The gas turbine is used for electric power generation and has an output power of 132MW. It has an efficiency of 34.6%. The maximum and minimum ambient temperatures are 267K and 326K respectively. The technical descriptions of the above stated GT is shown in appendix A. The concept applied is based on GPA and AI. It relies on performance parameter trending at standardized conditions so that it can be compared to actual performance. As discussed earlier, a deviation in the measured gas parameter can be accounted because of the deviation in component health [4].

### 3.1 Thermodynamic Theory of Gas Turbine

In the GT cycle (topping cycle) as shown in fig 1, the air is compressed isentropically in the compressor from state 1 to 2 where its temperature rises from  $T_1$  to  $T_2$ . The compressed air then enters the combustion chamber where the combustion of fuel takes place isobarically [14]. According to Ogbonnaya and Ugwu the thermodynamic theory is shown below:

The relationship between gas path measurable parameters is:

$$\frac{T_2}{T_1} = (rp)^{\gamma-1/\gamma} \quad (1)$$

$$T_2 = T_1(rp)^{\gamma-1/\gamma} \quad (2)$$

And

$$T_3 = T_4(rp)^{\gamma-1/\gamma} \quad (3)$$

Where,

$T_1$  = Compressor inlet temperature

$T_2$  = Compressor outlet temperature

$T_3$  = Turbine inlet temperature

$T_4$  = Turbine outlet temperature

$r_p$  = Pressure ratio denoted by  $\frac{P_2}{P_1}$

The work done by compressor is given as;

$$W_C = MC_p(T_2 - T_1) \quad (4)$$

Heat supplied to the combustor component

$$Q_{23} = MC_p(T_3 - T_2) \quad (5)$$

The Work done at turbine is given as;

$$W_T = MC_p(T_3 - T_4) \quad (6)$$

Heat rejected by the system is given as;

$$Q_{41} = MC_p(T_4 - T_1) \quad (7)$$

Where M = mass of air

$C_p$  = specific heat capacity of air at constant pressure

According to Cengel and Boles thermal efficiency of the gas turbine can be calculated using [15].

$$\eta = \frac{MC_p(T_3-T_4)-MC_p(T_2-T_1)}{MC_p(T_3-T_2)} \quad (8)$$

This can also be written as;

$$\eta = \frac{W_T - W_C}{Q_{23}} \quad (9)$$

*Compressor Health Parameter*

$$S_{f_c}, f_c = \frac{G_{c,cor,deg}}{G_{c,cor}} \quad (10)$$

$$\Delta S_{f_c}, f_c = \frac{(G_{c,cor,deg} - G_{c,cor})}{G_{c,cor}} \quad (11)$$

$$S_{f_c}, E_{ff} = \frac{\eta_{c,deg}}{\eta_c} \quad (12)$$

$$\Delta S_{f_c}, E_{ff} = \frac{(\eta_{c,deg} - \eta_c)}{\eta_c} \quad (13)$$

Where,

$S_{f_c}, F_c$  = Compressor flow capacity index

$G_{c,cor}$  = Compressor corrected flow when the compressor is healthy

$G_{C,cordeg}$  = Compressor corrected flow capacity when the compressor is degraded

$S_{FC}, E_{ff}$  = Compressor isentropic efficiency index

$\eta_C$  = Compressor isentropic efficiency index when the compressor is healthy

$\eta_{C,deg}$  = Compressor isentropic efficiency index when the compressor is degraded

*Combustor Health Parameter*

$$S_{fB}, E_{ff} = \frac{\eta_{B,deg}}{\eta_B} \quad (14)$$

$$\Delta S_{fB}, E_{ff} = \frac{\eta_{B,deg} - \eta_B}{\eta_B} \quad (15)$$

Where,

$S_{FB}, E_{FF}$  = Combustor isentropic efficiency index

$\eta_B$  = Combustor efficiency index when the combustor is healthy

$\eta_{B,deg}$  = Combustor efficiency index when the combustor is degraded

The performance of actual combustor can be expressed as follows;

$$\eta_{B,deg} = \vec{f}(\text{load}, \Delta S_{FB}, E_{ff}) \quad (16)$$

Where, Load = engine load power

*Turbine Health Parameters*

$$S_{FT}, F_C = \frac{(G_{T,cor,deg})}{G_{T,cor}} \quad (17)$$

$$\Delta S_{FT}, F_C = \frac{(G_{T,cor,deg} - G_{T,cor})}{G_{T,cor}} \quad (18)$$

$$S_{FT}, E_{ff} = \frac{(\eta_{T,deg})}{\eta_T} \quad (19)$$

$$\Delta S_{FT}, E_{ff} = \frac{(\eta_{T,deg} - \eta_T)}{\eta_T} \quad (20)$$

Where,

$S_{FT}, F_C$  = Turbine flow capacity index

$G_{T,cor}$  = Turbine corrected flow when the turbine is healthy

$G_{T,cor,deg}$  = Turbine corrected flow when the turbine is degraded

$S_{FT}, E_{FF}$  = Turbine isentropic efficiency index

$\eta_T$  = Turbine isentropic efficiency when the turbine is healthy

$\eta_{T,deg}$  = Turbine isentropic efficiency when the turbine is degraded

### 3.2 Gas Path Analysis

The GPA algorithm can be summarized into the main steps:

- (i) measurement normalization
- (ii) reference value generation,
- (iii) estimation of performance deviation, and
- (iv) diagnosis decision and this algorithm was introduced by Urban

The GPA method is based on thermodynamic relationships where one of the main objectives is to estimate deterioration in gas path components from a number of measured sensor signals which are denoted as measurement deltas ( $\Delta$ ). These

equations could be used to estimate steady state and transient variations in the performance parameters for an arbitrary gas turbine engine during most conceivable sets of input conditions

$$\Delta Y = X\Delta X + C \tag{21}$$

Where,  $\Delta Y$  is the gas path measured parameter deltas,  $\Delta x$  is the deviation in performance,  $X$  is the influence coefficient matrix presented in Urban (1992), and  $C$  is the measurement noise. Elements in  $\Delta Y$  are typically: spool speeds  $\Delta N$ , temperatures  $\Delta T$ , and pressures  $\Delta P$ . Elements in  $\Delta X$  are typically: efficiencies  $\Delta \eta$ , and flow capacities  $\Delta \Gamma$  of the gas path components such as compressors, turbines, and fans. The matrix  $X$  can be divided into two parts:

- (i) An engine fault influence matrix  $X_e$ , and
- (ii) A sensor fault influence matrix  $X_s$ , where the previous defined matrix  $X$  and health parameter  $\Delta x$  in equation (10) is extended with the sensor fault dependencies. To simplify the mathematics, the sensor measurement noise vector is assumed to be Gaussian with a zero mean.

#### IV. RESULT AND DISCUSSION

The number of rules used in this system is 27, calculated as  $Terms^{Variables} = 3^3 = 27$ . The fuzzy rule shows the combination of the MF terms used to determine the extent of the fault and generate five linguistic terms in the fault probability which are very low (VL), low (L), moderate (M), high (H) and very high (VH). The fuzzy rule used in this project is presented in table 2.

**TABLE 2  
FUZZY RULES**

	A	B	C	D
1	Temperature	Pressure	Shaft Speed	Fault Probability
2	L	L	L	VL
3	L	L	M	VL
4	L	L	H	L
5	L	M	L	VL
6	L	M	M	L
7	L	M	H	M
8	L	H	L	L
9	L	H	M	M
10	L	H	H	H
11	M	L	L	VL
12	M	L	M	L
13	M	L	H	M
14	M	M	L	L
15	M	M	M	M
16	M	M	H	H
17	M	H	L	M
18	M	H	M	H
19	M	H	H	VH
20	H	L	L	L
21	H	L	M	M
22	H	L	H	H
23	H	M	L	M
24	H	M	M	H
25	H	M	H	VH
26	H	H	L	H
27	H	H	M	VH
28	H	H	H	VH

### 4.1 Membership Function Plot for Faults

The fault prediction values (y axis) is taken between 0.217 and 0.909 and the number of points (x axis) is as shown in table 2. The result is shown in figure 3 to 6, it can be seen that the value for the highest possible fault (y axis) is 0.909. It was observed that at higher temperature, pressure and shaft speed as shown in fig 4 to fig 6 that there is a rapid increase in fault prediction which increases the probability of failure of operating the gas turbine at these conditions.

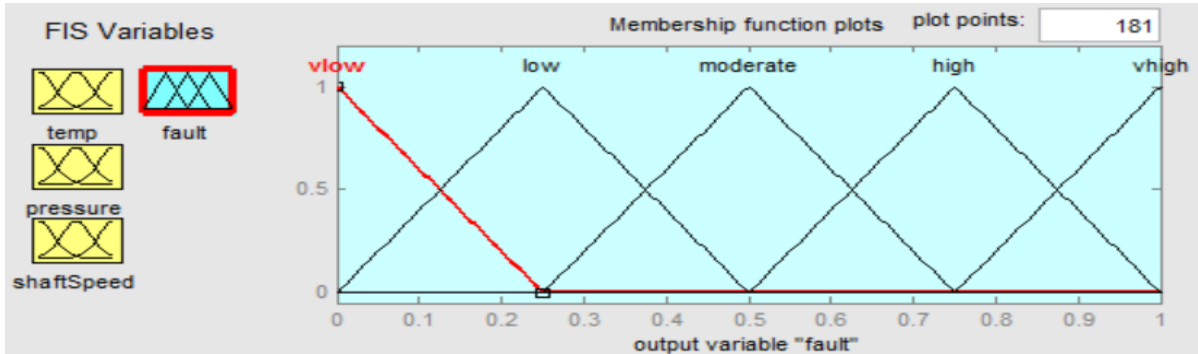


**FIGURE 3: Membership function plot for Failure**

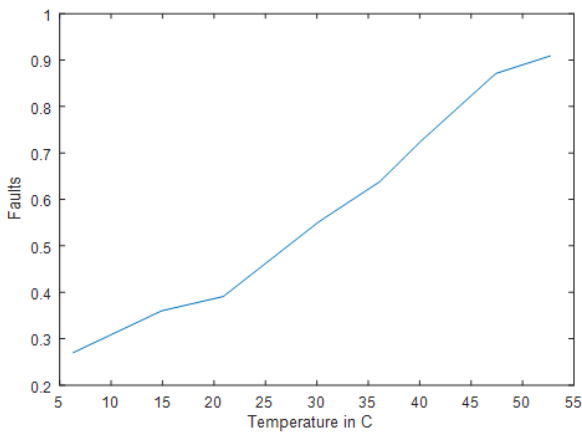


**FIGURE 4: Temperature against Faults**

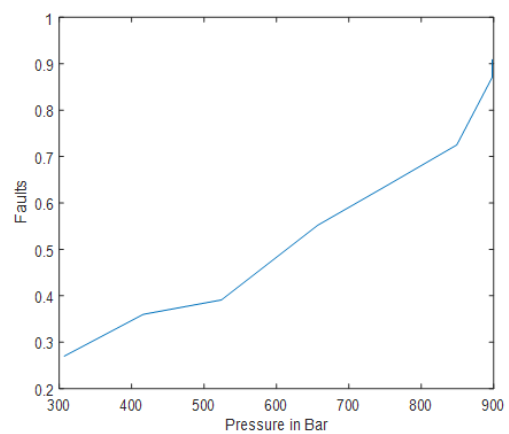


**FIGURE 5: Pressure against Faults**

There is rapid increase in temperature at 23 °C to 48 °C and a relative change from 0.4 to 0.909 in faults prediction. These changes can be seen to cause a bend in the figures above and faults is most likely to occur at this. The GT will experience less occurrence of faults from 5 °C to 20 °C.

There is rapid increase in pressure from 580 to 900 bar and a relative change from 0.44 to 0.909 in faults prediction. These changes can be seen to cause a rapid rise in the figures above and faults is most likely to occur. The GT will experience fewer occurrences of faults from 400 to 500 bar.

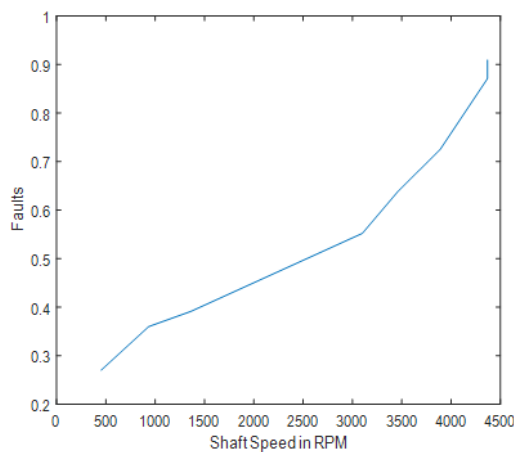


**FIGURE 6: Shaft Speed against Faults**

There is rapid increase in shaft speed from 3500 to 4500 rpm and a relative change from 0.6 to 0.909 in faults prediction. These changes can be seen to cause a rapid rise in the figures above and faults is most likely to occur. The GT will experience fewer occurrences of faults from 1000 to 3200 rpm. The input parameters as stated earlier are temperature, pressure and shaft speed and the output is the fault prediction. The Figures above shows the graphical representation of the input parameters on fault prediction.

## V. CONCLUSION

Gas turbines are fielded as an attractive alternate power source. Although its dominance in industry and military application continues to be strong, the risk of running each unit within their safety margin has caused many eyebrows to be raised. The risk in this context is maintainability and reliability. That is why it is important to prevent to machine from break down through preventive maintenance as this will go a long way to reduce unintentional failure when the machine is needed the most. To this effect, GPA and fault prediction is the way forward for better operation of a gas turbine both in power generation and other applications.

The significant conclusions made from the project are listed below.

- A detailed study of types of gas turbine was carried out.
- Working principles of a GT cycle and their performance are well understood.
- A detailed study on fault prediction was undertaken.
- PG9171 GT of the Ibom Power Plant Company at Ikot Abasi was used as a case study.

### 5.1 Recommendation

Based on the research project, the following recommendations are made:

- Fuzzy logic should be applied as a useful tool because of its simplicity and its ability to tackle problem of uncertainty.
- Other principal parameters such as Temperature, Pressure and Shaft Speed should be used to analyse condition monitoring of the GT.
- To prevent gas path faults from occurring which leads to breakdown of the machine, the causes of the gas path faults should be dealt with.

## REFERENCES

- [1] Asgari, H., Venturini, M., Chen, X.Q., and Sainudiin, R. (2014).Modelling and Simulation of the Transient Behaviour of an Industrial Power Plant Gas Turbine.ASME Journal of Engineering for Gas Turbines and Power.136(6), 061601.10 pages
- [2] Asgari, H., Chen, X.Q., and Sainudiin, R. (2013).Modelling and Simulation Approaches for Gas Turbine System Optimization.In M.K. Habib and J.P. Davim (Eds.), Engineering Creative Design in Robotics and Mechatronics.Ch. 14, pp. 240-264, IGI Global.
- [3] Bazazzadeh, M., Badihi, H., &Shahriari, A. (2011).Gas Turbine Engine Control Design Using Fuzzy Logic and Neural Networks.*International Journal of Aerospace Engineering* , 12 pp.
- [4] Odokwo.V.E., Ogbonnaya.E.A., Nwaorgu.G.O. (2019).Performance Optimization of Combined Gas and Steam Power Plant using Matrix Laboratory. *International Journal for Research in Applied Science and Engineering Technology (IJRASET)*, ISSN: 2321-9633; IC Value: 45.98; Volume 7 Issue X, Oct 2019
- [5] Shalan, H. E. M. A, M. A. Moustafa Hassan and A. B. G. Bahgat (2010) Comparative Study On Modelling Of Gas Turbines In Combined Cycle Power Plants. Proceedings of the 14th International Middle East Power Systems Conference (MEPCON'10), Cairo University, Egypt, December 19-21, 2010, Paper ID 317
- [6] MarekDzida and Olszewski.(2011).Comparing combined gas turbine/steam turbine and marine low speed piston engine/steam turbine systems in naval applications *Polish Maritime Research* 4(71) 2011 Vol 18; pp. 43-48 10.2478/v10012-011-0025-8.
- [7] Doel, D.I. (2003). Interpretation Of Weighted Least Squares Gas Path Analysis Results.*Journal of Engineering for Gas Turbines and Power*, 125(3); 642-633.
- [8] Scaravanamutto H.I., Rogers H; Cohen H and Stranznicky P.V (2001). Modelling and Control of An O<sub>2</sub>/2O<sub>2</sub> Gas Turbine Cycle. 7<sup>th</sup> edition of Gas Turbine Theory ISBN 9781292093130.
- [9] Ying Y., Yunpeng C., andShuying Li. (2016).Study On Gas Turbine Engine Fault Diagnostic Approach with a Hybrid of Gray Relation and Gas Path Analysis.*Advances in Maechanical Engineering*, vol 8(1) 1-14.
- [10] Jasmani M.S; Li Y.G and Z. Ariffin, (2011). Measurement Selection For Multicomponent Gas Path Diagnostic Using Analytical Approach and Measurement Subset Concept. *Journal of Engineering and Gas Turbine Power*, 133(11).
- [11] Sajeev A.M (2015).Gas Turbine Diagnosis Based on Gas Path Analysis.Delft University of technology.

- [12] Urban, L.A. (1992). Gas Path Analysis Applied to Turbine Engine Condition Monitoring. AIAA-72-1082.
- [13] Provost M.J. (1994). The Use of Optimal Estimation Techniques in the Analysis of Gas Turbine. PhD and Master's Thesis, school of engineering Cranfield university, (953) UK
- [14] Ogbonnaya E. A and Ugwu H. U. (2012). Analysis Of Steam Recuperative System To Cogas Plant. *Journal of Engineering and Applied Sciences*. Asian Research Publishing Network (ARPAN). Vol. 7, NO. 5.
- [15] Cengel Y. A. and Boles A. M. (2010). *Thermodynamics: An Engineering Approach*. 6th Ed. McGraw-Hill. pp. 589.

# A Study to Evaluate the Effectiveness of Self Instructional Module on Knowledge and Practice regarding Integrated Management of Neonatal and Childhood Illnesses among Staff Nurses working in Paediatric Wards of Selected Hospitals in Patna, Bihar

Rohit Tongariya

Principal, Govt. ANMTC, Katihar (Bihar)  
(Nursing Officer, Patna Medical College & Hospital)-2015-2018

## Abstract—

**Introduction:** Children are our future and our most precious resources. Today's children are the citizens of tomorrow's world. The IMNCI case management component is mainly focused on the classification of the five most common causes of infant mortality (diarrhoea, pneumonia, malaria, measles and malnutrition), identification of treatment, accurate treatment or timely referral, counseling of the mother and giving follow-up care. IMNCI integrated treatment guidelines are devised to assist the health workers to assess the sick child by observing easily recognizable signs. Working through a color-coded system, the health worker classifies the sickness and takes the necessary steps such as urgent referral for medical treatment at a health Centre, medical treatment on the spot or advice for home management.

**Method & Material:** An evaluative research approach and quasi-experimental research design was adopted. 150 nurses working in pediatric wards of selected hospitals at Patna were selected for the study by using purposive sampling technique. By using knowledge questionnaires, and competency checklists questionnaires.

**Results:** The study reveals that out of 100% of nurses 3.3% of the nurses had good knowledge before Self-instructional module; majority of the nurses 60% had average knowledge; 36.6% of the nurses had poor knowledge. Whereas majority of the subjects 76.7% had good knowledge, 23.3% nurses had average knowledge after a Self-instructional module in IMNCI. In competency 51.7% had moderate on practice, 38.3% had adequate knowledge on practice, and 10% of the nurses had inadequate knowledge on practice before the Self-instructional module. Whereas majority of the nurses 83.3% had adequate knowledge on practice, 16.7% nurses had moderate knowledge on practice after the Self-instructional module on IMNCI.

**Conclusion:** There is a positive co-relation observed between the level of knowledge and practice regarding Integrated Management of Neonatal and Childhood Illnesses among staff nurses. The study revealed that Self-instructional module improved the knowledge and practice regarding Integrated Management of Neonatal and Childhood Illness among Staff nurses.

**Keywords—** Knowledge, Practice IMNCI.

## I. INTRODUCTION

Children are our future and our most precious resources. Today's children are the citizen's of tomorrow's world. In other words, the children are the budding human resources and the future citizens of the nation. Healthy children are not only assets but also the stepping stone to build a strong and prosperous nation. Their survival and protection is prerequisite for the future development of humanity. Every child represents the unit of human capital. He/she has the potential to grow into a productive adult and contribute to the economic and social development of the country. The Integrated management of neonatal and childhood illness strategy is a broad strategy developed by WHO in collaboration with UNICEF, and it aims at reducing childhood deaths, illness, and disability, and improving growth and development. It combines improved management of childhood illness with aspects of nutrition and immunization in children below the age of five years.

### 1.1 Statement of the Problem

“A study to evaluate the effectiveness of Self Instructional Module on knowledge and practice regarding Integrated Management of Neonatal and Childhood Illnesses among staff nurses working in Paediatric wards of selected Hospitals in Patna, Bihar”

## 1.2 Objectives

- 1) To assess the knowledge regarding Integrated Management of Neonatal and Childhood Illnesses among staff nurses before and after a Self instructional module.
- 2) To assess the practice regarding Integrated Management of Neonatal and Childhood Illnesses among staff nurses before and after a Self instructional module.
- 3) To evaluate the effectiveness of a Self Instructional Module based on Integrated Management of Neonatal and Childhood Illnesses among staff nurses.
- 4) To correlate the post test knowledge score with the practice score regarding Integrated Management of Neonatal and Childhood Illnesses among staff nurses.
- 5) To associate the post test knowledge score regarding Integrated Management of Neonatal and Childhood Illnesses among staff nurses with selected demographic variables.
- 6) To associate the post test practice score regarding Integrated Management of Neonatal and Childhood Illnesses among staff nurses with selected demographic variables.

## II. MATERIALS AND METHODS

The present study evaluates the effectiveness of Self Instructional Module on knowledge and practice regarding Integrated Management of Neonatal and Childhood Illnesses among staff nurses. An evaluative research approach, quasi-experimental research design was adopted. 150 nurses working in pediatric wards of selected hospitals at Patna were selected for the study. Purposive sampling technique is used. The data is collected by structured interview questionnaire and an observational checklist. This structured interview questionnaire contains 40 questions and an observational checklist consists of 20 questions.

### 2.1 Description of data collection instruments

**Section –I** Baseline data

**Section-II** Knowledge questionnaire regarding integrated management of neonatal and child hood illnesses.

**Section- III** Structured Observational checklist on integrated management of neonatal and child hood illnesses.

**Section- IV** Self Instructional Module on integrated management of neonatal and child hood illnesses.

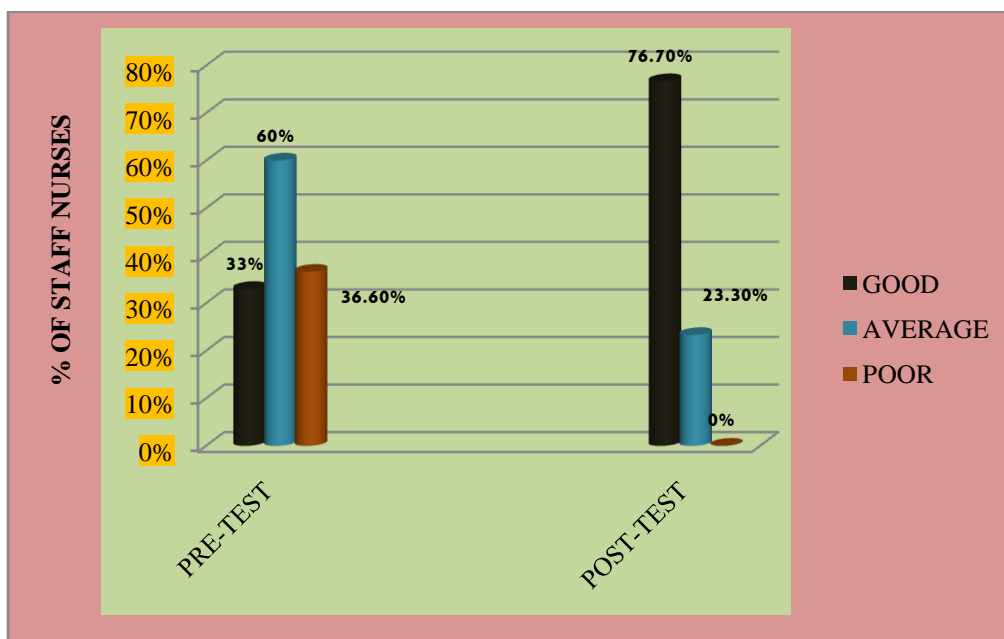


**FIGURE 1: Distribution of staff nurses knowledge before and after self instructional module on IMNCI**

Figure 1. The findings revealed that among the 150 staff nurses, before the administration of Self instructional module, majority of them 90(60%) had average knowledge and 5 (33%) had good knowledge. After the administration of Self instructional module, majority of them 115 (76.7%) had good knowledge and 35 (23.3%) had average knowledge on IMNCI.

**TABLE 1**  
**FREQUENCY AND PERCENTAGE DISTRIBUTION OF SELECTED DEMOGRAPHIC VARIABLES OF NURSES**  
**n=150**

S. No	Demographic variables	Frequency(f)	Percentage (%)
1	<b>Age (Years)</b>		
	a) 20-25	69	46%
	b) 25-30	57	38%
	c) 30-35	18	12%
	d) 35 and above	6	4%
2.	<b>Gender</b>		
	Male	42	28%
	Female	108	72%
3.	<b>Religion</b>		
	Hindu	107	71.33%
	Muslim	15	10%
	Christian	28	18.66%
4.	<b>Professional Education</b>		
	GNM	81	54%
	B.SC.N	60	40%
	PB B.SC.N	9	6%
5.	<b>Years of Experience (Years)</b>		
	0-3	21	14%
	3-6	108	72%
	6-10	12	8%
	10 and Above	9	6%
6.	<b>Source Of Information</b>		
	Books	9	6%
	Journals	24	16%
	Training	21	14%
	In service education	15	10%
	Any other	36	24%
	Nil	45	30%

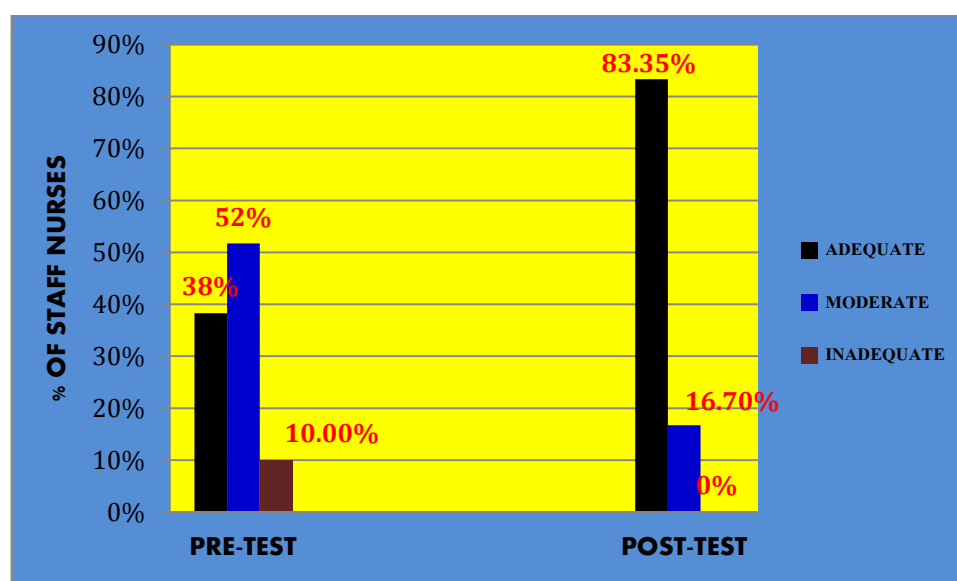


**FIGURE 2: Distribution of staff nurses knowledge on practice before and after a Self-instructional module on IMNCI**

Figure 2. The findings revealed that among the 150 staff nurses, before the administration of Self instructional module majority of the them 78(51.7%) had moderate knowledge on practice and only 15(10%) had inadequate knowledge on practice. whereas after the administration of Self instructional majority of them 125(83.3%) had adequate knowledge on practice and 25(16.7%) had moderate knowledge on practice on IMNCI.

**TABLE 2**

**EFFECTIVENESS OF THE SELF INSTRUCTIONAL MODULE IN IMPROVING THE LEVEL OF KNOWLEDGE AND PRACTICE REGARDING INTEGRATED MANAGEMENT OF NEONATAL AND CHILDHOOD ILLNESSES AMONG STAFF NURSES**

n=150

S. No	variables	Maximum Score	Pre test		Post test		‘t’ Value
			Mean	SD	Mean	SD	
1.	Knowledge	40	11.8	3.6	24.5	3.16	32.42
2.	Practice	20	4.3	1.69	8.8	1.56	23.96

Table 2 Showed that there was a significant difference found ( $P < 0.05$ ) between the pretest mean score 11.8 ( $\pm 3.6$ ) and posttest mean score of knowledge 24.5 ( $\pm 3.16$ ) and mean score pretest knowledge on practice 4.3 ( $\pm 1.69$ ) and posttest mean score 8.81 ( $\pm 1.56$ ). The t value for knowledge were 32.42 and 23.96 for practice which is greater than table value (1.655) at  $p < 0.05$ . It shows that the self instructional module was effective in improving the knowledge and practice regarding Integrated Management of Neonatal and Childhood Illnesses among staff nurses.

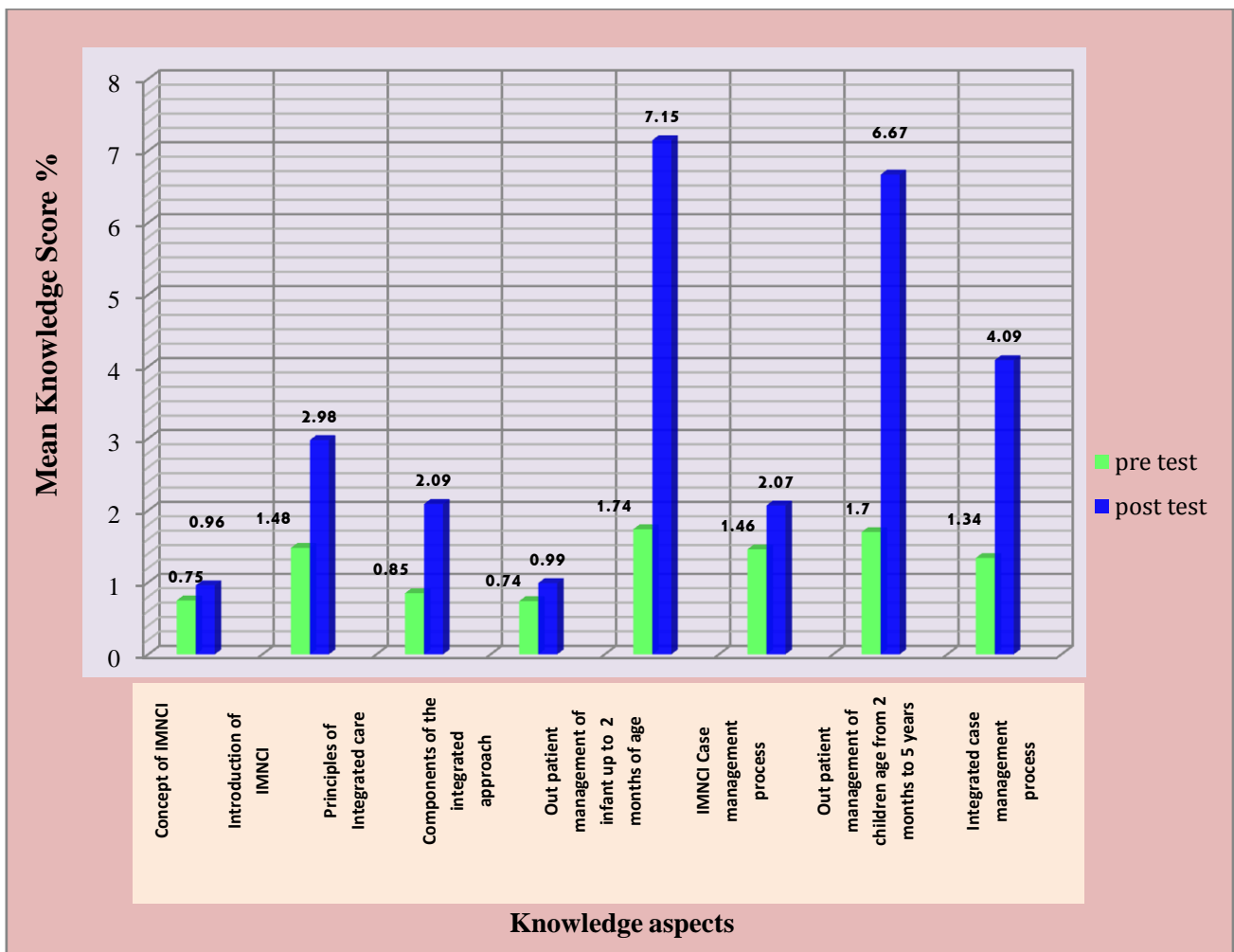


**FIGURE 3: Effectiveness of the self instructional module in improving the level of knowledge regarding individual aspects of Integrated Management of Neonatal and Childhood Illnesses among staff nurses.**

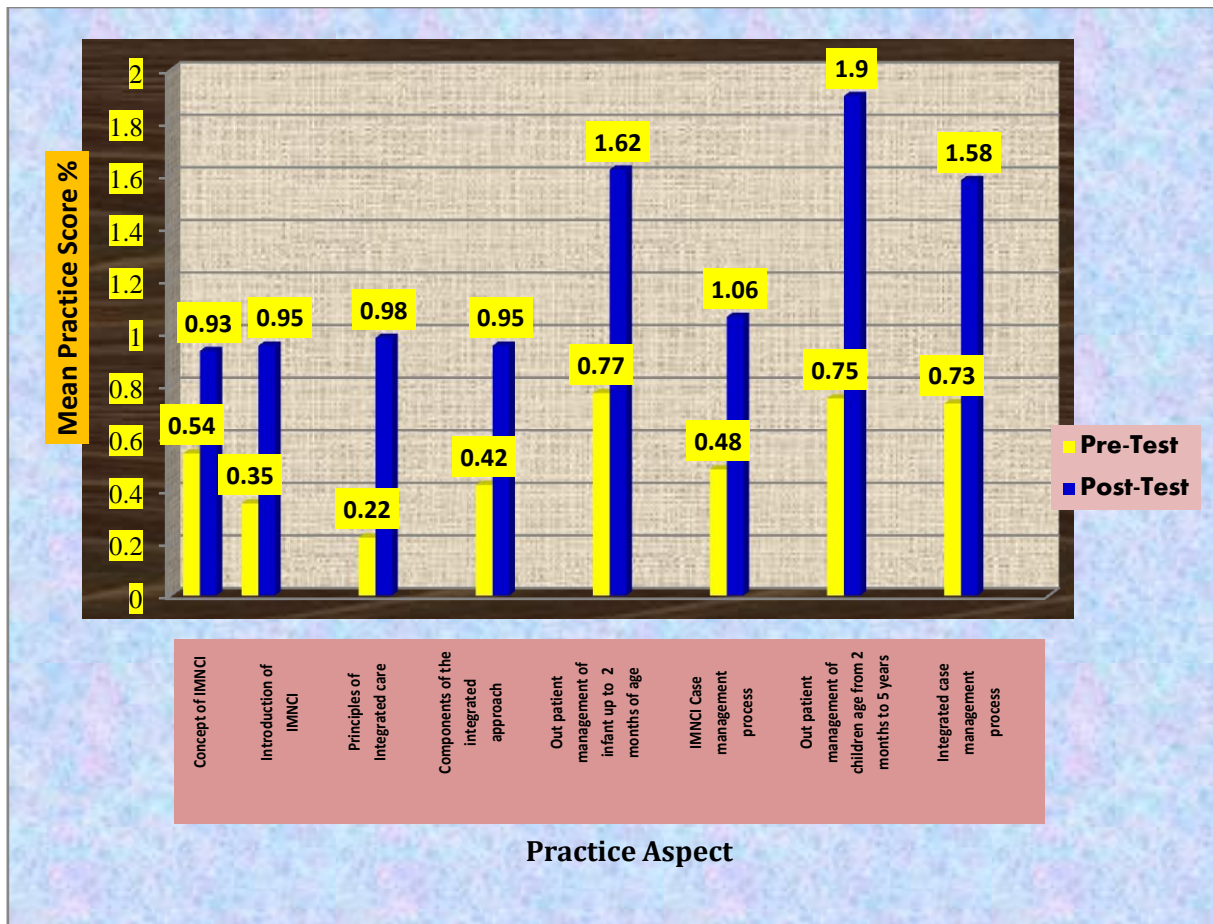


**FIGURE 4: Effectiveness of the self instructional module in improving the practice regarding individual aspects of Integrated Management of Neonatal and Childhood Illnesses among staff nurses.**

**TABLE 3**

**CO-RELATION BETWEEN THE POST TEST LEVEL OF KNOWLEDGE SCORE AND PRACTICE SCORE REGARDING INTEGRATED MANAGEMENT OF NEONATAL AND CHILDHOOD ILLNESSES AMONG STAFF NURSES.**

n=150

	Knowledge		Practice		'r' Value
	Mean	SD	Mean	SD	
<b>Sample 150</b>	24.5	3.16	8.8	1.56	1

Table 3- showed that there is a positive co-relation observed between the level of knowledge and practice regarding Integrated Management of Neonatal and Childhood Illnesses among staff nurses.

**III. RESULTS**

The study reveals that out of 100% of nurses 3.3% of the nurses had good knowledge before Self-instructional module; majority of the nurses 60% had average knowledge; 36.6% of the nurses had poor knowledge. Whereas majority of the subjects 76.7% had good knowledge, 23.3% nurses had average knowledge after a Self-instructional module in IMNCI. In competency 51.7% had moderate on practice, 38.3% had adequate knowledge on practice, and 10% of the nurses had inadequate knowledge on practice before the Self-instructional module. Whereas majority of the nurses 83.3% had adequate knowledge on practice, 16.7% nurses had moderate knowledge on practice after the Self-instructional module on IMNCI. There was a significant difference found ( $P < 0.05$ ) between the pretest mean score 11.8 ( $\pm 3.6$ ) and posttest mean score of knowledge 24.5 ( $\pm 3.16$ ) and mean score pretest knowledge on practice 4.3 ( $\pm 1.69$ ) and posttest mean score 8.81 ( $\pm 1.56$ ). The t value for knowledge were 32.42 and 23.96 for practice which is greater than table value (1.655) at  $p < 0.05$ . It shows that the

self instructional module was effective in improving the knowledge and practice regarding Integrated Management of Neonatal and Childhood Illnesses among staff nurses. There is a positive co-relation observed between the level of knowledge and practice regarding Integrated Management of Neonatal and Childhood Illnesses among staff nurses. There is no association between age, gender, religion, professional education, years of experience and source of information regarding Integrated Management of Neonatal and Childhood Illnesses with the knowledge score of staff nurses. There is no association between age, gender, religion, professional education, years of experience and source of information regarding Integrated Management of Neonatal and Childhood Illnesses with the practice score of staff nurses.

#### IV. CONCLUSION

From the findings of the present study, it is concluded that the level of knowledge and practice regarding Integrated Management of Neonatal and Childhood Illness among staff nurses was inadequate during the pre-test assessment. However, the findings in the post-test, knowledge and practice have improved and the scores indicated an adequate level of knowledge and practice among staff nurses. The improvement is due to the administration of the Self instructional module. Therefore the knowledge and practice of the staff nurses can be further improved by providing on-going teaching and health education programmes.

The study revealed that Self instructional module improved the knowledge and practice regarding Integrated Management of Neonatal and Childhood Illness among Staff nurses

#### LIMITATIONS OF THE STUDY

- There was no actual observation of the practical performance of the staff nurses but only their responses on practice.
- The duration after the study post test assessment was very small; so long term retention cannot be measured.

#### RECOMMENDATIONS

- 1) A similar study can be undertaken with larger samples to validate and generalize the findings of the study.
- 2) The present study can be replicated in similar and different settings.
- 3) A similar study can be conducted among school students and non-medical college students.
- 4) A study can be conducted to assess the knowledge and practice of mothers of under five children regarding Integrated Management of Neonatal and Childhood Illnesses in community.
- 5) A similar study can be undertaken by using different teaching methods.
- 6) A similar study can be conducted on various aspects of IMNCI guideline

#### REFERENCES

- [1] K Park "Text Book of preventive and social medicine", 18th edition, Banarsidas Dhanot publishes pg 235.
- [2] "New Health policy and planning frame work part 1st working version", pg 235 in Jan30, 2005.
- [3] Deshmukh (2008). Perception and health care seeking about Newborn Danger signs among mothers Indian Journal of pediatrics 75(1) 324 – 326.
- [4] 'National Research For Institute of child health and Development in Tokyo', volume 48 [8] pg 404-409 2206 August 2005'.
- [5] WHO Department of child and Adolescent Health and Development [CAH], "Student handbook of IMNCI 2003".
- [6] Isabelle.de.Zoysa, Nita Bhandari, Naseema Akhtar Maharaj K Bhan; science direct; case seeking for illness in young infants in an urban slum in India, Volume 47, issue 12, pages 2101-2111, 1998.
- [7] Sinhababu A. Mukhopadhyay DK, Panja TK, Saren, Mandal NK, et.al., (2010) A study on infant and young feeding practices, Journal of Health Population and Nutrition. 28(6) 294-9.
- [8] Thompson. M.E, and Harutyunyan, (2009). Impact of Community based IMCI. Health Policy Plan. 24(2).45-46.
- [9] Athumanijuma, (2007). Knowledge, Attitude, practice of mothers on symptoms and signs of IMNCI strategy. official publication of medical student's Association 73(7).1-5.
- [10] Kelly JM, Rowe AK, Onikpo F, Lama M., Cokouits F, et.al (2007). Care takers' recall of Integrated Management of Childhood Illness counselling messages in Benin. Published online 2009 Oct 1. doi: [10.1186/1471-2431-9-62.
- [11] Neerugupta, (2007). An Evaluation of diarrheal disease and Acute respiratory infection. Indian Journal of Pediatrics. 74 (5) 234 – 236.

- 
- [12] Santosh K, Bhargava. Center for Newborn care. Department of Pediatrics, SL Jain Hospital. The Challenge of Neonatal Mortality in India. *Indian Pediatrics* 2004; 41:657-662.
- [13] Srivastava NM, Awasthi S, Agarwal GG, Care-seeking behavior and out-of-pocket expenditure for sick newborns among urban poor in Lucknow, northern India: a prospective follow-up study. *Indian J Comm Med* 2009; Apr 2; 61.
- [14] SY, Holloway KA, Ivanovska V, Muhe L, Lambrechts T. Does shortening the training on integrated management of childhood illness guidelines reduce its effectiveness? A systematic review. *Health policy plan*. 2011 Apr 23. Available from : <http://www.ncbi.nlm.nih.gov/pubmed>.
- [15] Lulseged S , Integrated management of childhood illness: a review of the Ethiopian experience and prospects for child health , *Etiopian medical Journal* , 2002 Apr;40(2):187-201.
- [16] Christiane Horwood, Kerry Vermaak, Nigel Rollins, Lyn Haskins, Phumla Nkosi, and Shamim Qazi, An Evaluation of the Quality of IMCI Assessments among IMCI Trained Health Workers in South Africa, *PLoS ONE*. 2009; 4(6): e5937.



**AD Publications**

**Sector-3, MP Nagar, Bikaner,  
Rajasthan, India**

**[www.adpublications.org](http://www.adpublications.org), [info@adpublications.org](mailto:info@adpublications.org)**